

---

Doctoral Dissertations

Student Theses and Dissertations

---

Summer 2024

# Non-Linearity Modeling and Quantifications for Practical Rf Interference Control

Shengxuan Xia

*Missouri University of Science and Technology*

Follow this and additional works at: [https://scholarsmine.mst.edu/doctoral\\_dissertations](https://scholarsmine.mst.edu/doctoral_dissertations)



Part of the [Electrical and Computer Engineering Commons](#)

Department: **Electrical and Computer Engineering**

---

## Recommended Citation

Xia, Shengxuan, "Non-Linearity Modeling and Quantifications for Practical Rf Interference Control" (2024). *Doctoral Dissertations*. 3320.

[https://scholarsmine.mst.edu/doctoral\\_dissertations/3320](https://scholarsmine.mst.edu/doctoral_dissertations/3320)

This thesis is brought to you by Scholars' Mine, a service of the Missouri S&T Library and Learning Resources. This work is protected by U. S. Copyright Law. Unauthorized use including reproduction for redistribution requires the permission of the copyright holder. For more information, please contact [scholarsmine@mst.edu](mailto:scholarsmine@mst.edu).

NON-LINEARITY MODELING AND QUANTIFICATIONS FOR PRACTICAL RF  
INTERFERENCE CONTROL

by

SHENGXUAN XIA

A DISSERTATION

Presented to the Graduate Faculty of the  
MISSOURI UNIVERSITY OF SCIENCE AND TECHNOLOGY

In Partial Fulfillment of the Requirements for the Degree

DOCTOR OF PHILOSOPHY

in

ELECTRICAL ENGINEERING

2024

Approved by:

Chulsoon Hwang, Advisor

Jun Fan, Co-Advisor

Daryl Beetner

DongHyun Kim

Xiaoming He

© 2024

SHENGXUAN XIA

All Rights Reserved

## PUBLICATION DISSERTATION OPTION

This dissertation consists of the following four articles, formatted in the style used by the Missouri University of Science and Technology:

Paper I, found on pages 7–37, Dipole Moment Based Reciprocity for Practical Desensitization Identification and Mitigation, has been published in *IEEE Transactions on Electromagnetic Compatibility*, vol. 65, no. 4, pp. 1017-1026, Aug. 2023, doi: 10.1109/TEM.2023.3247784.

Paper II, found on pages 38–48, Capacitive Radio Frequency Metallic Contacts for Low Passive Intermodulation, has been submitted to *IEEE Microwave and Wireless Technology Letters*.

Paper III, found on pages 49–77, Sideband Spectrum Estimations Based on Two-tone Passive Intermodulation Characterization, is intended for submission to *IEEE Transactions on Electromagnetic Compatibility*.

Paper IV, found on pages 78–110, A Segmentation Approach for Predicting Plane Wave Coupling to PCB Structures, has been accepted in *IEEE Transactions on Electromagnetic Compatibility*.

## ABSTRACT

Radio frequency (RF) interference can degrade the receiving sensitivity of antennas (desense problem). It is essential to model the nonlinearity as it is the root-cause of the unwanted frequency components. Understanding the electromagnetic (EM) coupling or radiated emissions is also important.

Nonlinearity causes modulation-involved desense problems, and it consists of two categories: upconversion of the baseband noise by the transmitting (TX) signal, and the passive intermodulation (PIM) of the transmitting signal itself. The upconversion caused desense can be modeled and analyzed with the dipole-moment based coupling framework. PIM has been identified as another nonlinear distortion mechanism, specifically in the metallic contacts. Capacitive RF contacts are proposed and validated to resolve PIM problems using the anodized layer to skip the quantum tunneling of the metallic contact interfaces. While two-tone test has been mostly adopted in the PIM related studies for measurement characterizations, the link between the two-tone tests and broadband sideband is missing. Therefore, another essential work has been done to establish a link to correlate the two-tone results and wideband sideband spectrum levels.

The proper RF interference control measures for complicated electronic devices without clear geometry information, can be evaluated in a statistical way with a segmentation approach. The segmentation approach allows a faster estimation of the EM coupling levels/RF susceptibility, leading to a better insight of the coupling mechanism and more appropriate interference control solutions.

## ACKNOWLEDGMENTS

I would like to express my great appreciation to my advisor, Dr. Chulsoon Hwang, and my co-advisor Dr. Jun Fan. Their guidance, assistance, and acknowledgement on my Ph. D. studies are essential to all the great outcome I have made. Dr. Hwang helped me significantly with the progress of academic research and provided great opportunity in the future career path. Back in 2017, I happened to be granted with an opportunity to visit Missouri University of Science and Technology EMC Lab and Dr. Fan played an important role leading me to start my Ph.D. journey. Significant changes happened during the pandemic, and I had planned to quit this journey for some other plan. Dr. Hwang and Dr. Beetner were important to change my mind and made me decide to stay eventually.

I would like to thank Dr. Daryl Beetner and Dr. Victor Khilkevich for some other close collaborations on other topics and I have gained a lot in technical skillset.

In addition, I would like to thank Dr. DongHyun Kim and Dr. Xiaoming He for serving on my doctoral committee members.

Finally, my sincere appreciation goes to whoever support me especially including my mother.

## TABLE OF CONTENTS

	Page
PUBLICATION DISSERTATION OPTION .....	iii
ABSTRACT.....	iv
ACKNOWLEDGMENTS .....	v
LIST OF ILLUSTRATIONS .....	x
LIST OF TABLES .....	xiii
 SECTION	
1. INTRODUCTION.....	1
1.1. MODULATION- INVOLVED RF DESENSE PROBLEMS.....	1
1.2. PASSIVE INTERMODULATION CAUSED RF DESENSE.....	2
1.2.1. Passive Intermodulation Characterizations. ....	3
1.2.2. Mitigation Solutions for PIM. ....	4
1.2.3. Nonlinear Model for PIM Spectrum Estimation. ....	4
1.3. FAST EM COUPLING/RADIATED EMISSION ESTIMATION METHOD FOR RF INTERFERENCE CONTROL.....	5
 PAPER	
I. DIPOLE MOMENT BASED RECIPROCITY FOR PRACTICAL DESENSITIZATION IDENTIFICATION AND MITIGATION .....	7
ABSTRACT.....	7
1. INTRODUCTION.....	8
2. DIPOLE MOMENT BASED RECIPROCITY FOR RF COUPLING ESTIMATIONS.....	11

2.1. BRIEF INTRODUCTION TO THE PROBLEM OF MODULATION-INVOLVED RF DESENSITIZATION .....	11
2.2. NOISE SOURCE MODELING WITH DIPOLE MOMENTS .....	13
2.3. COUPLING PATH MODELING .....	19
3. RF COUPLING QUANTIFICATIONS AND ANALYSIS .....	23
3.1. CORRELATIONS .....	23
3.2. NOISE COUPLING CONTRIBUTION ANALYSIS .....	25
4. PRACTICAL RF DESENSITIZATION MITIGATION METHODS .....	26
4.1. SUPPRESSING RADIATION ON DOMINANT NOISE SOURCES.....	26
4.2. COUPLING CANCELLATION METHOD .....	27
4.3. NOISE SPECTRUM SUPPRESSION .....	30
4.4. SUMMARY FOR RFI PROBLEM SOLVING .....	31
5. DISCUSSIONS .....	34
REFERENCES .....	35
II. CAPACITIVE RADIO FREQUENCY METALLIC CONTACTS FOR LOW PASSIVE INTERMODULATION .....	38
ABSTRACT .....	38
1. INTRODUCTION.....	38
2. PROPOSED CAPACITIVE RF CONTACT.....	40
2.1. CONCEPT AND IMPLEMENTATION.....	40
2.2. PIM MEASUREMENT VALIDATION .....	41
2.3. EVALUATION OF THE CONTACT IMPEDANCE .....	43
3. CONCLUSION .....	47

REFERENCES.....	47
III. SIDEBAND SPECTRUM ESTIMATIONS BASED ON TWO-TONE PASSIVE INTERMODULATION CHARACTERIZATION .....	49
ABSTRACT .....	49
1. INTRODUCTION.....	50
2. PIM ESTIMATION .....	52
2.1. TWO-TONE CASE.....	52
2.2. BROADBAND CASE.....	55
3. MEASUREMENT VALIDATION.....	63
3.1. REAL TX SPECTRUM.....	63
3.2. METALLIC CONTACT MEASUREMENT SYSTEM .....	67
3.3. TUNABLE NONLINEAR SOURCE SYSTEM.....	69
4. CONCLUSIONS .....	74
REFERENCES.....	75
IV. A SEGMENTATION APPROACH FOR PREDICTING PLANE WAVE COUPLING TO PCB STRUCTURES .....	78
ABSTRACT .....	78
1. INTRODUCTION.....	79
2. SEGMENTATION APPROACH .....	82
2.1. CASCADABLE SEGMENTS FOR FAST COUPLING ANALYSIS .....	82
2.2. FAR-FIELD RECIPROCITY.....	83
2.3. GENERALIZED S-PARAMETERS BASED ON FAR-FIELD RECIPROCITY .....	84
2.4. ROTATION, TRANSLATION, AND CASCADING OF SEGMENTS.....	86

3. PRE-CHARACTERIZATION OF SEGMENTS.....	89
3.1. MODELING OF SEGMENTS USING FULL-WAVE SIMULATIONS .....	89
3.2. ANALYTICAL MODELING OF THE STRAIGHT TRACES .....	90
3.3. MODELING OF TRACE BENDS .....	92
4. ASSESSMENT ACCURACY OF THE SEGMENTATION METHOD.....	95
4.1. TRANSLATION INDUCED ERROR.....	95
4.2. IMPACT OF FINITE GROUND PLANE.....	97
4.3. LIMITATIONS AND THE POTENTIAL ERRORS.....	99
5. STATISTICAL ANALYSIS OF COUPLING USING THE SEGMENTATION METHOD .....	101
6. DISCUSSION AND CONCLUSIONS.....	106
REFERENCES.....	107
SECTION	
3. CONCLUSIONS AND SUMMARY.....	111
REFERENCE.....	112
VITA.....	121

## LIST OF ILLUSTRATIONS

SECTION	Page
Figure 1.1. An example of up-conversion of baseband noise causing interference. ....	1
Figure 1.2. Near-field pattern for dipole moment extractions. ....	2
Figure 1.3. PIM measurement system for flexible metallic component. ....	3
Figure 1.4. Capacitive contact concept. ....	4
Figure 1.5. Broadband sideband spectrum caused by PIM. ....	5
Figure 1.6. Segmentation concept for fast EM coupling analysis. ....	6
 PAPER I	
Figure 1. Demonstration of modulation-involved RF desensitization demonstrations. ...	12
Figure 2. Near field scan measurement setup. ....	13
Figure 3. Scanned H-field patterns, dipole moment types, and locations. ....	15
Figure 4. Rescaling the dipole moment magnitudes with the measurements for two configurations. ....	17
Figure 5. Modeling of the RF antenna. ....	21
Figure 6. Performance of the whole antenna module. ....	22
Figure 7. Correlations of the total EM couplings between a direct measurement and reciprocity-based calculations. ....	24
Figure 8. Individual contributions of the noise sources. ....	26
Figure 9. Near-field changes with additional grounding planes. ....	26
Figure 10. Cancellation method implementation. ....	29
Figure 11. Simulated S21 for the two layout designs of the dmic circuit. ....	30

Figure 12. Changing the ferrite beads to better suppress the unwanted spectrum generation.....	32
Figure 13. Practical workflow for solving RFI problems. ....	33
<b>PAPER II</b>	
Figure 1. FOF contacts between metal chassis pads.....	40
Figure 2. Flexible metallic components and landing substrates. ....	40
Figure 3. Two-tone PIM test platform for flexible metallic components. ....	42
Figure 4. Measured force–PIM results of FOF contacts with conductive (etched) and non-conductive (anodized) Al6013 pads. ....	43
Figure 5. Two-port shunt topology test fixture for contact characterization .....	44
Figure 6. Contact evaluations of measured and extracted equivalent circuits.....	45
<b>PAPER III</b>	
Figure 1. Generation of different sideband spectra.....	52
Figure 2. LTE band 20 TX spectrum, 23 dBm, various bandwidth settings. ....	57
Figure 3. Demonstration of the IM products’ sideband spectrum. ....	58
Figure 4. Approximation of the summation of random phasors.....	60
Figure 5. Using a Gaussian distribution to approximate the Irwin-Hall distribution. ....	62
Figure 6. Measured TX spectrum (zoomed in, 100 KHz span) consisting of many tones with 1 KHz spacing. ....	63
Figure 7. Investigation of modeling for mimicked TX.....	64
Figure 8. Investigation of the pre-distorted TX spectrum.....	65
Figure 9. Measurement setup for validation of a metallic contact.....	67
Figure 10. Test fixture comprising a flexible metallic component (Al pads on two micro-strip boards and conductive fabric over foam).....	67

Figure 11. Correlation results of a conductive foam (0.24 N loading force case).....	67
Figure 12. Measurement setup.....	70
Figure 13. Automation of the test flow.....	72
Figure 14. Measurement results and comparison. ....	73
<b>PAPER IV</b>	
Figure 1. Segmentation concept illustration. ....	82
Figure 2. PCB under electromagnetic wave illumination.....	83
Figure 3. Generalized S-parameter model to represent a segment under plane wave illumination.....	85
Figure 4. (a) a trace routing example composed by 7 segments; (b) translation and rotation to a segment (top view); (c) equivalent circuit representation. ....	86
Figure 5. Extra time delay due to the translation (on the 2D plane) of the segment. ....	88
Figure 6. Modeling of a microstrip trace segment to obtain generalized S-parameters ...	89
Figure 7. Two straight traces are added to a small trace bend to allow simulation with waveguide ports. ....	92
Figure 8. De-embedding the characteristics of the bend.....	93
Figure 9. Investigation of the translation error .....	96
Figure 10. Impact of the size of the ground plane and relative position of the trace.....	98
Figure 11. Random IC-trace-IC geometry.....	102
Figure 12. Statistical analysis of random IC-trace-IC geometries.....	103

**LIST OF TABLES**

PAPER I	Page
Table 1. Extracted Dipole Moments (@873.6 MHz for example) .....	20
PAPER II	
Table 1. Capacitance Extraction Results .....	46
PAPER III	
Table 1. Correlation Results for Alodine-coated Conductive Foam.....	70
PAPER IV	
Table 1. Computational Time Comparison.....	105

# 1. INTRODUCTION

## 1.1. MODULATION- INVOLVED RF DESENSE PROBLEMS

Radio frequency (RF) interference can degrade the receiving sensitivity of antennas (desense problem). For the typical RF interference problems, engineers have been aware of the potential noise sources such as high-speed channels, integrated circuits (ICs), camera modules, etc. The direct electromagnetic (EM) coupling between the RF antenna and the noise sources can be well modeled using dipole-moment-based coupling framework. However, when nonlinearity is considered, the noise spectrum can be more complicated than the direct EM coupling because the nonlinear distortion can make the occurrence of the new frequency components.

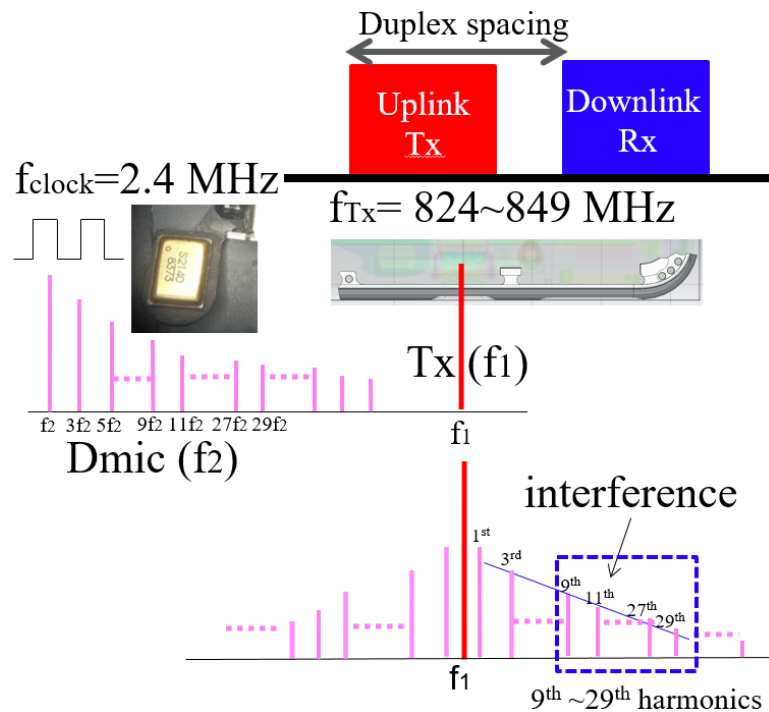


Figure 1.1. An example of up-conversion of baseband noise causing interference.

The nonlinear property allows the baseband noise to be up-converted when modulating with the high-frequency transmitting (TX) signals. As Figure 1.1 demonstrates, after the modulation, the newly generated spectrum can be adjacent to the TX range and result in the desense problems in frequency-division-duplex (FDD) systems.

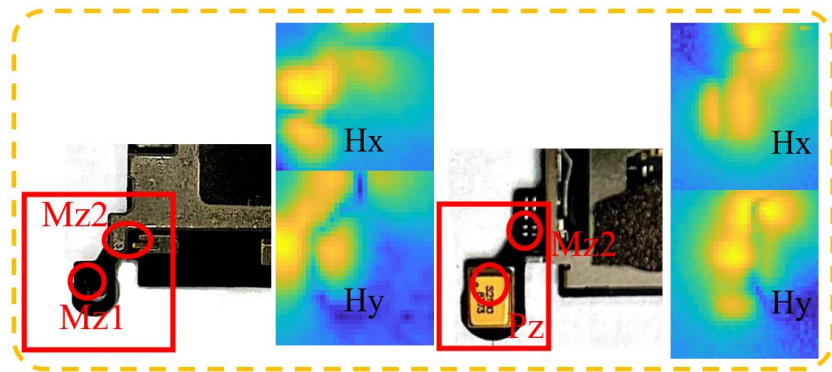


Figure 1.2. Near-field pattern for dipole moment extractions.

The up-converted frequency components can still be measured with a spectrum analyzer. When near-field scan is utilized, the scanned tangential H-field patterns and the field strengths above a certain scanning height (Figure 1.2) can reconstruct the equivalent dipole moments to represent the noise sources. More quantitative analysis can provide more insights and prioritize the EM coupling contributions. The contents are covered in the first paper.

## 1.2. PASSIVE INTERMODULATION CAUSED RF DESENSE

Passive intermodulation (PIM) is a subtle nonlinear distortion that happens in the contact interfaces of the metallic components. Because the TX signals in FDD systems

such as LTE are relatively high-power and wideband, the intermodulation of the TX itself can cause the spectrum leakage to the adjacent channels and then contaminate the receiving channels. Due to the enormous power level difference in TX and RX, PIM is still an important consideration even if the nonlinearity is low. Metallic components are widely used in the electronic devices and can potentially degrade the wireless communication qualities.

**1.2.1. Passive Intermodulation Characterizations.** The measurement characterizations of the flexible metallic components such as springs and conductive foams are necessary for evaluating the PIM levels versus the component material, compression range, aging, surface treatment, etc. The high-power TX signals need to flow through the contact points to generate PIM spectrum. To achieve good measurement dynamic range, the high-power TX signal path and low-power RX (PIM) signal path need to be separated.

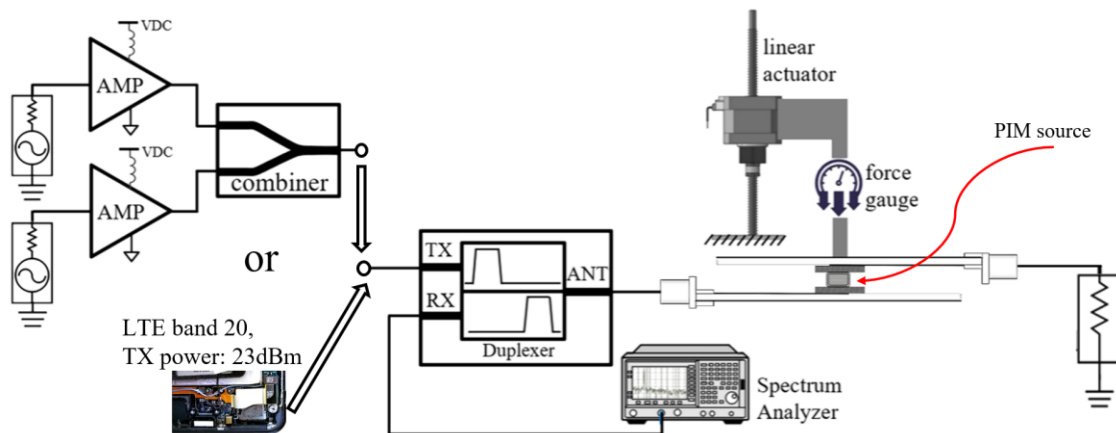


Figure 1.3. PIM measurement system for flexible metallic component.

Duplexer-based system, as shown in Figure 1.3, is an optimal solution for this separation purpose. The TX power is mostly terminated on the right side load, and only

the generated PIM spectrum is reflected and captured in the “RX” port of the duplexer. Furthermore, the setup is equipped with linear actuator and force gauge for automation purpose. So, the mechanical as well as electrical performances can be recorded simultaneously. This setup is useful to dig out many interesting PIM behaviors.

**1.2.2. Mitigation Solutions for PIM.** The PIM measurement setup provides the evidence of quite some PIM mitigation solutions such as enlarging the contact area/points, tighter compression, avoiding “self-contact” status, etc. Besides those solutions, a non-conductive contact is an innovative way to get rid of PIM generation.

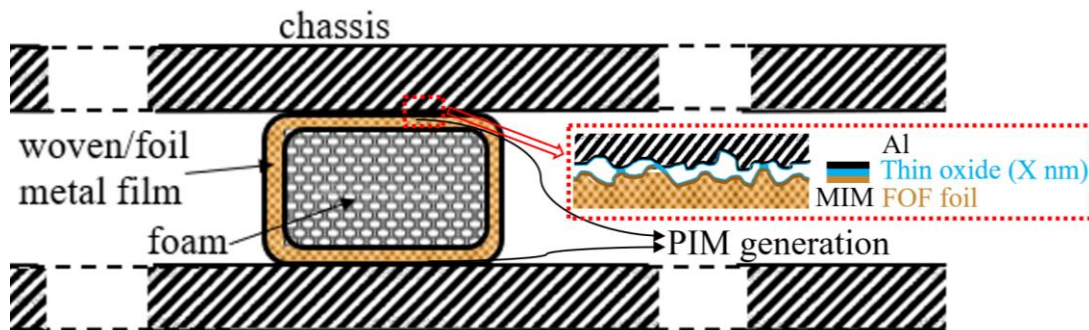


Figure 1.4. Capacitive contact concept.

A most-common mechanism of PIM generation is the tunneling effect due to the existence of the thin oxide layer between the metallic contact interfaces. If the oxide layer thickness is intentionally thickened, the tunneling effect is significantly suppressed to avoid the PIM generation. The change from conductive contact to capacitive contact, however, requires the impedance remaining similarly low at RF range. The PIM-free contact proposal is covered in the second paper.

**1.2.3. Nonlinear Model for PIM Spectrum Estimation.** The two-tone test is the most common measurement method for quantitatively characterize PIM, however, is still

unclear what desense level will be with a certain intermodulation product level. A linkage is needed to connect the two-tone measurements to the wideband spectrum results.

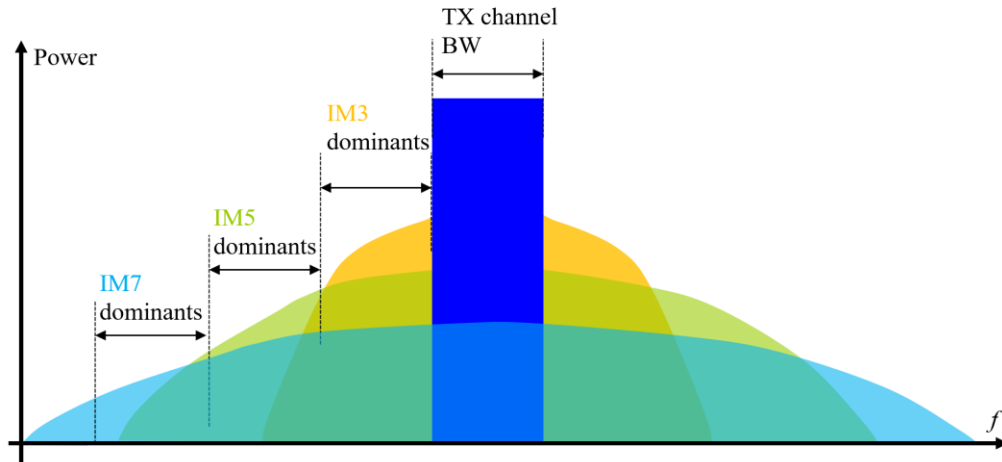


Figure 1.5. Broadband sideband spectrum caused by PIM.

The nonlinear model specifically for sideband spectrum generation can be extracted from two-tone results. The evaluations of the nonlinear distortion, shown in Figure 1.5, with a wideband TX signal injection case, can be achieved with either numerical calculations (frequency-domain convolution) or derived closed-form equations. The detailed establishment of the nonlinear model and the linkage are described in the third paper.

### 1.3. FAST EM COUPLING/RADIATED EMISSION ESTIMATION METHOD FOR RF INTERFERENCE CONTROL

A better insight of the radiated emission, or RF susceptibility with EM couplings, can benefit the RF interference control measures. For complicated structures, the

electromagnetic coupling from an external plane wave can be estimated for multiple angles of incidences. However, the computational effort is too expensive to exhaust all the possibilities especially when there are also some uncertainties in the target devices. With far-field reciprocity theorem, the EM model can be pre-characterized and stored as components in a library. The segments can be then assembled like building blocks to represent a complicated PCB geometry with minimal computational efforts, as shown in Figure 1.6. With this accelerated segmentation method for electromagnetic coupling analysis, a large number of geometries can be analyzed when considering a variety of PCBs with many random variables. Thus, a better insight of the EM coupling/radiation level can be figured out more easily.

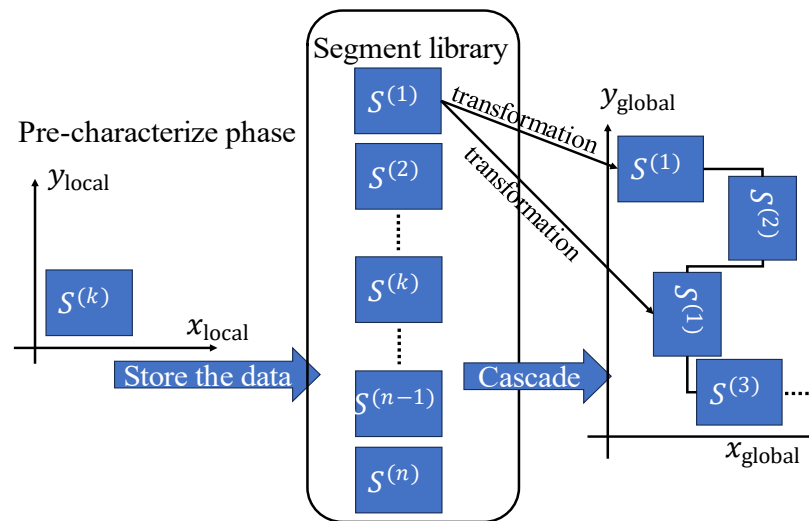


Figure 1.6. Segmentation concept for fast EM coupling analysis.

The detailed theories, derivations, and applications of the fast EM coupling estimation method are covered in the fourth paper.

## PAPER

### I. DIPOLE MOMENT BASED RECIPROCITY FOR PRACTICAL DESENSITIZATION IDENTIFICATION AND MITIGATION

#### ABSTRACT

Radio frequency interference can degrade the receiving sensitivity of antennas. The interference is usually caused by certain coupling structures, such as layouts without adequate grounding for the return path. Those structures can be modeled as a set of equivalent dipole moments. Herein, the dipole moment model-based coupling framework is applied to a practical design case to devise an engineering solution. The coupling framework incorporates dipole-moments as radiation sources and a coupling model based on the reciprocity theorem. Unfortunately, near-field scan probes often lack access to all locations, owing to the compact structure. A combined measurement-simulation method is used to obtain the field quantities lacking direct access to measurements. The dipole-moment-based coupling framework helps estimate the couplings from different noise sources individually. Thus, the priority of solving for better layout designs can be determined according to the coupling estimations. Furthermore, the physics associated with the reconstructed dipole moment can provide insights and suggest possible mitigation methods. Several practical mitigation methods are discussed, including suppression of the dominant noise source, and the coupling path to the victim antenna.

**Keywords:** radio-frequency interference, dipole moment, near field scan, reciprocity, RF desensitization.

## 1. INTRODUCTION

Frequency (RF) interference widely exists in modern electronic devices. RF noise sources usually originate from integrated circuits (ICs), high-speed channels without adequate shielding, camera modules, etc. In modern electronic devices, although those noise sources may not radiate efficiently in the far-field, thus either preventing the products from passing electromagnetic compatibility standards or causing electromagnetic interference (EMI) issues, RF antennas can still experience degradation of sensitivity (RF desensitization). Given the trend toward designing increasingly compact consumer electronics with wireless communication functions, the noise sources from those ICs or modules tend to have more effective coupling to the RF antennas. Therefore, it has become essential for engineers to efficiently identify the root causes and identify solutions.

Near-field scan measurement is often used in electromagnetic compatibility [1], EMI [2], or RF interference applications. A strong near field usually indicates the existence of a significant noise source. More importantly, the measured near field can quantitatively characterize noise sources. In practical applications, field measurements are typically acquired by near-field probes. The electric near-field probes usually have lower measurement accuracy than magnetic near-field probes, because of unwanted H-field coupling and common mode coupling [3]. Thus, unless E-field measurement is necessary, H-field only measurement is a typical choice. Moreover, because measuring complex fields (magnitude and phase) introduces greater test complexity, magnitude-only field scanning is usually preferred when possible [4]. A spectrum analyzer or vector network

analyzer (VNA) is used to read the values measured by the near-field probes, and the instrument readings need to be converted to the field strength with a calibration method such as microstrip-based calibration [5].

The reciprocity theorem effectively aids in analysis of EM coupling. Huygen's box is one form used to obtain the coupling based on EM fields [6]. Detailed derivations and measurement validations have been given previously [7]. This method also applies to multiple-source cases [8] or special scenarios, such as those in which the noise sources are clamped between two conductor plates [9].

Huygen's box based approach is useful but has two obvious disadvantages: complexity and a lack of physical understanding of the EM coupling. When the physical structure that generates the near field is electrically small, the radiating structure can be approximated as an infinitesimal dipole/loop antenna [10]. An infinitesimal dipole antenna with an excitation of electric current is an electric dipole moment, and infinitesimal loop antenna can be considered as a dipole driven by a magnetic current, known as a magnetic dipole moment [11]. Furthermore, when scanning on a plane with a certain height, the measured near field patterns have certain shapes depending on the orientation, type, and amplitude of the equivalent dipole moment. The extracted dipole moments can effectively model RF interference problems by representing complicated noise sources.

A dipole-moment-based coupling framework was developed by using the equivalent dipole moments as a noise radiation source and a coupling model based on the reciprocity theorem. The framework is simple and straightforward, yet provides rigorous physical understanding [12]. Efforts have been made to model dipole moment sources in

full-wave simulations [13] and in measurements [14]. Because the near-field pattern of certain dipole moment always has the same shape, advanced methods such as machine learning can also be used for identifying dipole moment types [15]. A set of equivalent dipole moments can model complicated sources in other applications, such as EMI [16], shielding [17], or far-field [18] scenarios, but nevertheless are more frequently used in RFI applications. One advantage is that the dipole moment can be extracted with tangential H-field magnitude only scans [19], thus simplifying the procedures and decreasing time consumption. The other advantage of the dipole-moment-based coupling framework is that it provides better insight into the EM coupling from the source to the victim antenna. For example, the RF current path on a specific USB connector structure has been identified, thus, dipole moment generation is clearly understood [20]. More importantly, effective solutions can be efficiently proposed, such as a simple rotation of the IC placement [21]. RFI problems can become even more complicated when modulation is involved, such as liquid crystal display clock signals can interfere with the receiving band [22]. Similar issues have been found to be the root causes of RFI due to the modulation of digital microphone (dmic) [23]. The characterization of the modulation may be performed as previously described [24]. In addition, for the measurement of cases involving modulation, the sideband noise may require a duplexer to suppress the high-power transmitting signals for better dynamic range [25]. However, most previous studies aiming to solve real RFI problems have the access to near-field scanning. With the trend toward designing increasingly compact electronic devices, field probes inevitably have limited space for conventional field scanning measurement. Therefore, finding solutions for these scenarios for reference is essential.

Herein, we examined the scenario in which multiple dipole moments are present, and very limited access is available for typical near-field scan measurement. The challenges were conquered on the basis of several assumptions and the information obtained from a changed configuration. Practical solutions showed the high capability of dipole-moment-based reciprocity usage in a complicated case. More importantly, through application of reciprocity for each noise source separately, the priorities of the noise couplings from individual sources were identified. Furthermore, all equivalent dipole moments and coupling paths were clearly determined to understand the mechanism. Efficient and feasible solutions are proposed, together with simulation demonstrations and measurement validation, to demonstrate the improvement.

## **2. DIPOLE MOMENT BASED RECIPROCITY FOR RF COUPLING ESTIMATIONS**

### **2.1. BRIEF INTRODUCTION TO THE PROBLEM OF MODULATION-INVOLVED RF DESENSITIZATION**

The RF desensitization problem is caused by EM coupling between the dmic module and the RF antenna. Because of the non-ideal grounding design near the dmic, the layout becomes a good receiver/radiator structure. According to a previous study [25], three steps cause RF desensitization: 1. The RF antenna radiates the TX signals and couples to the dmic layout. 2. The clock signals are modulated with the captured TX signals in the dmic, because of the nonlinearity of the component. 3. The modulated signals (new spectrum) are radiated from the dmic layout and couple back to the RF antenna.

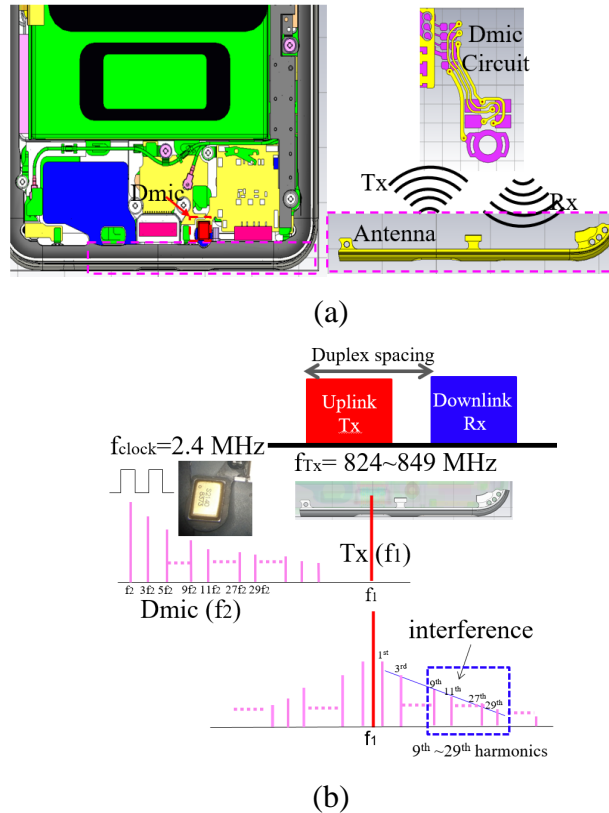


Figure 1. Demonstration of modulation-involved RF desensitization demonstrations: (a) round-trip coupling between the RF antenna and the dmic module, (b) up-conversion of the spectrum by modulation.

As shown in Figure 1 (a), the dmic module is placed very close to the RF antenna, so that the round-trip coupling between the antenna and dmic might potentially be sufficient to cause problems. Although the clock signals (fundamental frequency of 2.4 MHz) of the dmic are within a low-frequency range, the up-converted spectrum after modulation with the TX signals falls into the receiving band, as shown in Figure 1 (b).

Furthermore, the actual TX signals radiating from the RF antenna are wideband, and thus the modulated signals are also wideband. The wideband sideband spectrum tends to be more troublesome than narrowband signals because it contains much higher RF power than a single tone (under the same peak amplitude) and occupies a wider

frequency range so that the popping among channels cannot easily skip those with interference.

## 2.2. NOISE SOURCE MODELING WITH DIPOLE MOMENTS

Dipole-moment-based reciprocity divides the original source-to-victim coupling problem into two parts: source characterization and coupling path modeling. The source characterization involves extraction of the equivalent dipole moment(s) to represent the noise source(s). The coupling path modeling finds the transfer function from the noise source to the victim antenna. Thus, through application of reciprocity, the coupled voltage on the victim antenna caused by the noise source(s) can be determined by the extracted equivalent dipole moment(s) and the transfer function(s) of the dipole moment(s) to the antenna.

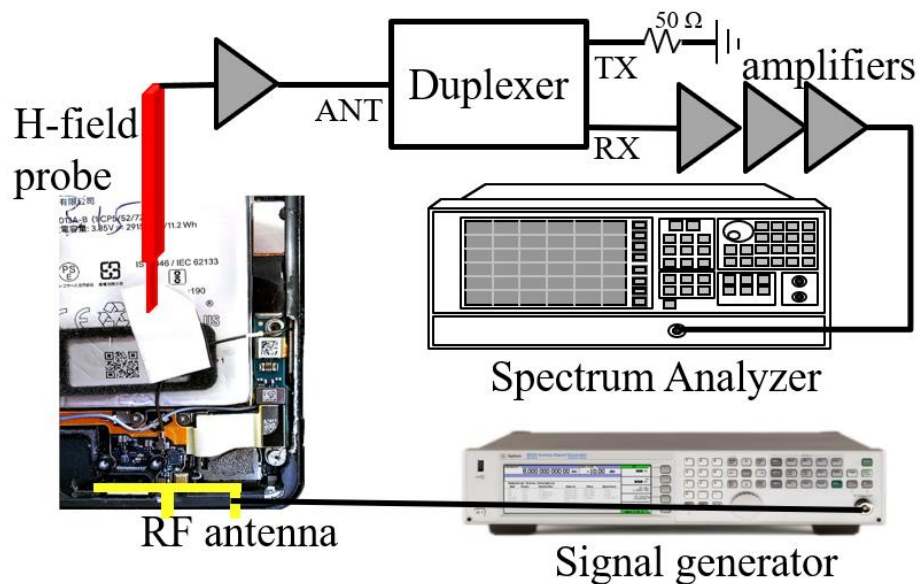
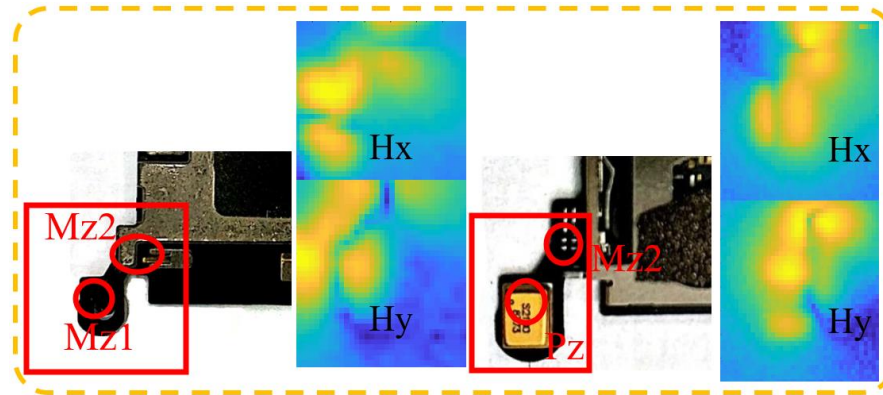


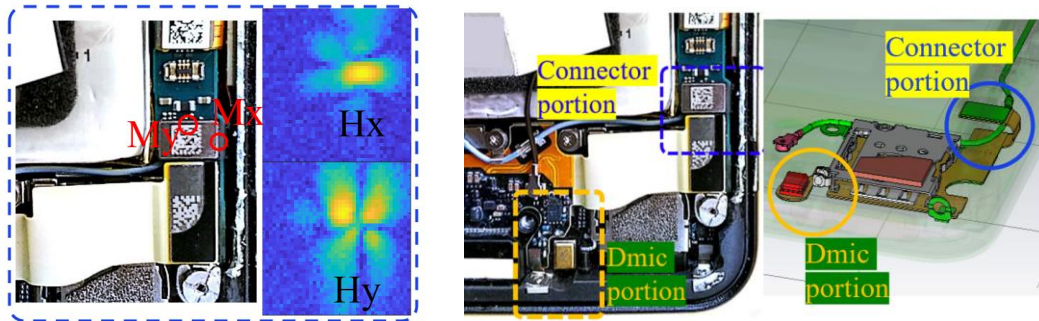
Figure 2. Near field scan measurement setup

With clear understanding of the mechanism through which the modulated sideband signals interfere with the receiving band, the frequencies of the sideband signals can be determined if the frequency of the TX signal is given. To simplify the measured spectrum analysis, a single tone TX signal from a signal generator was used instead of the actual wideband TX. As shown in Figure 2, the signal generator produced a 17 dBm sinusoidal wave injected into a cellphone antenna. The dmic module was turned on. An H-field probe was used to scan the tangential field strength on a certain height plane. The scanning measurement targeted RX frequencies of interest, and the duplexer was added to function as a bandpass filter (specifically for the RX band). The scanned data measured by the spectrum analyzer were converted to field strength with the proper characterization of the field probe [5]. Preliminary sparse scanning results showed that at the target frequencies, the scanned hotspots were located at only two regions: one close to the dmic component and the other near the SIM-flex PCB connector. After the regions of interest were identified, more careful scans were performed in specific locations.

Because of the non-ideal grounding design of the dmic portion, the “clock-to-ground” nets formed a loop (Figure 1 (a) right) that was considered a potential and significant radiator contributing to the EM coupling to the RF antenna nearby. However, the field probe had measurement access to only the region at the connector portion and could not directly characterize the radiated field at the dmic component, because the flexible PCB was buried inside the phone with some depth. In addition, the thickness of the dmic metal shielding shell caused the field radiated from the net-formed-loop on the back side to be un-capturable. Instead, the scanned patterns were obtained in the flipped-out configuration. A previous study has shown a “reference” configuration with the



(a)



(b)

(c)

Figure 3. Scanned H-field patterns, dipole moment types, and locations: (a) two Mz dipoles and one Pz dipole in the dmic portion; (b) Mx and My dipoles in the connector portion; (c) noise sources on the SIM-flex PCB from two regions.

SIM-flex flipped outside of the phone, so that both sides of the dmic have access for near field scan measurement [25] as shown in Figure 3 (a). The connector region was directly measured (Figure 3 (b)).

The scan measurement with the SIM-flex PCB flipped outside enables identification and understanding of all radiating structures in the dmic portion. With the information on the flexible PCB layout, the scanned patterns, and the alignment of the pattern with the layout/dmic component, the two Mz dipole moments can be understood

to be caused by the horizontal loop formed by the clock net and the ground net, whereas the Pz dipole is caused by the vertical displacement current between the dmic die and its metal can. Furthermore, all dipole moments are correlated sources, because they all come from the same clock and TX modulated signal/clock harmonics. In addition, when the SIM-flex is placed back inside the cellphone, there is no metal ground beneath the dmic (because it is too close to the antenna, and the design avoids any additional metal structures nearby); therefore, the three dipole moments remain highly correlated, and do not have image effect to change the dipoles, because of the absence of metal plate beneath the dipole moments [25]. Thus, although the configuration was changed from being flipped out to being placed inside, the sources remained correlated and always shared the same ratios among the three components.

Two types of the spectrum fall within the RX range: the modulated sideband (TX modulation with 9<sup>th</sup> to 20<sup>th</sup> order clock harmonics) spectrum and the spectrum of high-order (363<sup>rd</sup> to 372<sup>nd</sup> order) clock harmonics. As discussed, all noise sources are correlated and share the same ratios between one another. Under the condition that the frequency range of interest is below 900 MHz and the entire dimension of the clock net on the SIM-flex PCB is less than 2.5 cm, all sources are in phase for approximations. Notably, the handling for two types of the spectrum differs. For high-order clock harmonics, the RF current originates from the connector side and propagates all way to the dmic component; therefore, the magnitudes of the dipole moments at the dmic portion should be almost the same for both configurations. However, for the modulated sideband spectrum, the first-step couplings from the antenna to the flexible PCB differ for the two

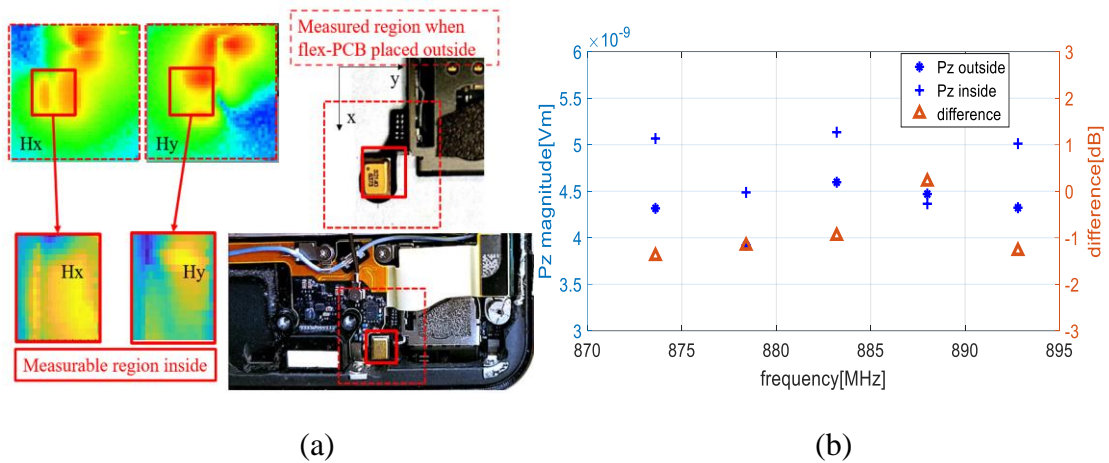


Figure 4. Rescaling the dipole moment magnitudes with the measurements for two configurations: (a) flipped-out and original configurations and the corresponding measured field patterns; (b) measurable Pz dipole (radiating frequency for clock harmonics) extracted from two different configurations.

configurations. Therefore, unlike the high-order clock harmonics, the generated modulation signals had quite different magnitudes between the two configurations.

Measurements were conducted to verify the assumption that the noise sources caused by the high-order clock harmonics had almost the same magnitudes for both cases. As shown in Figure 4 (a), for the flipped-out case, the Pz dipole moment was extracted from the scanned data on the front side of the dmic. For the original case, a small region remained available for near field scanning. Although the measurable area inside cannot provide a complete field pattern, the dipole moment still can be extracted with the obtained partial patterns [26]. As shown in Figure 4 (b), the radiating source Pz was nearly the same in both cases with a less than 2 dB difference. The other two Mz dipole moments, when the SIM-flex was placed inside, were also of the same magnitude (within acceptable error), according to the extracted results from the scanned data for the flipped-out case.

Similar procedures were conducted for the modulated signals: two Mz dipoles and one Pz dipole were extracted from the flipped-out case first. Then with the limited measurable region inside, the Pz dipole was extracted from the partial pattern. Based on the study in [23], in the dmic region, all the three dipole moments are caused by the RF current flowing along the clock net (two Mz dipoles are the horizontal loops and one Pz is the vertical current at the mic component). Small electric dipole (vertical) and its magnetic field strength in the near-field region can be expressed as [27]:

$$\mathbf{H}_{Pz} \approx \mathbf{H}_{Pz,\varphi} = \frac{I_0 l e^{-jkr} \sin \theta}{4\pi r^2} \hat{\varphi} \quad (1)$$

where  $I_0$  is the electric current flowing along the vertical line with length of  $l$ .  $r$  is the radial distance from the observation position to the dipole center. While the dipole moment extractions use the scanned magnetic field strengths, thus, when the current amplitude changes to  $I_0'$ , the magnetic field strength follows:

$$\frac{|H_{Pz}'|}{|H_{Pz}|} = \frac{I_0'}{I_0} = \frac{P_z'}{P_z} \quad (2)$$

Similarly, for small loop dipole, it satisfies:

$$\mathbf{H}_{Mz} \approx -j \frac{I_m l e^{-jkr} \cos \theta}{2\omega \mu r^3} \hat{r} - j \frac{I_m l e^{-jkr} \sin \theta}{4\omega \mu r^3} \hat{\theta} \quad (3)$$

where  $I_m$  is the magnetic current. As the vertically flowing magnetic current is only an equivalence but does not exist, [27] provides the conversion from magnetic current to the real electric current flowing along the loop, expressed as:

$$I_m l = j\omega \mu I_0 S \quad (4)$$

where  $S$  is the loop area. And similarly, the magnetic field and dipole moment strengths will change following the current as:

$$\frac{|H_{M_z'}|}{|H_{M_z}|} = I_m' / I_m = I_0' / I_0 = M_z' / M_z \quad (5)$$

Therefore, as all the three dipoles are driven by the same current on the clock net, it is reasonable to make the assumption that the three dipoles always share the same ratios, the two  $M_z$  dipoles can be extracted by re-scaling, as expressed by equations (6) and (7):

$$M_{Z1\_actual} = M_{Z1\_ref} \frac{P_{Z\_actual}}{P_{Z\_ref}} \quad (6)$$

$$M_{Z2\_actual} = M_{Z2\_ref} \frac{P_{Z\_actual}}{P_{Z\_ref}} \quad (7)$$

where  $M_{Z1\_ref}$ ,  $M_{Z2\_ref}$ , and  $P_{Z\_ref}$  are extracted from the measurement for the flipped-out configuration, and  $P_{Z\_actual}$  is extracted in the original configuration with the partial pattern. As shown in Table 1, there are 3 dipole moments used for the modeling of the noise sources at the dmic part, considering both configurations, the four quantities were known from the near field scan measurement, and the two unknowns were obtained by equations (6) and (7). Thus, all noise sources were successfully modeled as in-phase dipole moments with the correct magnitudes. The equivalent modeling for the noise sources was therefore solved for this practical application by using dipole-moment-based reciprocity.

### 2.3. COUPLING PATH MODELING

Coupling path modeling characterizes the transfer function from the source to the victim structure. By stimulating the victim structure and measurement of the field at the dipole moment location, the source-to-victim coupling path can be found.

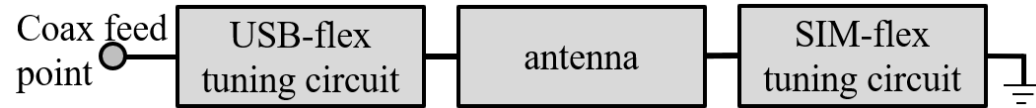
Table 1. Extracted Dipole Moments (@873.6 MHz for example).

Flipped-out configuration		Original configuration	
Dipole moment	Status and magnitude	Dipole moment	Status and magnitude
Pz_ref	Known 3.21e-9 Vm	Pz_actual	Known 5.13e-9 Vm
Mz1_ref	Known 5.65e-12 Am <sup>2</sup>	Mz1_actual	Unknow 9.04e-12 Am <sup>2</sup> (scaled)
Mz2_ref	Known 4.46e-12 Am <sup>2</sup>	Mz2_actual	Unknow 7.14e-12 Am <sup>2</sup> (scaled)

However, the field measurement (exciting the victim antenna) has the same challenge as that in equivalent dipole moment extraction. Because the two Mz dipoles are buried inside the cellphone, access is lacking for probing at the equivalent dipole moment locations. Therefore, the coupling path modeling can rely on only full-wave simulations. As shown in Figure 5 (a), the RF antenna has two tuning circuits to adjust the working frequency range for different bands. Thus, the entire antenna module is complicated. Furthermore, not all EM related properties of the materials used in the product are known, and the full-wave simulation requires more effort to tune.

To construct the correct full-wave simulation models of two tuning circuits on the flexible PCBs, the two PCBs were detached from the phone and soldered with the SMA connectors at the connection points to the antenna structure in Figure 5 (b)(d). Accordingly, the full-wave simulation models for each PCB had the same connectors attached. After adding all lumped elements and tuning of their values, the simulated S-parameters of the circuits eventually matched the measurement results, as demonstrated

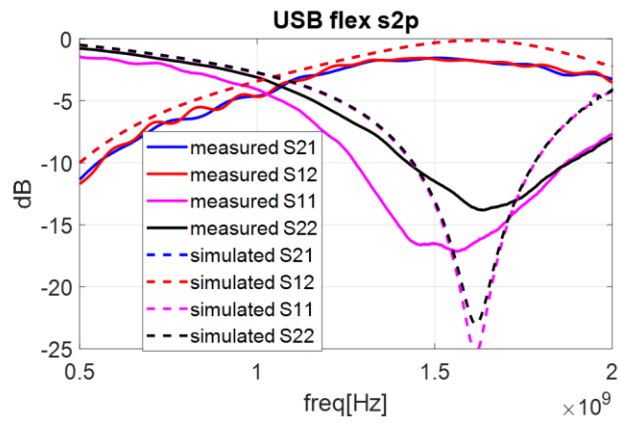
in Figure 5 (c). Thus, the full-wave models of both circuits were prepared for the next step.



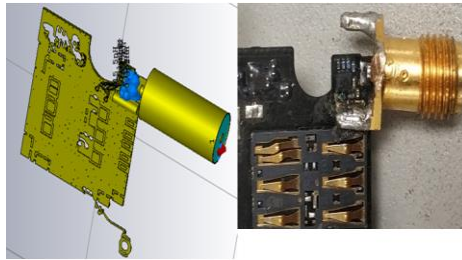
(a)



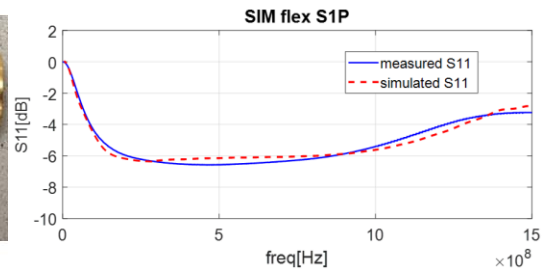
(b)



(c)



(d)



(e)

Figure 5. Modeling of the RF antenna: (a) connection diagram of the working antenna; (b) actual USB-flex tuning circuit and full-wave simulation model; (c) comparison of measured and simulated S-parameters of the USB tuning circuit; (d) actual SIM-flex tuning circuit and full-wave simulation model; (e) comparison of measured and simulated S-parameters of the SIM tuning circuit.

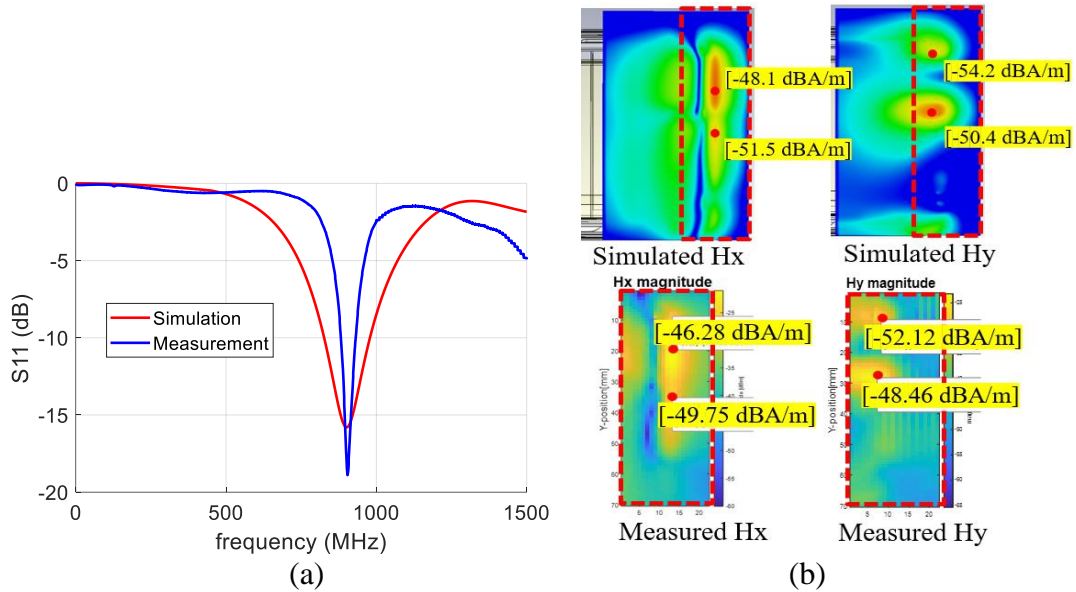


Figure 6. Performance of the whole antenna module: (a) S11 of the antenna (b). near field patterns on the plane above the antenna.

The SMA connectors were then removed from the full-wave simulation models, and all parts were re-assembled according to the connection diagram in Figure 5 (a). Both the S-parameter and the generated near field were then verified for the antenna system. As shown in Figure 6 (a), the full-wave simulation model provided the same resonance frequency of the antenna but did not strictly match the Q-factor. The near field right above the antenna was scanned through measurement and simulation as shown in Figure 6 (b). The field distributions were nearly identical, but the amplitudes had a 2 dB difference, probably because of the inaccurate Q-factor. However, the accuracy of the estimation of the EM coupling from the noise sources to the antenna was fair.

### 3. RF COUPLING QUANTIFICATIONS AND ANALYSIS

The noise sources were modeled with equivalent dipole moments with proper handling of the measured data from two configurations. The coupling paths of the sources to the victim antenna were characterized through a combination of measurement and simulation. After both parts were practically solved, dipole-moment-based reciprocity was applied to quantify the couplings and provide further insights.

#### 3.1. CORRELATIONS

The total coupled RF power was directly measured with a previously described setup [25]. The duplexer was used to inject a mimicked TX signal into the antenna and to provide an RF path allowing the RX spectrum to be measured by a spectrum analyzer. The dipole-moment-based reciprocity provided the estimated coupled voltage on the antenna, according to the expression:

$$U^{fwd} = \frac{Z_L}{2U^{rev}} \left( \sum \overline{E^{rev}} \cdot \vec{P} + \sum \overline{H^{rev}} \cdot \vec{M} \right) \quad (8)$$

where  $U^{fwd}$  is the coupled voltage from the noise source to the victim antenna (the original problem),  $Z_L$  is the load impedance, and  $\vec{P}$  and  $\vec{M}$  are the extracted dipole moments (electric dipole and magnetic dipole, respectively) from the source characterizations by near scanning. For the coupling path, the incident voltage  $U^{rev}$  is excited voltage on the victim antenna; thus,  $\overline{E^{rev}}$  and  $\overline{H^{rev}}$  are the electric and magnetic fields at the dipole moment locations sourced from the victim antenna. As discussed in Section 2, a total of 5 dipole moments were present, and the summation of the couplings for the 5 sources was calculated as shown in Figure 7. The dipole-moment-based

reciprocity captured the trend of the couplings within a certain error. The correlations of the couplings due to high-order clock harmonics were within a 2 dB error. The estimated couplings due to the modulated signals had a less than 4 dB difference with respect to the directly measured results. These larger differences were probably caused by the rescaling procedures in Section 2.

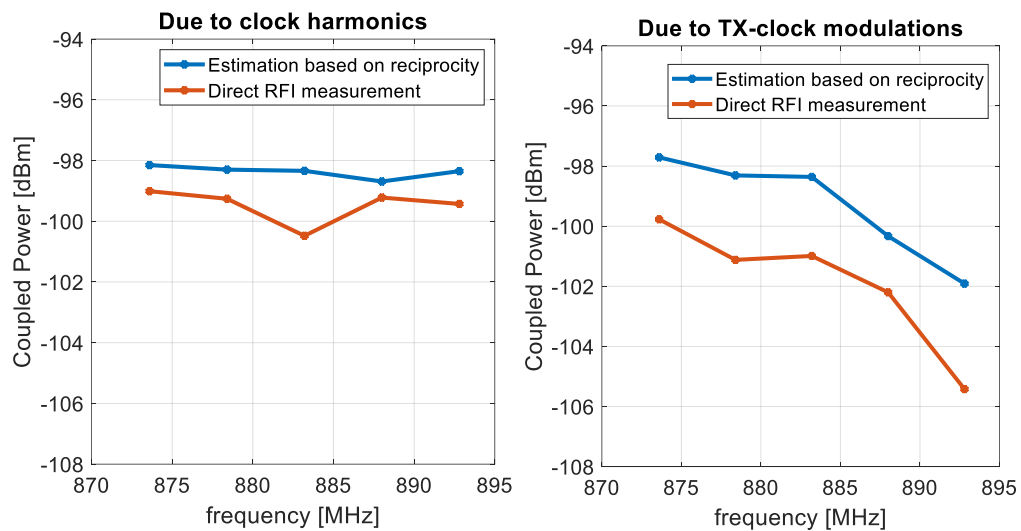


Figure 7. Correlations of the total EM couplings between a direct measurement and reciprocity-based calculations.

It needs to be emphasized that, although the modulated signal couplings have less power than the clock harmonics, in real applications, the modulation involved interference is much more troublesome. First, the RF interference caused by high-order harmonics are irrelevant to the TX power, but the interference by modulation is proportional to the TX power. Because of the limited TX power level from the signal generator, the input TX in the measurement was only 17 dBm but in actual applications can be as high as 23 dBm. Second, the modulated signals are wideband and always

follow the TX channels; therefore, the “contaminated” range cannot be avoided by simply changing the channels.

### 3.2. NOISE COUPLING CONTRIBUTION ANALYSIS

One of the most important benefits from the dipole-moment-based reciprocity theorem is that the couplings from each individual noise sources can be separated. Thus, the interference contributions can be determined for each problematic structure.

Accordingly, engineers can determine the priority of the modifications on each part. For the  $k^{th}$  dipole moment source, its coupling contribution to the victim antenna can be expressed as (9) or (10), for magnetic and electric dipole types respectively:

$$U_k^{fwd} = \frac{Z_L}{2U^{rev}} \overrightarrow{H}^{rev}_k \cdot \overrightarrow{M}_k \quad (9)$$

$$U_k^{fwd} = \frac{Z_L}{2U^{rev}} \overrightarrow{E}^{rev}_k \cdot \overrightarrow{P}_k \quad (10)$$

From (9) and (10), significant noise contributor satisfies two conditions: 1. Strong radiation from the dipole source, 2. Efficient coupling path to antenna. For example, the two horizontal loops, although the source Mz1 is not significantly stronger than Mz2 (see Table 1), however, Mz1 loop is much closer to the antenna and in an efficient coupling orientation, it contributes dominantly and the loop further away is negligible.

The individual coupling contributions after application of reciprocity in this 5-dipole scenario are shown in Figure 8. The dominant interference portion is the dmic region instead of the connector region, because the coupled RF power from the single Mz1 dipole is 10 dB higher than that from the combination of Mx and My in the connector part. The first and second most dominant noise sources are the Mz1 and Pz

dipoles. Therefore, only solving for the layout loop and the metal shell at the dmic is sufficient in practice to suppress RF desensitization.

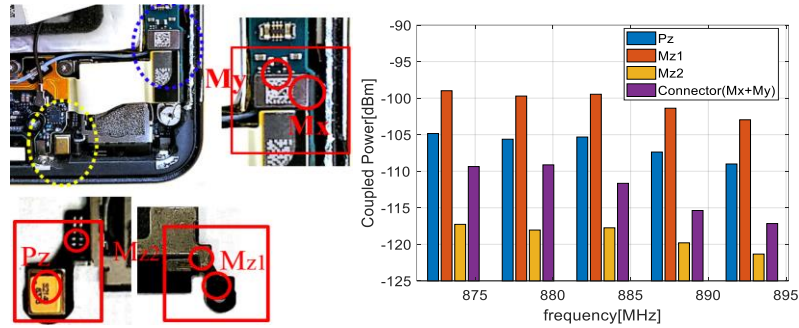


Figure 8. Individual contributions of the noise sources.

#### 4. PRACTICAL RF DESENSITIZATION MITIGATION METHODS

The physics-based dipole moment extraction provided clear understanding of the radiating structures. Reciprocity theorem calculations indicated the priorities of the mitigation solutions by identifying the dominant coupling contributors. With all preparations, mitigation methods can therefore be devised more efficiently.

##### 4.1. SUPPRESSING RADIATION ON DOMINANT NOISE SOURCES

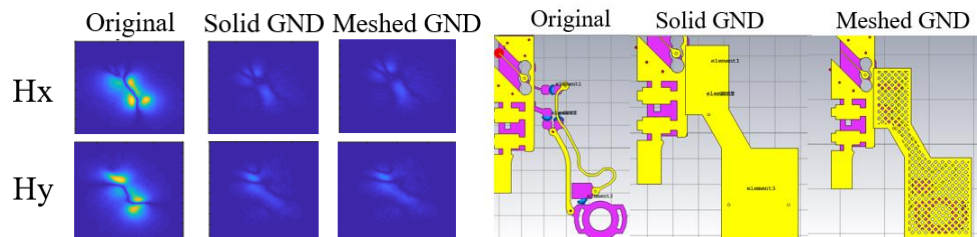


Figure 9. Near-field changes with additional grounding planes.

As indicated by equation (7), the coupling is proportional to the amplitude of the dipole moment. Therefore, RF desensitization can be decreased if the amplitude of the dominant dipole moment is suppressed. From the physics-based dipole moment extractions, the dominant  $M_{z1}$  dipole is caused by the radiating structure formed from the horizontal loop. Thus, a better grounding design can provide a better RF return path to decrease the radiation from the loop. As shown in Figure 9, by simply adding a piece of ground (either solid or meshed) beneath the dmic circuit layout, the generated near field strength can be significantly decreased. As a result, the magnitude of the magnetic dipole moment is greatly suppressed, thus resulting in less coupling to the victim antenna. Although this mitigation method using a better grounding design is efficient for solving the desensitization problem, the additional metal piece added near the RF antenna is likely to detune the antenna. Therefore, this solution is not feasible for after-designed products.

#### 4.2. COUPLING CANCELLATION METHOD

The two dominant contributors are the  $P_z$  and  $M_{z1}$  dipoles; therefore, the coupling calculations in equation (8) can be approximated as:

$$U^{fwd} \approx \frac{Z_L}{2U^{rev}} \left( \overrightarrow{E}_Z^{rev} \cdot \overrightarrow{P}_Z + \overrightarrow{H}_{z1}^{rev} \cdot \overrightarrow{M}_{z1} \right) \quad (11)$$

where  $U^{fwd}$  is the total coupled voltage from the noise source to the victim antenna, and  $Z_L$  is the load impedance.  $\overrightarrow{P}_Z$  and  $\overrightarrow{M}_{z1}$  are the two most dominant dipole moments.  $U^{rev}$  is the incident voltage exciting the victim antenna.

Of note, the sources are correlated because they are all originated from the same

signal, and the couplings from each individual source will have constant phase differences. In addition, under this frequency and dimension, the phase change has been described to be negligible; therefore, the coupled voltages from the sources will be either in-phase or out-of-phase. Equivalently, the coupled voltages will either additively or subtractively form the ultimate total coupled voltage level.

By taking advantage of this aspect, a “negatively” coupled source can be created to balance the total coupling and suppress RF desensitization. As shown in Figure 10 (a), the Mz dipoles are formed by the horizontal loop beneath the dmic circuit (with the original two Mz dipoles marked as black circles). When another ground net is added at the right side, the RF current can be partially distracted by the new ground net; thus, two additional Mz dipoles are formed (blue circles). Then when the balanced ground net is added, the total coupling will change to:

$$U_{balanced}^{fwd} \approx \frac{Z_L}{2U^{rev}} \left[ \overrightarrow{E_Z^{rev}} \cdot \overrightarrow{P_Z} + \overrightarrow{H_{Z1}^{rev}} \cdot \left( \overrightarrow{M'_{Z1}} - \overrightarrow{M''_{Z1}} \right) \right] \quad (12)$$

where  $U_{balanced}^{fwd}$  is the total coupled voltage for the new configuration, the original  $\overrightarrow{M_{Z1}}$  dipole moment is changed to be  $\overrightarrow{M'_{Z1}}$  because of the RF current distribution change, the newly formed dipole is  $\overrightarrow{M''_{Z1}}$  (note that the current flow directions are opposite, so there is a negative sign in equation (12)), and because the distance of the two dipoles is extremely small, the magnetic field for both dipole locations can be approximated to be the same as  $\overrightarrow{H_{Z1}^{rev}}$ . To evaluate the feasibility of this balanced loop cancellation method, the transfer functions for the coupling from the antenna to the dmic circuit were simulated for both con Previous studies have developed a variety of methodologies for solving the RFI problems using near-field scan and reciprocity theory. However, when solving the real

industrial problems, time-consuming measurements are done back and forth to improve the measurement qualities. Based on many hands-on measurements experience and debugging process during this study, an efficient workflow is summarized as Figure 13 shows. Appropriate measures need to be taken based on different scenarios for the best fit of a solution to the problem. As shown in Figure 10 (b), excitation port 1 was set at the coplanar feeding location before injection into the USB tuning circuit. The entire antenna was simulated to radiate as desired. Because the nonlinearity of the dmic component caused the mixing, the up-converted sideband signals were generated at the dmic component location. Therefore, placing the second port right at the clock-ground pins location of the dmic is reasonable.

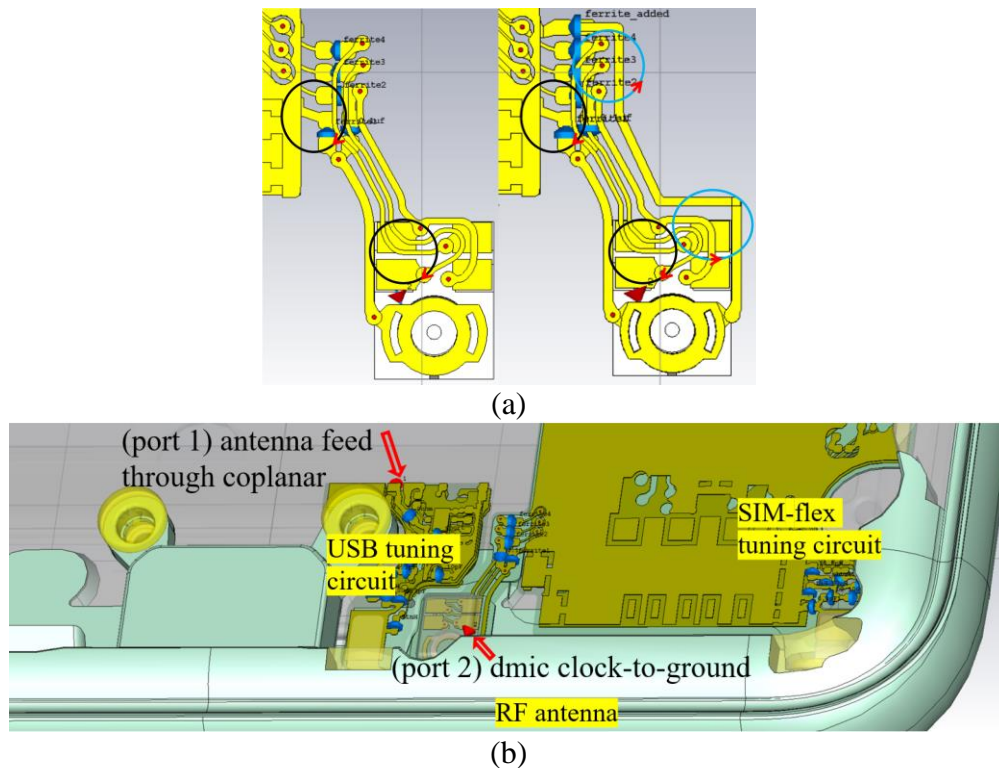


Figure 10. Cancellation method implementation: (a) dmic circuit layout design: original case (left) and with an additional ground net added (right); (b) full-wave simulations for the dmic-to-antenna couplings for the two cases.

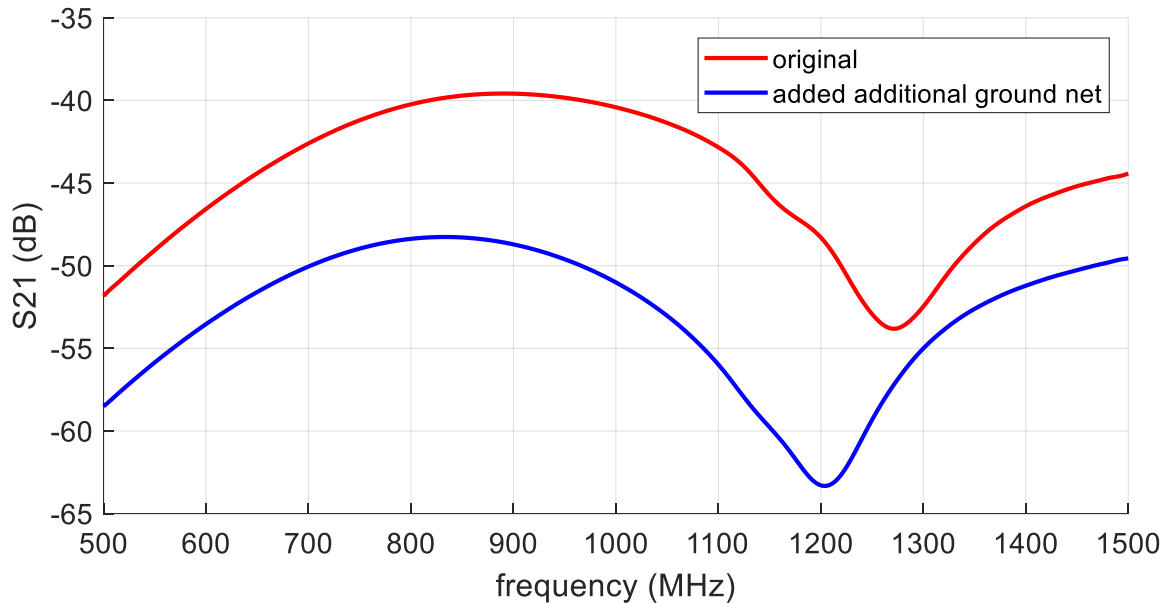


Figure 11. Simulated S21 for the two layout designs of the dmic circuit.

Simulations for both configurations were conducted, and the S21 (antenna-to-dmic) results are shown in Figure 11. By adding the extra ground net, the one-way coupling was decreased by 8 dB. Given that the modulation involved RF desensitization was caused by the round-trip coupling, the total suppression on the couplings should be approximately 16 dB.

### 4.3. NOISE SPECTRUM SUPPRESSION

Beyond the two described methods, because a working dmic needs only a 2.4 MHz clock signal without high requirements on the high frequency components, ferrite beads can be added to decrease the amplitudes of the unwanted and unnecessary harmonics. As shown in Figure 12 (a), the ferrite beads are placed in series on the clock net. By changing the beads to those with larger impedance, both the 9<sup>th</sup> to 29<sup>th</sup> harmonics (20–70 MHz) and 363<sup>rd</sup> to 372<sup>nd</sup> harmonics (869–894 MHz) are significantly suppressed.

As a result, the RF desensitization level can be efficiently decreased and can be measured with the setup shown in Figure 12 (b). As shown in Figure 12 (c), decreases of approximately 8 dB on the 363<sup>rd</sup> to 372<sup>nd</sup> harmonics and approximately 16 dB on the modulated (9<sup>th</sup> to 29<sup>th</sup>, modulated with TX) harmonics were observed.

#### **4.4. SUMMARY FOR RFI PROBLEM SOLVING**

Previous studies have developed a variety of methodologies for solving the RFI problems using near-field scan and reciprocity theory. However, when solving the real industrial problems, time-consuming measurements are done back and forth to improve the measurement qualities. Based on many hands-on measurements experience and debugging process during this study, an efficient workflow is summarized as Figure 13 shows. Appropriate measures need to be taken based on different scenarios for the best fit of a solution to the problem.

This work demonstrated the ability to analyze and solve RF interference problems through application of the dipole-moment-based reciprocity theorem. A sophisticated practical cellphone design was used as an example for demonstration. By taking full advantage of the previous related studies on dipole moment extraction methods, all equivalent dipole moment sources were still successfully modeled even without traditional field scan measurement access. An important advantage of using the reciprocity theorem in scenarios with multiple noise sources is that the individual contributions can be quantified and ranked for the best engineering efficiency. Furthermore, the physics-based dipole moment extractions can provide insights into exactly which structures are troublesome. Thus, the proposed mitigation solutions are reasonable and effective.

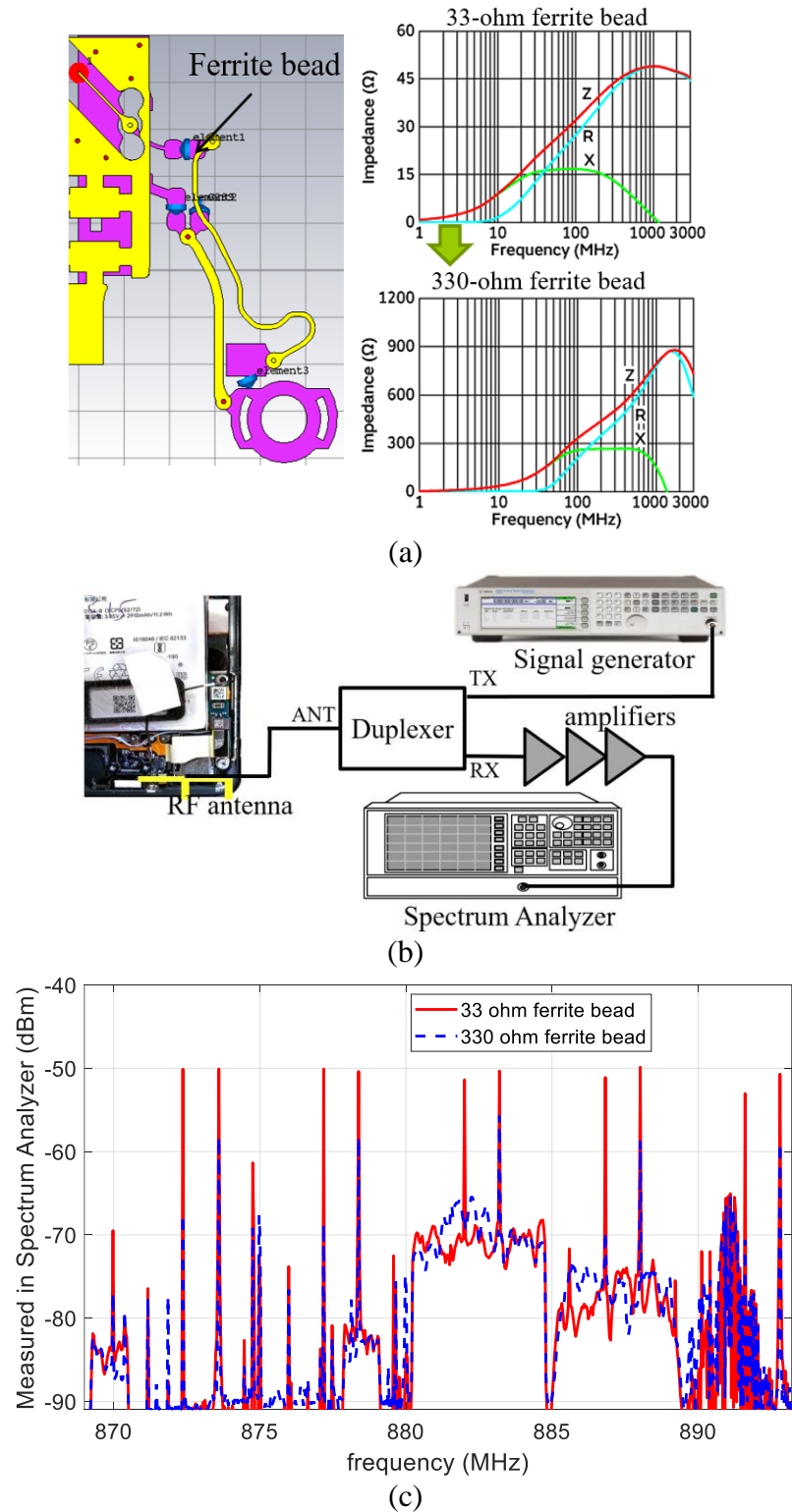


Figure 12. Changing the ferrite beads to better suppress the unwanted spectrum generation: (a) changed ferrite bead on the clock net; (b) validation measurement setup; (c) measured spectrum before and after changing the ferrite bead.

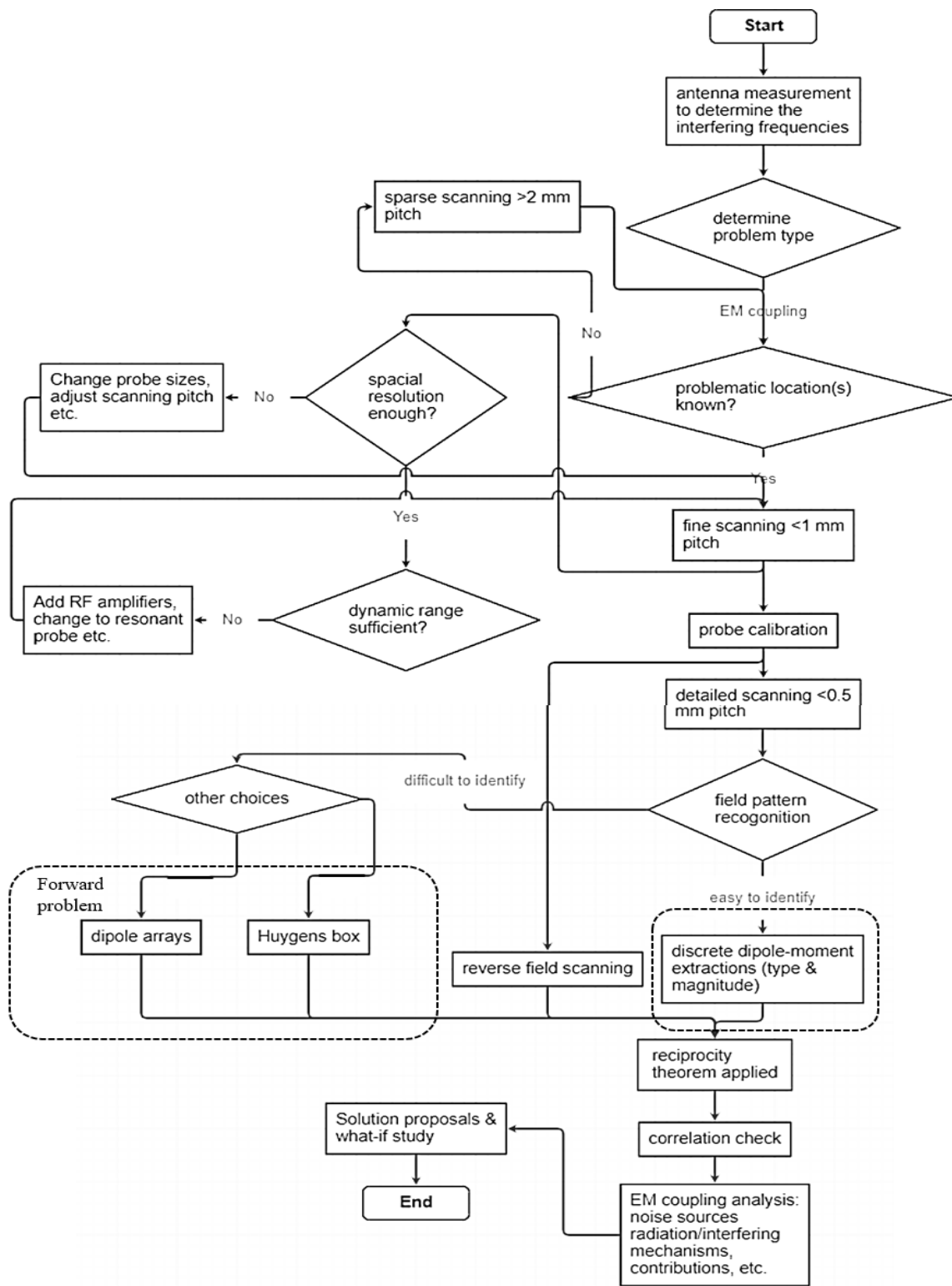


Figure 13. Practical workflow for solving RFI problems.

## 5. DISCUSSIONS

However, the current work has several limitations and lessons:

- 1) The frequency of interest must be relatively low so that the assumption of in-phase noise sources is valid. At higher frequencies, the structure becomes electrically large, and handling remains possible but much more challenging.
- 2) The flipped-out and placed-in configurations share the same sets of dipole moments because of the absence of a conductor beneath the dmic. In more general scenarios, if the configuration is changed, the RF current distributions may change accordingly.
- 3) The slightly poorer accuracy with the rescaled dipole moments might have come from the lack of consideration of the subtle RF current change after the SIM-flex was placed back into the phone.
- 4) Because of the lack of information on materials, extracting the field strengths for such a complicated case from full-wave simulations is typically not recommended, because it takes too much effort.

Dipole moment extraction has been extensively studied over the years. However, in solving real-world problems, clearly determining the underlying physics is essential. Only when the dipole moment type is correlated with the extract physical structure causing the radiation can practical solutions come out reasonably and efficiently.

## REFERENCES

- [1] E. X. Liu, W. J. Zhao, B. Wang, S. Gao and X. C. Wei, "Near-field scanning and its EMC applications," *2017 IEEE International Symposium on Electromagnetic Compatibility & Signal/Power Integrity (EMCSI)*, 2017, pp. 327-332, doi: 10.1109/ISEMC.2017.8077889.
- [2] Y. F. Shu and X. C. Wei, "PCB electromagnetic interference modelling based on reciprocity theorem," *2017 IEEE Electrical Design of Advanced Packaging and Systems Symposium (EDAPS)*, 2017, pp. 1-3, doi: 10.1109/EDAPS.2017.8276939.
- [3] W. Zhang et al., "Improvement on the Accuracy of Near-Field Scanning Using Tangential Electric Field Probe," *2021 IEEE International Joint EMC/SI/PI and EMC Europe Symposium*, 2021, pp. 370-375, doi: 10.1109/EMC/SI/PI/EMCEurope52599.2021.9559226.
- [4] J. Pan, X. Gao and J. Fan, "Identifying Interference From Multiple Noise Sources Using Only Magnetic Near Fields," *IEEE Transactions on Electromagnetic Compatibility*, vol. 63, no. 2, pp. 580-588, April 2021, doi: 10.1109/TEMC.2020.3020049.
- [5] J. Zhang, K. W. Kam, J. Min, V. V. Khilkevich, D. Pommerenke, and J. Fan, "An Effective Method of Probe Calibration in Phase-Resolved Near-Field Scanning for EMI Application," *IEEE Transactions on Instrumentation and Measurement*, vol. 62, no. 3, pp. 648–658, 2013.
- [6] H. Wang, V. Khilkevich, Y. Zhang and J. Fan, "Estimating Radio-Frequency Interference to an Antenna Due to Near-Field Coupling Using Decomposition Method Based on Reciprocity," *IEEE Transactions on Electromagnetic Compatibility*, vol. 55, no. 6, pp. 1125-1131, Dec. 2013, doi: 10.1109/TEMC.2013.2248090.
- [7] J. Pan et al., "Radio-Frequency Interference Estimation Using Equivalent Dipole-Moment Models and Decomposition Method Based on Reciprocity," *IEEE Transactions on Electromagnetic Compatibility*, vol. 58, no. 1, pp. 75-84, Feb. 2016, doi: 10.1109/TEMC.2015.2496210.
- [8] Y. Sun, B. Tseng, H. Lin and C. Hwang, "RFI Noise Source Quantification Based on Reciprocity," *2018 IEEE Symposium on Electromagnetic Compatibility, Signal Integrity and Power Integrity (EMC, SI & PI)*, 2018, pp. 548-553, doi: 10.1109/EMCSI.2018.8495187.
- [9] L. Zhang et al., "Radio-Frequency Interference Estimation for Multiple Random Noise Sources," *IEEE Transactions on Electromagnetic Compatibility*, doi: 10.1109/TEMC.2021.3117845.

- [10] Balanis, C. A. (1997). *Antenna theory: Analysis and design*. Wiley.
- [11] A. Taaghool and T. K. Sarkar, "Near-field to near/far-field transformation for arbitrary near-field geometry, utilizing an equivalent magnetic current," *IEEE Trans. Electromagn. Compat.*, vol. 38, no. 3, pp. 536–542, Aug. 1996. [5] J. Pan, X. Gao, and J. Fan, "Far-field prediction by only magnetic near
- [12] Q. Huang, T. Enomoto, S. Seto, K. Araki, J. Fan, C. Hwang "Accurate and Fast RFI Prediction Based on Dipole Moment Sources and Reciprocity" *Proc. Of DesignCon*, 2018.
- [13] Q. Huang, Y. Liu, L. Li, Y. Wang, C. Wu and J. Fan, "Radio frequency interference estimation using transfer function based dipole moment model," *2018 IEEE International Symposium on Electromagnetic Compatibility and 2018 IEEE Asia-Pacific Symposium on Electromagnetic Compatibility (EMC/APEMC)*, Singapore, 2018, pp. 115-120.
- [14] G. Cho, J. Jin, H. Park, H. H. Park and C. Hwang, "Assessment of Integrated Circuits Emissions With an Equivalent Dipole-Moment Method," *IEEE Transactions on Electromagnetic Compatibility*, vol. 59, no. 2, pp. 633-638, April 2017, doi: 10.1109/TEMC.2016.2633332.
- [15] Q. Huang and J. Fan, "Machine Learning Based Source Reconstruction for RF Desense," *IEEE Transactions on Electromagnetic Compatibility*, vol. 60, no. 6, pp. 1640-1647, Dec. 2018, doi: 10.1109/TEMC.2018.2797132.
- [16] S. Lee et al., "Analytical intra-system EMI model using dipole moments and reciprocity," *2018 IEEE International Symposium on Electromagnetic Compatibility and 2018 IEEE Asia-Pacific Symposium on Electromagnetic Compatibility (EMC/APEMC)*, 2018, pp. 1169-1173, doi: 10.1109/ISEMC.2018.8393972.
- [17] C. Hwang, J. -D. Lim, G. Y. Cho, H. -B. Park and H. H. Park, "A Novel Shielding Effectiveness Matrix of Small Shield Cans Based on Equivalent Dipole Moments for Radio-Frequency Interference Analysis," *IEEE Transactions on Electromagnetic Compatibility*, vol. 58, no. 3, pp. 766-775, June 2016, doi: 10.1109/TEMC.2016.2536139.
- [18] W. Liu, Z. Yan, J. Wang, Z. Min and Z. Ma, "An Improved Equivalent Dipole Moment Source Model Based on Regularization Optimization Method for Near Field-Far Field Conversion," *IEEE Access*, vol. 8, pp. 42504-42518, 2020, doi: 10.1109/ACCESS.2020.2976907.
- [19] Q. Huang et al., "A Novel RFI Mitigation Method Using Source Rotation," *IEEE Transactions on Electromagnetic Compatibility*, vol. 63, no. 1, pp. 11-18, Feb. 2021, doi: 10.1109/TEMC.2020.2995828.

- [20] Y. Sun, H. Lin, B. -C. Tseng, D. Pommerenke and C. Hwang, "Mechanism and Validation of USB 3.0 Connector Caused Radio Frequency Interference," *IEEE Transactions on Electromagnetic Compatibility*, vol. 62, no. 4, pp. 1169-1178, Aug. 2020, doi: 10.1109/TEMC.2019.2925935.
- [21] C. Hwang and Q. Huang, "IC placement optimization for RF interference based on dipole moment sources and reciprocity," *2017 Asia-Pacific International Symposium on Electromagnetic Compatibility (APEMC)*, 2017, pp. 331-333, doi: 10.1109/APEMC.2017.7975497.
- [22] C. Hwang et al., "Noise coupling path analysis for RF interference caused by LCD noise modulation," *2016 IEEE International Symposium on Electromagnetic Compatibility (EMC)*, 2016, pp. 348-352, doi: 10.1109/ISEMC.2016.7571671.
- [23] S. Xia, et al., "RFI Estimation for Multiple Noise Sources Due to Modulation at a Digital Mic Using Dipole Moment Based Reciprocity," *2020 IEEE International Symposium on Electromagnetic Compatibility & Signal/Power Integrity (EMCSI)*, 2020, pp. 1-5, doi: 10.1109/EMCSI38923.2020.9743517.
- [24] C. Hwang, D. Pommerenke, J. Fan, T. Enomoto, J. Maeshima and K. Araki, "Modeling and Estimation of LCD Noise Modulation for Radio Frequency Interference," *IEEE Transactions on Electromagnetic Compatibility*, vol. 59, no. 6, pp. 1685-1692, Dec. 2017, doi: 10.1109/TEMC.2017.2705178.
- [25] C. Hwang, D. Pommerenke, J. Fan, T. Enomoto, J. Maeshima and K. Araki, "Wideband Noise Measurement Technique in Duplex Systems for RF Interference," *IEEE Transactions on Electromagnetic Compatibility*, vol. 60, no. 4, pp. 1038-1044, Aug. 2018, doi: 10.1109/TEMC.2017.2782673.
- [26] L. Zhang et al., "Accurate RFI prediction of 3D non-planar connector with half magnetic dipole pattern," *2019 Joint International Symposium on Electromagnetic Compatibility, Sapporo and Asia-Pacific International Symposium on Electromagnetic Compatibility (EMC Sapporo/APEMC)*, 2019, pp. 770-773, doi: 10.23919/EMCSapporo/APEMC44270.2019.8976328.
- [27] Balanis, C.A. (1997) *Antenna theory: Analysis and design*. New York: Wiley.

## II. CAPACITIVE RADIO FREQUENCY METALLIC CONTACTS FOR LOW PASSIVE INTERMODULATION

### ABSTRACT

Metallic components are widely used in mobile devices for electrical connection purposes, including radio frequency (RF) antenna modules. However, oxidization on the metal surfaces creates nonlinearity and thus generates noticeable passive intermodulation (PIM), particularly when the RF antenna transmits high-power signals. This nonlinearity results in spectrum leakage from the transmitting band to the receiving band, leading to degradation of the receiver's sensitivity (desensitization). In this paper, a capacitive metallic contact solution is proposed and experimentally validated to avoid PIM generation at the metallic contact interface for RF antenna modules.

**Keywords:** Passive intermodulation, Metallic contacts, Radio frequency desensitization, Capacitive contacts, Fabric-over-foam

### 1. INTRODUCTION

Compact and modularized designs have become common in modern electronic devices. Therefore, flexible metallic components such as springs and fabric-over-foam (FOF) contacts are widely used for electrical connections in consumer products. However, it is well known that subtle nonlinearity exists at the metallic contact interfaces because of the presence of an oxidation layer [1]. When high-power radio frequency (RF) current passes through a metal-insulator-metal structure, the subtle nonlinearity causes

passive intermodulation (PIM) generation at the contact interface. The PIM-generated sideband spectrum can leak from the high-power transmitting signals and interfere with the receiving channels, causing RF receiver sensitivity degradation (also known as desensitization) issues in frequency-division-duplex-mode operating systems [2].

Experimental studies on flexible components have shown that significant PIM generation occurs when a contact interface is barely formed [3]. By increasing the contact force/pressure or effective contact area, one can mitigate PIM generation [4]. Utilizing better metal material/surface treatments can also be helpful [5]. However, these solutions may not always be feasible because of cost and manufacturing/assembly constraints.

In this paper, we propose an easy-to-manufacture non-conductive contact to prevent PIM generation causing desensitization, specifically for applications such as RF antenna modules. For RF antennas, a direct current (DC) path is not mandatory, and a good capacitive path may be sufficient for module-to-chassis connections without affecting the normal functions of the antenna modules. In this work, a capacitive contact is realized via an anodization layer, which is thick enough to prevent the tunneling effect while still providing enough capacitance for a low-impedance path in the RF range. Our experiments demonstrate that the proposed RF contacts can achieve an insertion loss similar to that of typical metallic contacts while creating a much lower PIM.

## 2. PROPOSED CAPACITIVE RF CONTACTS

### 2.1. CONCEPT AND IMPLEMENTATION

The tunneling effect, which occurs within a thin oxide layer, is considered to be a dominant nonlinear mechanism in metallic surface contacts [6], [7]. However, the

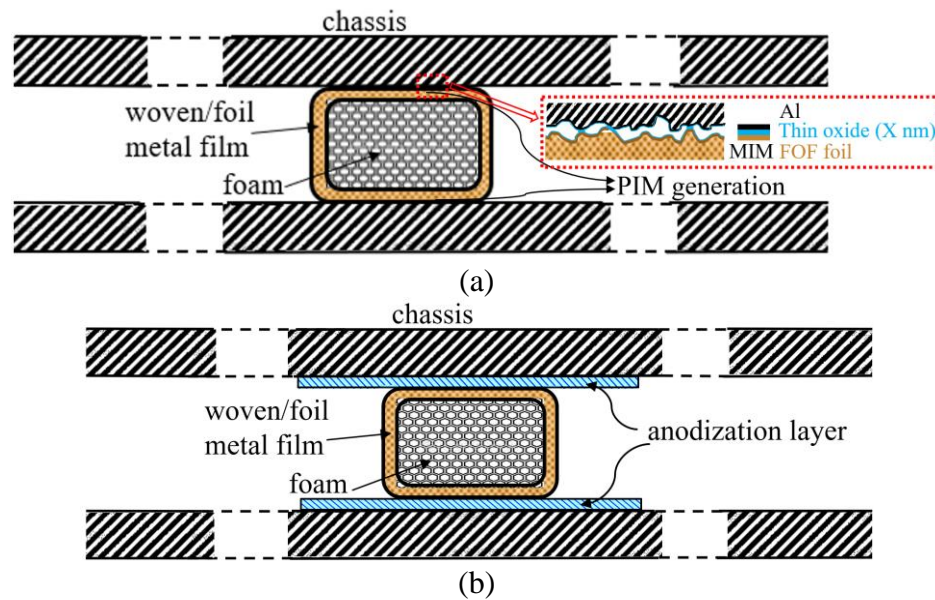


Figure 1. FOF contacts between metal chassis pads: (a) conductive FOF contact, (b) capacitive FOF contact.

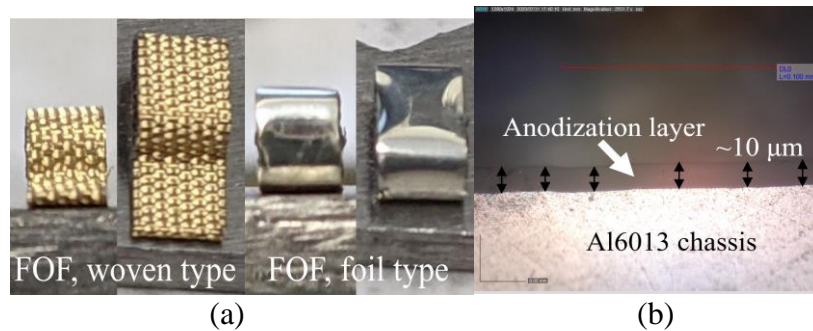


Figure 2. Flexible metallic components and landing substrates: (a) FOF contacts, (b) cross-sectional image of an anodized aluminum alloy.

tunneling effect becomes noticeable only when the oxide layer is thinner than a couple of nanometers. For a thick oxide layer ( $>10$  nm), tunneling through the potential barrier is

significantly reduced, and therefore, PIM generation can be mitigated. However, in this case, the metallic contact interface becomes non-conductive. The RF current can only propagate through the interface by a displacement current (capacitance). Maintaining a good RF connection in the desired frequency range requires the non-conductive contact to have sufficient capacitance to maintain a low-impedance RF connection. This concept of a capacitive RF connection applied to an FOF contact is depicted in Figure 1.

Sufficient capacitance is required to maintain a low impedance in the desired RF range. A small contact area may not provide sufficient capacitance, thus, components with small contact area, such as springs, are not appropriate for the proposed capacitive RF contacts. FOF components, as shown in Figure 2 (a), are more feasible, as their contact area dimensions are in the range of several millimeters. In addition, to achieve a capacitance on the order of tens of picofarads, the insulation layer cannot be greater than tens of micrometers. To achieve this thickness range, an anodization process can be utilized. An anodization layer can be easily and inexpensively manufactured in a massive production setting. Additionally, using a thinner insulator with a higher dielectric constant can also increase the capacitance. In this study, we used Al6013 alloy as an example. The anodization-formed aluminum oxide is only approximately 10  $\mu\text{m}$  thick, as shown in Figure 2 (b).

## **2.2. PIM MEASUREMENT VALIDATION**

As shown in Figure 3, there are two sinusoidal waves within the TX band (790 and 815 MHz) of the duplexer (in this setup, the duplexer is for LTE band 20, TX: 790~820 MHz, RX: 832~862 MHz). The two tones propagate through the test vehicle

from the “ANT” port to the low-PIM 50- $\Omega$  termination. The test fixture is loaded with the FOF contact and landing pads. The generated 3<sup>rd</sup> order inter-product (IP3) propagates backward and is captured by the spectrum analyzer from the “RX” port. As the prototype has been automated with a linear actuator (to control the gap) and a force gauge (to monitor the contact force), multiple quantities, including the force, IP3, and displacement distance, will be recorded for various contact conditions [8].

For each step of the actuator’s movement, the force and IP3 are recorded simultaneously. Figure 4 demonstrates the advantage in PIM suppression achieved by using a capacitive path rather than a conductive path. It can be observed that for the conductive contact, the PIM is reduced to a low level only when the FOF contact compression reaches a force higher than 20 g. In contrast, for a non-conductive contact, there is no requirement on the compression force/gap, and a low level of PIM is always achieved. Thus, adopting a non-conductive contact can be an efficient way to dramatically reduce the generation of PIM.

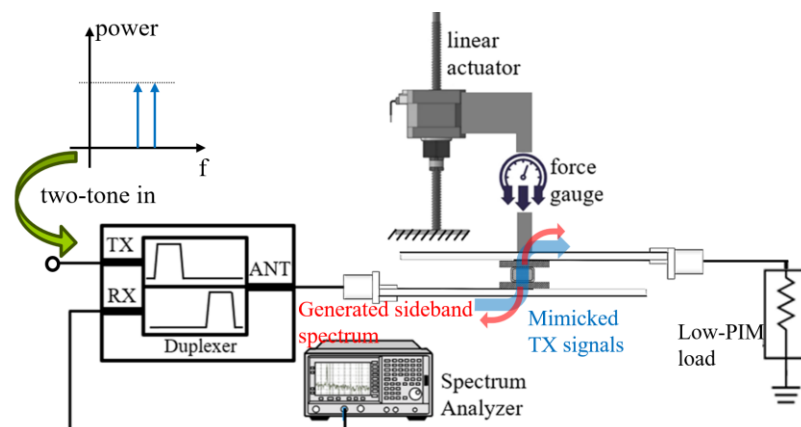


Figure 3. Two-tone PIM test platform for flexible metallic components.

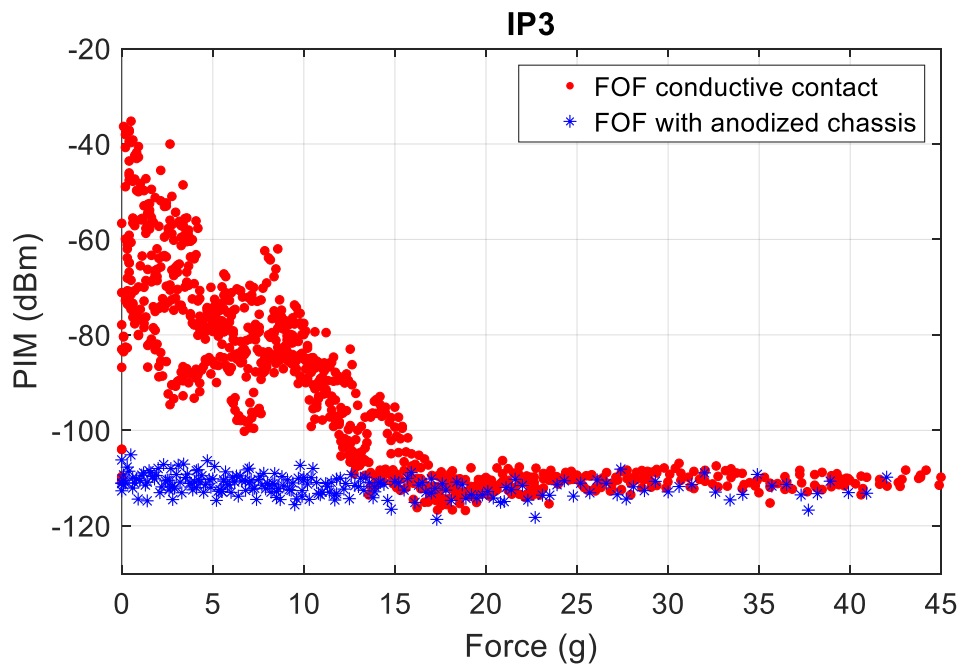


Figure 4. Measured force–PIM results of FOF contacts with conductive (etched) and non-conductive (anodized) Al6013 pads.

### 2.3. EVALUATION OF THE CONTACT IMPEDANCE

The simplified equivalent circuit of the FOF component can be either serial-RL (conductive contact) or serial-LC (capacitive contact). The only difference between the two types of contacts is that the contact resistance at the interfaces is replaced by the capacitance when the system switches from conductive to non-conductive. The parasitic inductance dominates the impedance at a higher frequency range and is more strongly associated with the FOF component shape itself and the gap. Hence, the inductance extraction is not critical. For the non-conductive contact, extracting the capacitance is important because it dominates the low-frequency impedance. When the contact type switches to be non-conductive, a sufficient capacitance is required to ensure that the insertion loss of the contact can remain low at frequencies above 600 MHz.

The parallel-plate capacitor calculation is an approximation, and because of the presence of non-ideal conditions, such as the woven texture on the FOF surface, FOF deformation during compression, potential air gap, etc., the capacitance extraction should still rely on measurement results. Because FOF contacts for electrical connections typically have small impedances, the two-port shunt topology is appropriate for building a test fixture [8]. As shown in Figure 5 (a), with two transmission lines on the two ends, the contact will be made in a shunt connection. The realization of this topology can

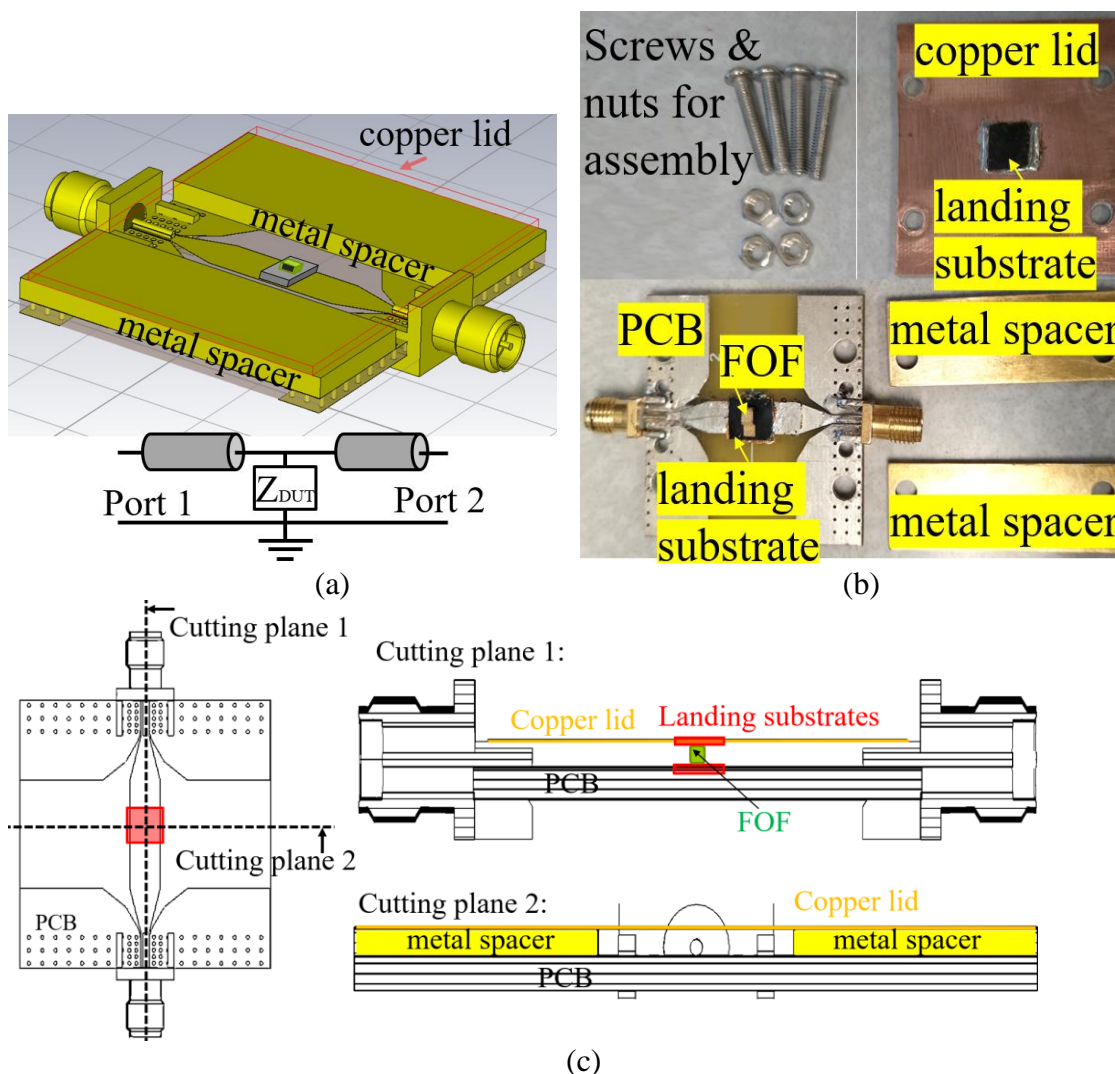


Figure 5. Two-port shunt topology test fixture for contact characterization: (a) test fixture model demonstration, (b) test fixture assembly, (c) detailed placement of the parts.

be achieved by using a printed circuit board (PCB) with two metal spacers and one metal lid, as shown in Figure 5 (b). When the parts are assembled as indicated in Figure 5 (c), all metal parts (ground on PCB, metal spacers, and copper lid) serve as the RF return path, except for the trace on the PCB and the inner pins of the SMA connectors. The test device's shunt connection will be made by touching both the trace and the lid. The 2x-thru de-embedding process [9] was used to eliminate the fixture's effect and to extract only the characteristics of the contact. The impedance of the contact can then be extracted [10,11].

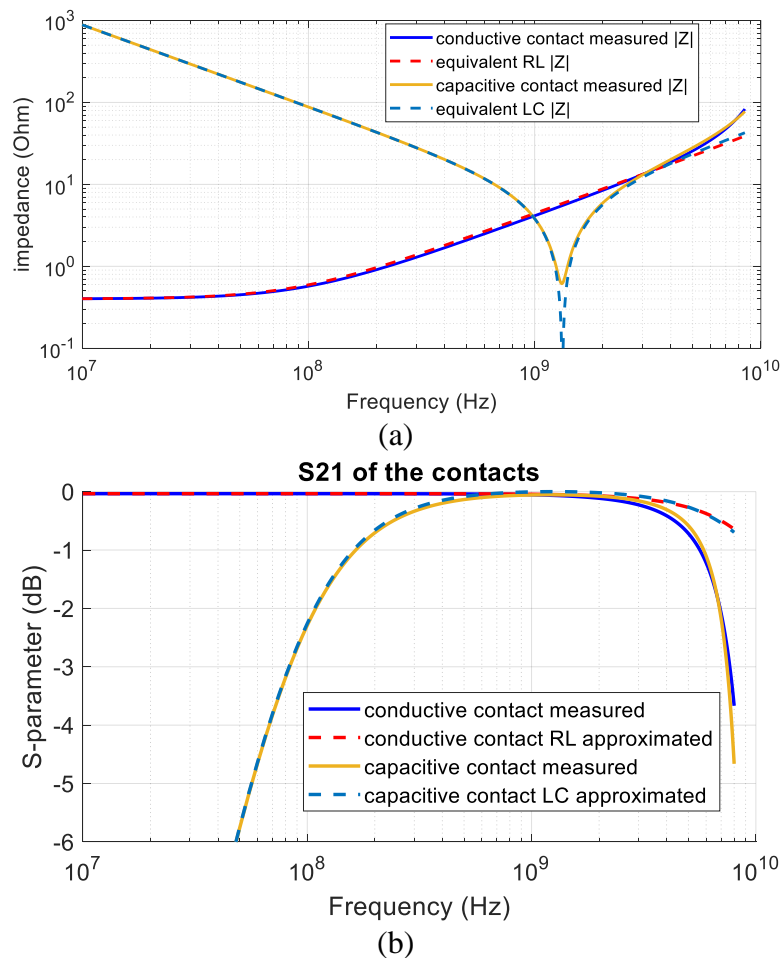


Figure 6. Contact evaluations of measured and extracted equivalent circuits: (a) impedance, (b) insertion loss.

The impedance of the contact can be obtained as shown in Figure 6 (a). From the impedance curve, the equivalent lumped serial-RLC circuit can be used to fit the measured curve, and the capacitance value can be extracted. It needs to be emphasized that the impedances shown in Figure 6 (a) are extracted with two-port shunt connection topology, while the S-parameters (shown in Figure 6 (b)) of the contacts are presented in the two-port series impedance topology. Figure 6 (b) shows the insertion losses of the impedances. Because the lumped RLC approximations are excessive simplifications, the equivalent representations can only work up to several gigahertz. The two-port shunt test fixture also limits the measurable range owing to the cavity resonance at higher frequency.

More configurations were measured following the same workflow, and the extraction results are summarized in Table 1.

Table 1 Capacitance Extraction Results

Test configuration (FOF + insulator)	Capacitance extracted from measurement	Parallel-plate estimation
O-shape foil+ anodized Al6013	12 pF	22 pF
P-shape woven+ anodized Al6013	14 pF	30 pF
O-shape foil+ 3 mil Kapton tape	1.1 pF	2.1 pF
P-shape foil+ 3 mil Kapton tape	1.5 pF	2.5 pF

It can be seen from Table 1 that the parallel-plate approximations overestimate the actual capacitance in each case. This result is most likely due to the small air gap

between the layers. Furthermore, not all of the insulation methods work well.

Anodization is a more feasible solution for providing a capacitive RF connection. Thus, it is critical to choose an appropriate dielectric material and thickness in order to have sufficient capacitance for the RF connection.

### 3. CONCLUSION

A non-conductive RF path for electrical connections between an RF antenna module and metal chassis has been proposed for solving the desensitization issue caused by PIM. The proposed solution exhibited a dramatic reduction in PIM. A two-port shunt test fixture was used to extract the equivalent circuit for FOF contacts. This study has demonstrated the feasibility of using a capacitive path without sacrificing RF performance in the desired frequency range. Appropriate selections of insulating material and thickness are critical to meet the minimum capacitance requirement.

### REFERENCES

- [1] Simmons, J. G. et al., "Generalized Formula for the Electric Tunnel Effect between Similar Electrodes Separated by a Thin Insulating Film," *Journal of Applied Physics*, 34(6), 1793–1803. Doi: 10.1063/1.1702682
- [2] H. Yang, H. Wen, Y. Qi and J. Fan, "An Equivalent Circuit Model to Analyze Passive Intermodulation of Loose Contact Coaxial Connectors," *IEEE Transactions on Electromagnetic Compatibility*, vol. 60, no. 5, pp. 1180-1189, Oct. 2018, doi: 10.1109/TEMC.2018.2794992.
- [3] J. Li et al., "Self-contact Introduced Passive Intermodulation Characterizations for Captured Springs," *2021 IEEE International Joint EMC/SI/PI and EMC Europe Symposium, Raleigh, NC, USA, 2021, pp. 929-934, doi: 10.1109/EMC/SI/PI/EMCEurope52599.2021.9559265.*

- [4] S. Xia et al., "Passive Intermodulation Under Different Spring Contact Conditions," *2022 IEEE International Symposium on Electromagnetic Compatibility & Signal/Power Integrity (EMCSI), Spokane, WA, USA, 2022*, pp. 12-16, doi: 10.1109/EMCSI39492.2022.9889661.
- [5] J. R. Wilkerson, P. G. Lam, K. G. Gard and M. B. Steer, "Distributed Passive Intermodulation Distortion on Transmission Lines," *IEEE Transactions on Microwave Theory and Techniques*, vol. 59, no. 5, pp. 1190-1205, May 2011, doi: 10.1109/TMTT.2011.2106138.
- [6] Holm, R. (1951). Errata, "The Electric Tunnel Effect across Thin Insulator Films in Contacts," *Journal of Applied Physics*, 22(9), 1217-1217. Doi:10.1063/1.1700142
- [7] J. J. Henrie, A. J. Christianson and W. J. Chappell, "Linear-Nonlinear Interaction and Passive Intermodulation Distortion," in *IEEE Transactions on Microwave Theory and Techniques*, vol. 58, no. 5, pp. 1230-1237, May 2010, doi: 10.1109/TMTT.2010.2045527.
- [8] S. Xia et al., "Practical Fixture Design for Passive Intermodulation Tests for Flexible Metallic Contacts," *2022 IEEE International Symposium on Electromagnetic Compatibility & Signal/Power Integrity (EMCSI), Spokane, WA, USA, 2022*, pp. 17-22, doi: 10.1109/EMCSI39492.2022.9889578.
- [9] B. Chen, J. He, Y. Guo, S. Pan, X. Ye and J. Fan, "Multi-ports ( $[2n] 2\times$ -thru de-embedding: theory, validation, and mode conversion characterization," *IEEE Transactions on Electromagnetic Compatibility*, vol. 61, no. 4, pp. 1261-1270, Aug. 2019, doi: 10.1109/TEMC.2019.2908782.
- [10] J. Jeon, H. Lee, B. Pu, J. -H. Kim, N. Zhang and W. Nah, "Prediction of Impedance Characteristics of MLCC Using Multiconductor Transmission Line Theory," *IEEE Transactions on Electromagnetic Compatibility*, vol. 58, no. 6, pp. 1760-1771, Dec. 2016, doi: 10.1109/TEMC.2016.2588519.
- [11] L. E. Wojewoda, M. J. Hill, K. Radhakrishnan and N. Goyal, "Use Condition Characterization of MLCCs," *IEEE Transactions on Advanced Packaging*, vol. 32, no. 1, pp. 109-115, Feb. 2009, doi: 10.1109/TADV.2008.2004811.

### III. SIDEBAND SPECTRUM ESTIMATIONS BASED ON TWO-TONE PASSIVE INTERMODULATION CHARACTERIZATION

#### ABSTRACT

Passive intermodulation (PIM) has been identified as a nonlinear distortion mechanism in metallic contacts. This subtle nonlinear distortion—generated in non-ideal contact interfaces such as springs, conductive foams, or tapes—causes spectrum leakage from the transmitting (TX) to the receiving frequency range. The leaked frequency component contaminates the receiving channel and degrades the receiving sensitivity of the radio frequency antenna (a condition called the desense problem). Although two-tone tests are often used for measurement characterization in PIM studies, the link between tone tests and broadband sideband is unclear. Moreover, the sideband generation causing desense in a frequency division duplex system may be associated with IM3 as well as higher-order IM components, depending on various settings such as the TX bandwidth and duplex spacing. Therefore, a link must be established to correlate two-tone results with wideband sideband spectrum levels. Herein, sideband calculation using measured broadband TX signals was validated, and a mathematical model with reasonable simplification is provided to link the two-tone test results to the broadband PIM spectrum.

**Keywords:** desense, radio-frequency interference, two-tone test, PIM, wideband spectrum.

## 1. INTRODUCTION

Degradation on the receiving sensitivity of a radio frequency (RF) antenna (also known as desense) has become a challenging engineering problem for current electronic devices with wireless communication functions [1]. With the trend toward more compact and modularized electronic device designs, metallic contacts (such as springs and conductive foams/tapes) inside devices are frequently used to facilitate assembly during mass production. However, those metallic contacts cannot always be considered ideal electrical connections. Because of the presence of many non-ideal factors, the metallic contact interfaces may potentially contain a thin oxide layer [2],[3], corrosion, or surface roughness causing constriction of contact points. Moreover, metallic contacts may have subtle nonlinearity properties caused by quantum tunneling [4-6], electro-thermal effects [7], or other nonlinear mechanisms [8-10]. This nonlinearity can distort the transmitting (TX) signals and create new frequency components in the harmonic and sideband ranges. In frequency division duplex (FDD) systems, focus is placed on sideband spectrum generation due to passive intermodulation (PIM). When an electronic device transmits high-power signals, PIM causes spectrum leakage from the TX range to the adjacent receiving (RX) frequency range, thus resulting in desense problems.

PIM characterization methods are critical for quantifying the nonlinearity and guiding mitigation of desense caused by PIM. The most commonly used PIM characterization method is the two-tone test [11],[12], in which high-power sinusoidal waves are used to mimic the TX signal, and the intermodulation (IM) products typically serve as the figure of merit to quantitatively characterize the PIM level [13]. Duplexer-

based two-tone measurements with proper fixture designs can be used to characterize both the mechanical and electrical behaviors of the flexible metallic contacts [14]. Although two-tone based measurement can clearly indicate nonlinearity trends (or even quantitative comparisons [15]), the exact relationship between the IM level and the desense level remains unclear. Whereas the actual TX signals are wideband, the PIM-created sideband spectrum is also wideband. Furthermore, depending on various settings (e.g., TX bandwidth, channel, and power) or the bands (frequency range or duplex spacing), the sideband noise spectrum may be associated with higher-order or even multiple IM products. Therefore, establishing a link between the typical two-tone test results and the actual desense levels caused by wideband TX signals is critical.

Herein, we discuss calculations for converting the two-tone results into a wideband spectrum, and we subsequently determine the RX noise power. A mathematical representation of the nonlinear component using a polynomial I-V expression based on characteristics extracted from two-tone measurements is provided. Frequency-domain convolutions with trimmed spectra can be used to numerically determine the sideband spectrum generated by PIM. With appropriate approximations, the spectrum model can be simplified and explicitly expressed; thus, the closed-form equations can be derived to determine the sideband spectrum. Herein, this sideband spectrum estimation is experimentally validated with both the metallic conductive foam component and a tunable nonlinear source fixture.

## 2. PIM ESTIMATION

In this section, the two-tone case is briefly introduced to explain the measurement characterization of the nonlinear component. The extracted characteristics from the two-tone measurement are subsequently used for broadband calculations.

### 2.1. TWO-TONE CASE

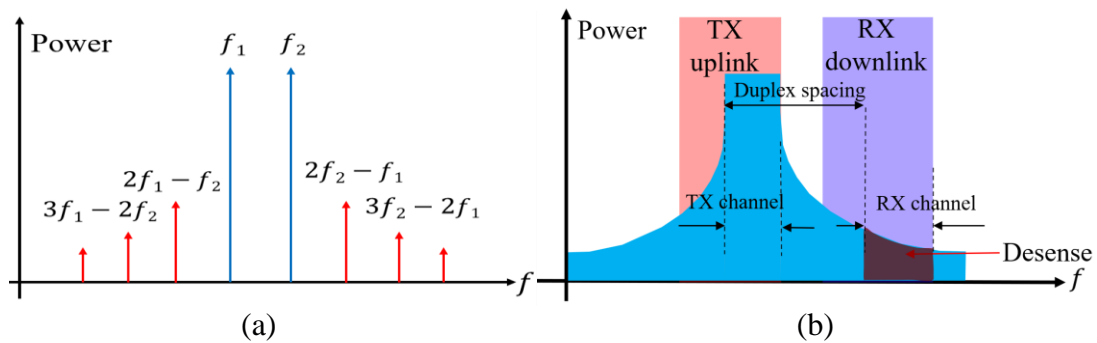


Figure 1. Generation of different sideband spectra: (a) two-tone TX and sideband IM products; (b) wideband TX signals and desense problem demonstration.

The two-tone test has been used primarily for qualitative PIM characterization. A duplexer-based two-tone test system [14] can provide a good measurement dynamic range, by separating the high-power TX and low-power RX into different paths. With the capability of high-dynamic range measurement, the two-tone measured results (sideband IM products shown in Figure 1 (a)) can be used to establish a nonlinear model. The established model is expected to be able to determine the broadband PIM spectrum within the RX channel (Figure 1 (b)).

A nonlinear component is naturally represented by an I-V relationship [16],[17]. The nonlinear I-V curve can be expressed as a polynomial expansion [18] to indicate the

sideband generation characteristics:

$$V_{\text{out}} = a_0 + a_1 I_{\text{in}} + a_2 I_{\text{in}}^2 + a_3 I_{\text{in}}^3 + \dots \quad (1)$$

where  $V_{\text{out}}$  is the output voltage of the nonlinear component when an input current  $I_{\text{in}}$  is provided. Because only odd-order polynomial coefficients (except for  $a_1$ , indicating the DC resistance) are associated with the sideband frequency components, the even-order coefficients are ignored in the expression. The odd-order coefficients can be found from the two-tone measurement. When two sinusoidal waves with equal amplitude are injected into the component, equation (1) can be re-written as:

$$\begin{aligned} V_{\text{out}}(t) = & a_1 I_0 (\cos \omega_1 t + \cos \omega_2 t) + \\ & a_3 I_0^3 (\cos \omega_1 t + \cos \omega_2 t)^3 + a_5 I_0^5 (\cos \omega_1 t + \cos \omega_2 t)^5 \\ & + a_7 I_0^7 (\cos \omega_1 t + \cos \omega_2 t)^7 \dots \end{aligned} \quad (2)$$

where  $I_0$  is the peak current amplitude of either tone. The expansion of equation (2) consists of more than only sideband IM products. After expansion of equation (2) and keeping only the lower-side (or higher-side) IM product terms, the polynomial expansion is changed to:

$$\begin{aligned} V_{\text{out}}(t) = & a_1 I_0 (\cos \omega_1 t + \cos \omega_2 t) + \dots \\ & + \frac{3}{4} a_3 I_0^3 \cos(2\omega_2 t - \omega_1 t) + \dots \\ & + \frac{5}{8} a_5 I_0^5 \cos(3\omega_2 t - 2\omega_1 t) + \dots \\ & + \frac{35}{64} a_7 I_0^7 \cos(4\omega_2 t - 3\omega_1 t) + \dots \end{aligned} \quad (3)$$

The coefficients can be extracted from the two-tone IM product power measured with the spectrum analyzer. For instance, if the spectrum analyzer indicates a  $P_{\text{IM5}}$

(frequency at  $f = (3\omega_2 - 2\omega_1)/2\pi$ ) from the duplexer-based system [14], then the following is satisfied:

$$2P_{\text{IM5}} = \frac{V_{\text{IM5}}^2}{2Z_0} \quad (4)$$

$$V_{\text{IM5}} = \frac{5}{8}a_5I_0^5 \quad (5)$$

where  $Z_0$  is the input impedance of the spectrum analyzer ( $Z_0 = 50 \Omega$ ), and  $V_{\text{IM5}}$  is the generated voltage at IM5 frequency. Of note, equation (4) considers twice the power, because the spectrum analyzer in Figure 1 captures only half the power of the generated IM products. By combining equations (4) and (5), we can extract the coefficient  $a_5$  from:

$$a_5 = \frac{16\sqrt{Z_0P_{\text{IM5}}}}{5I_0^5} \quad (6)$$

Similarly, all other orders of the coefficients can be found with the same method. With the polynomial coefficients extracted, the I-V expressed nonlinearity represents the nonlinear distortion generated sideband IM products.

Notably, the coefficient extraction in equations (2)–(6) is based on the assumption that the input current amplitude across the nonlinear component equals the TX current. However, this assumption is valid only when the discontinuity at the PIM source location is negligible in the RF path. Given that most of the metallic contacts have relatively small DC resistance values (much less than  $50 \Omega$ ), this assumption is reasonable. In addition, the two-tone frequency domain measurement has better accuracy than static I-V measurement [16] for the purposes of sideband spectrum estimation. However, the two-tone IM product reconstructed I-V preserves only the nonlinear characteristics for sideband generation but omits other nonlinear behaviors such as harmonic generation.

## 2.2. BROADBAND CASE

Although two-tone based measurement (Figure 1 (a)) facilitates characterization of PIM, the desense level (or the in-channel RX noise power) remains unclear. As demonstrated in Figure 1 (b), when the TX signal is wideband, the PIM-created sideband leakage is also broadband, and the noise spectrum within the RX channel accounts for the desense level. Notably, although error vector magnitude is a standard measurement [19] to quantify unwanted TX emissions, it is expressed as a percentage and does not contain the detailed spectrum distribution over the frequency. Thus, it is not suitable for quantifying desense problems, because the RX noise power has an enormous difference in amplitude with respect to the TX power, and the integration of the RX noise power must be specified in a certain frequency range.

When a cellphone emulates the LTE band TX signals, the TX spectrum consists of many small tones with random phases and with 1 KHz spacing for the adjacent tones (as shown and discussed in Section 3). When transmitting a 20 MHz bandwidth TX signal (for example, LTE band 20, TX: 830–850 MHz, 23 dBm herein), a total of 20,001 tones are occupied and distributed within the 20 MHz range.

After the polynomial coefficients are obtained from the two-tone measurement discussed in Section 2, equation (1) can be used to express the generated nonlinear voltage when the input TX current is:

$$I_{\text{in}}(t) = I_1 \cos(\omega_1 t + \varphi_1) + I_2 \cos(\omega_2 t + \varphi_2) + \dots + I_N \cos(\omega_N t + \varphi_N), \quad (7)$$

where  $N$  is the total number of tones within the TX range. First, when  $N=2$ , the phases of the two tones do not substantially affect the IM product amplitudes; however, with the involvement of more tones, the IM products generated by different combinations of tones

can “stack up” in the same frequency point; thus, the phase terms can have noticeable effects on the sideband spectrum power level. A direct solution for this nonlinear problem is to generate a time-domain current waveform consisting of all tones, as expressed in equation (7). The nonlinear distorted waveform can be found with equation (1) and then converted into the frequency domain to determine the sideband spectrum. However, this brute-force calculation poses a heavy computational burden. For the record length and sampling rate of the waveform, to satisfy the Nyquist frequency and distinguish the adjacent tones with 1 KHz spacing, the following conditions must be satisfied:

$$f_s > 2f_{\max}, f_{\text{resolution}} = \frac{f_s}{N_{\text{rec}}} < f_{\text{spacing}}, \quad (8)$$

where  $f_s$  is the sampling frequency,  $f_{\max}$  is the maximum frequency of the TX signal (herein, for LTE band 20,  $f_{\max} = 860 \text{ MHz}$ ),  $f_{\text{spacing}} = 1 \text{ KHz}$ , and  $N_{\text{rec}}$  is the record length of the waveform. The minimum requirement for  $N_{\text{rec}}$  is 1.72 million—an enormous data size. Whereas the sampling frequency is typically selected to be more than just twice the maximum frequency, the waveform is commonly several million or even tens of millions of data points. Therefore, the multiplications (exponentiations) in equation (1) are computationally expensive, and a lighter computational alternative is needed.

Instead of calculating in the time domain to account for the multiplications/exponentiation in equation (1), frequency-domain convolution can be used as the equivalence:

$$F\{I_{\text{in}}^m(t)\} = I_{\text{in}}(f) * I_{\text{in}}(f) * \dots * I_{\text{in}}(f) = I_{\text{in}}(f)^{*m} \quad (9)$$

where  $m$  is the order of the exponentiation. Notably, the time to frequency domain

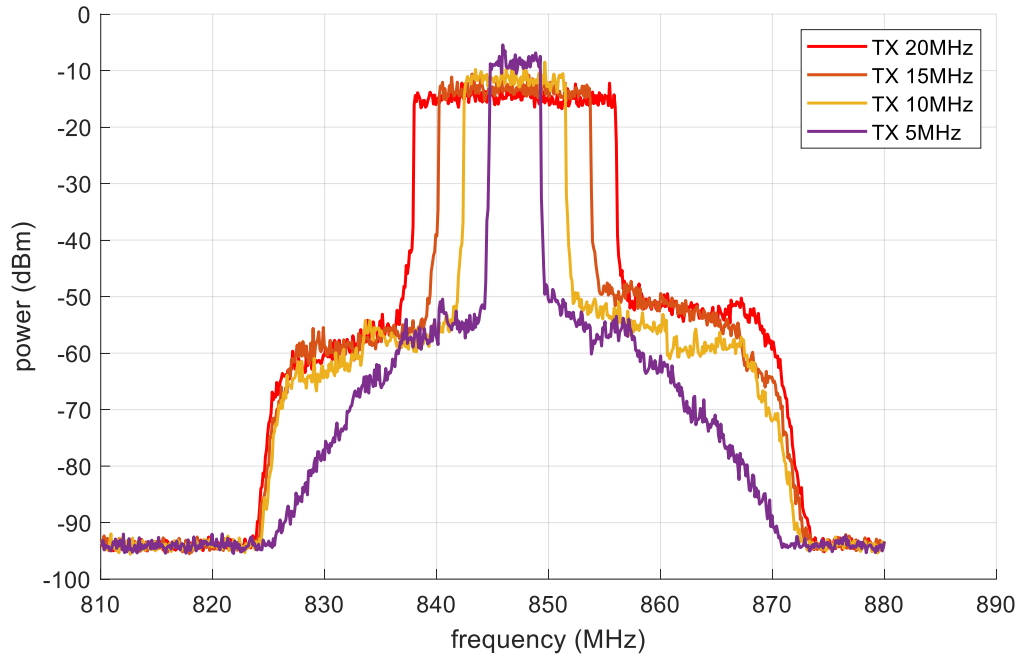


Figure 2. LTE band 20 TX spectrum, 23 dBm, various bandwidth settings.

conversion does not decrease the length of the data. However, the convolution calculations can use only a trimmed portion of the TX spectrum: because TX signals occupy only a certain bandwidth, all other spectra in the range of interest may be ignored (as shown in Figure 2; only several tens of MHz or an even smaller range of the measured spectrum is considered for the TX signal, and the rest is considered noise or spurious sideband; the effects of the spurious sideband are discussed in Section 3). Trimming in the frequency domain greatly avoids unnecessary calculations. Thus, solving equation (1) is computationally affordable after the conversion with equation (9) and trimming of the frequency components.

Although the trimmed frequency-domain convolution calculations are computationally affordable, further simplifications are applicable to derive the closed-form equations for the sideband spectrum.

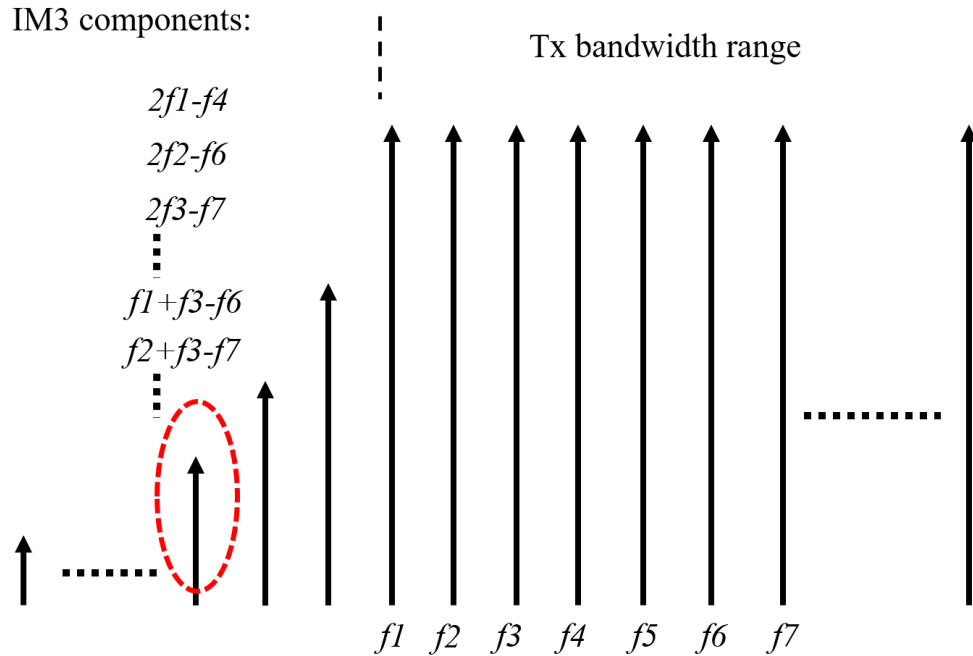


Figure 3. Demonstration of the IM products' sideband spectrum.

Equal power and random phase for all tones within the TX range (discussed in Section 3) can be reasonably assumed. Thus, the TX spectrum can be explicitly written as:

$$P_{\text{TX}}[k] = P_0 \cdot e^{j\varphi_k}, k = 1, 2, \dots, N, \varphi_k \sim U(0, 2\pi) \quad (10)$$

where  $k$  is the index of the sampled frequency points with 1 KHz spacing.  $N$  is the total number of tones, and the power level of each tone is  $P_0$  (e.g., 20 MHz TX bandwidth,  $N=20,001$ ,  $P_0 = -20$  dBm).  $\varphi_k$  is the random phase for each tone, satisfying a uniform distribution between 0 and  $2\pi$ . The intermodulation of the discrete TX tones generates the sideband frequency components that fall into 1 KHz grids. As illustrated in Figure 3, with multiple tones present within the TX bandwidth range, the IM3 products within the red circled frequency grid can be created from various combinations of tones. Because of the random phases of all TX tones, the IM3 products at the same frequency are summed

as complex numbers (considering the random phases rather than in phase). Similarly, for all frequency points in the sideband range, the power is the summation of all possible IM products (combinations) with random phases. Thus, the sideband spectrum calculations can be separated into two parts: 1) the number of IM products (created by different combinations of TX tones) falling within the same frequency and 2) the summation of the random phasors.

The IM product counts over the sampled frequencies are associated with the IM order and the total number of TX tones. The IM product counts satisfy the Irwin-Hall distribution [22] in the discrete form. The  $m^{\text{th}}$  order IM product count number at frequency index  $x$  to be  $H^{(m)}[x]$  is notated, and the sideband created by the  $m^{\text{th}}$  order IM products can be expressed as:

$$P_{\text{Imm, total}}[x] = E \left\{ \left| \sum_{k=1}^{k=H^{(m)}[x]} e^{j\varphi_k} \right| \right\} \cdot P_{\text{Imm}}, \varphi_k \sim U(0, 2\pi) \quad (11)$$

where  $P_{\text{Imm, total}}$  is the amplitude of the summation of all possible combinations of Imm products at a frequency point.  $P_{\text{Imm}}$  is the  $m^{\text{th}}$  IM power created by any pair of TX tones and can be found from the two-tone measurement (the TX tone power level and the generated IM product power follow the  $m$  dB/dB regrowth rate [20],[21]). In this way, the polynomial coefficient extraction described in equations (4),(5), and (6) may be omitted. A total of  $H^{(m)}[x]$  Imm products align at the frequency index  $x$ , and their phases are random. Therefore, the expected values of a summation of random phasors are also required to determine the solution for equation (11). When a total number  $N$  of units but random phasors  $e^{j\varphi_k}, k = 1, 2, \dots, N$  are present, the expected value of  $\left| \sum_{k=1}^{k=N} e^{j\varphi_k} \right|$  can be approximated as the given square root function with the curve fitting process in Matlab (with the power fit, and the power coefficient was found to be close to 0.5, and the

multiplication coefficient matches to the derivation when  $N=2$ ):

$$E\left\{\left|\sum_{k=1}^{k=N} e^{j\varphi_k}\right|\right\} \approx \frac{2\sqrt{2+2N}}{\pi}, N = 2,3,4 \dots \quad (12)$$

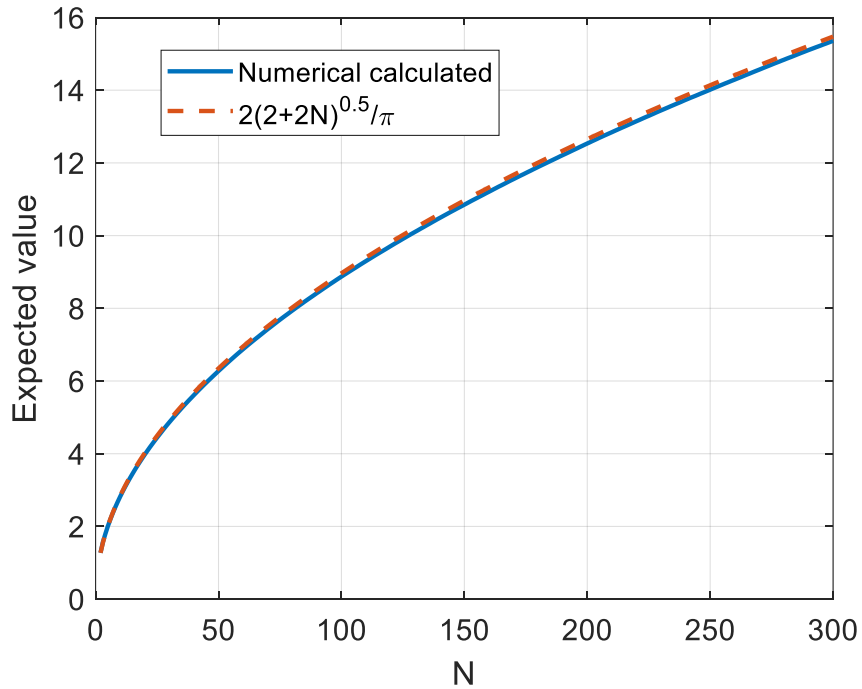


Figure 4. Approximation of the summation of random phasors.

This approximation has sufficient accuracy to determine the expected value of the magnitude of summation over random phasors and has been validated in MatLab through numerical calculations with a random function (Figure 4).

$H^{(m)}[x]$  can be derived as follows:

$$u[x] = \begin{cases} 1, & 1 \leq x \leq N \\ 0, & \text{otherwise} \end{cases} \quad (13)$$

$$H^{(m)}[x] = u[x] * u[x] * \dots * u[x] = u[x]^{*m} \quad (14)$$

$H^{(m)}$  satisfies the Irwin-Hall distribution but is expressed differently for different  $m^{\text{th}}$  orders. For instance, the third order is written as follows:

$$H^{(3)}[x] = \begin{cases} \frac{x(x+1)}{2}, & 1 \leq x \leq N - 1 \\ \dots, & N \leq x \leq 2N - 1 \\ \frac{[x-(3N-1)](x-3N)}{2}, & 2N \leq x \leq 3N - 2 \end{cases} \quad (15)$$

However, with higher orders, the Irwin-Hall distribution is closer to a Gaussian distribution. Thus, equation (14) can be approximated as:

$$H^{(m)}[x] \approx N^m \frac{1}{\sigma\sqrt{2\pi}} e^{-\frac{1}{2}\left(\frac{x-\mu}{\sigma}\right)^2}, H^{(m)}[x] \sim \mathcal{N}(\mu, \sigma^2), \quad (16)$$

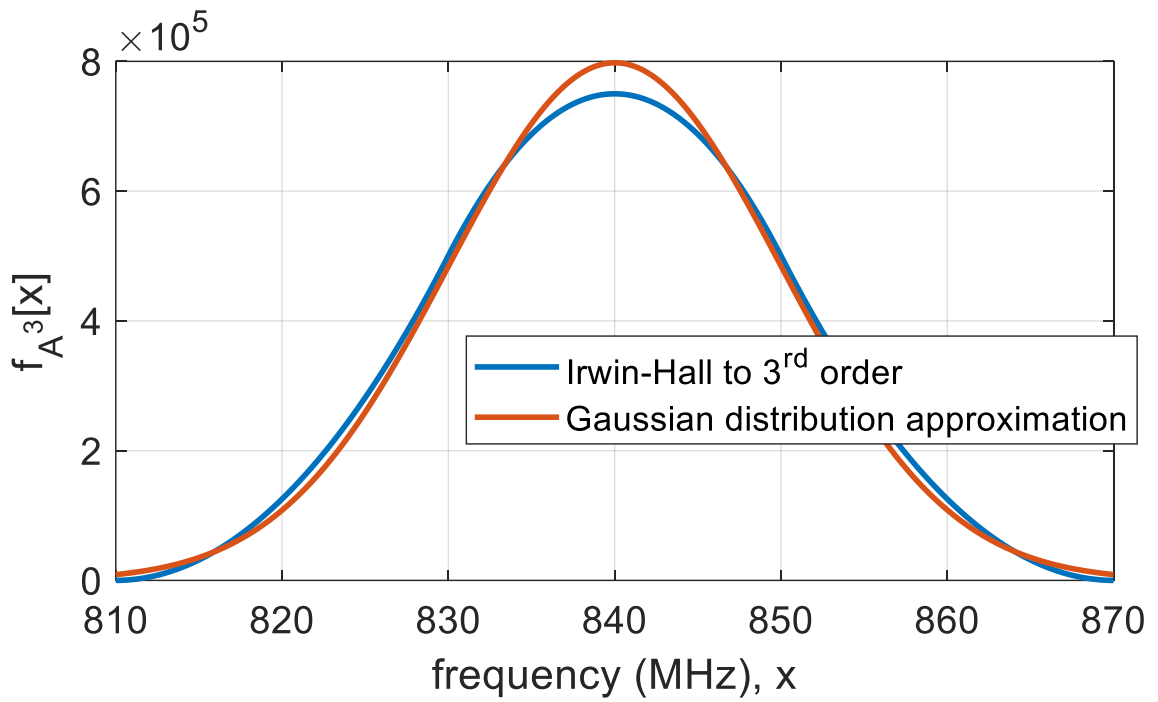
where  $\mu$  and  $\sigma$  are the mean and standard deviation of this Gaussian distribution, respectively. These values can be found as follows:

$$\mu = \frac{mN}{2}, \sigma = \sqrt{\frac{m}{12}} N \quad (17)$$

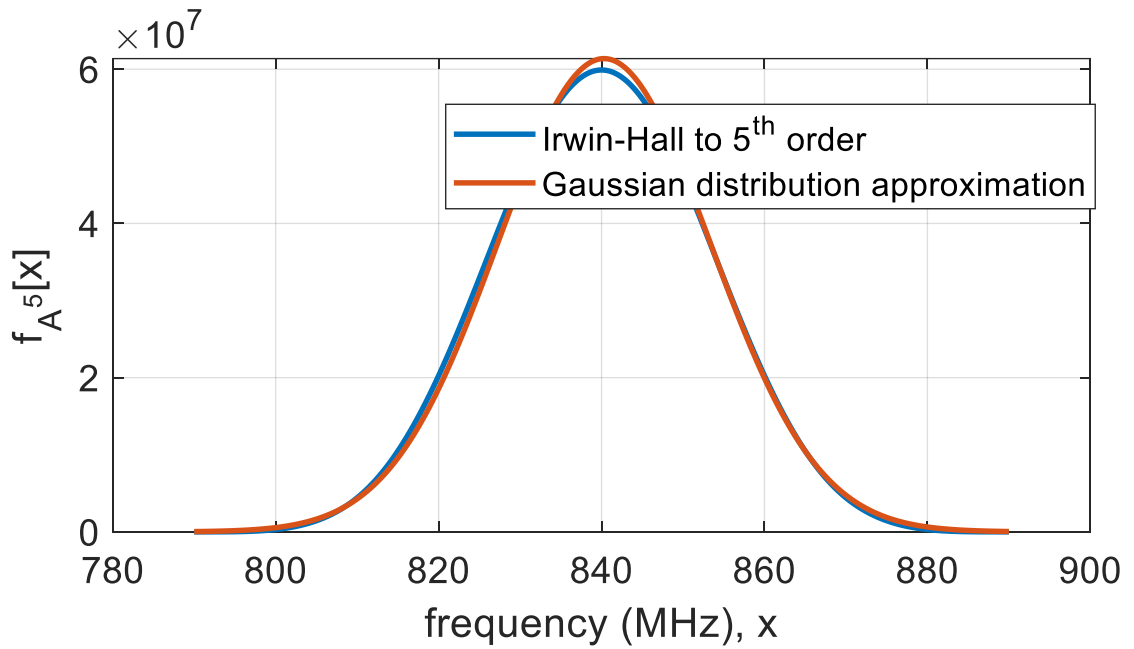
As shown in Figure 5, the Gaussian distribution (using the mean and standard deviation in equation (17)) can substitute for the Irwin-Hall distribution without sacrificing substantial accuracy, because the major discrepancies are within the TX range rather than the RX range (given that the IM products within the TX range are overwhelmed by the original high-power TX). Thus, the sideband spectrum can be expressed as:

$$P_{\text{Ipm, total}}[x] \approx P_{\text{IPm}} \frac{\sqrt{2N^m \frac{1}{\sqrt{\frac{m\pi}{6}} N} e^{-\frac{1}{2}\left(\frac{x-\frac{mN}{2}}{\sqrt{\frac{m}{12}} N}\right)^2}}}{\pi} \quad (18)$$

Several reasonable approximations may be involved but should have minor effects on the RX spectrum estimation expressed in closed-form expression.



(a)



(b)

Figure 5. Using a Gaussian distribution to approximate the Irwin-Hall distribution: (a) third order; (b) fifth order

### 3. MEASUREMENT VALIDATION

#### 3.1. REAL TX SPECTRUM

When a cellphone emulates LTE band 20 TX signals, the TX spectrum can be obtained from either a spectrum analyzer (magnitude only, Figure 2) or an oscilloscope (complex). With spectrum analyzer measurements, the TX tones fluctuate around a certain power level, and the summation equals 23 dBm. The small tones can be distinguished in the spectrum analyzer with a much smaller span and resolution bandwidth (RBW). The zoomed in spectrum has clear discrete tones with a 1 KHz gap (because the LTE subframe has a period of 1 ms), as shown in Figure 6. As discussed in Section 2, the broadband convolution calculations require complex numbers for the double-sided spectrum, because the phases of the tones affect the power level of the summation.

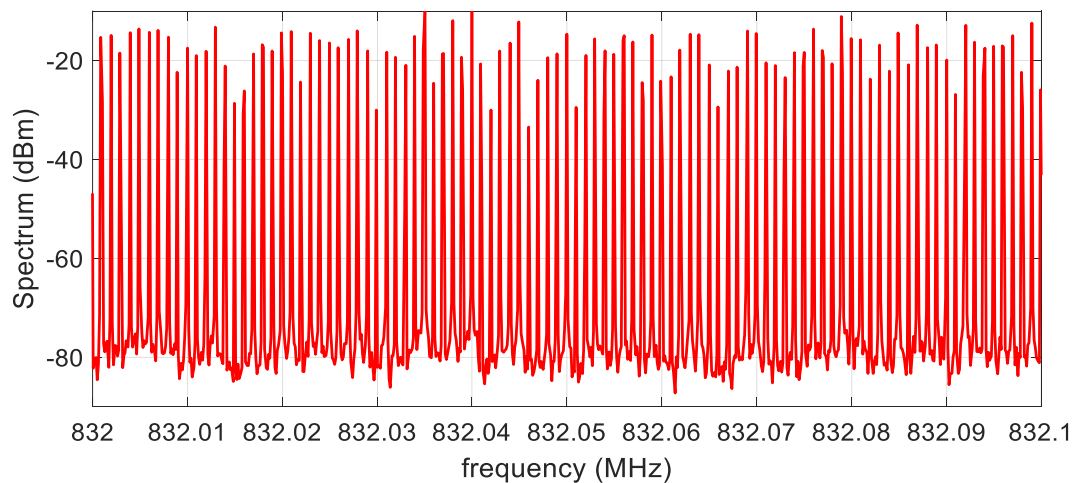


Figure 6. Measured TX spectrum (zoomed in, 100 KHz span) consisting of many tones with 1 KHz spacing.

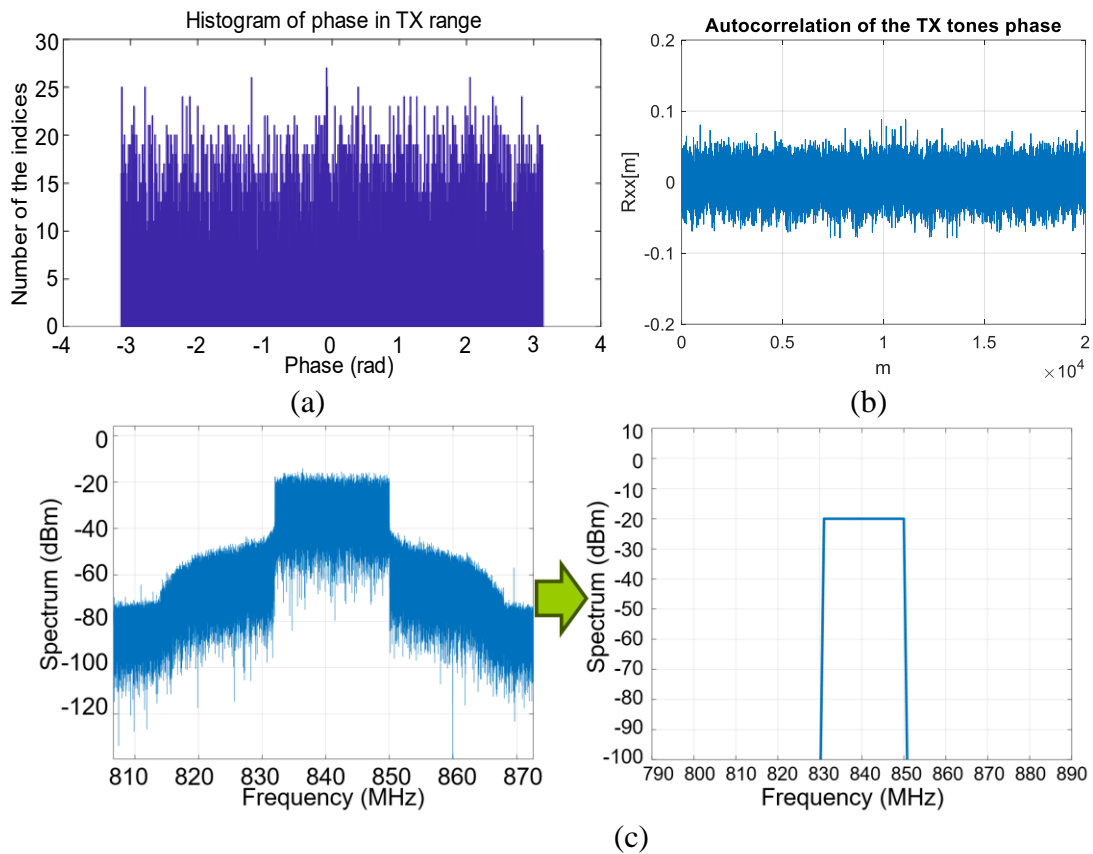


Figure 7. Investigation of modeling for mimicked TX: (a) histogram plot of the phases in the measured TX tones; (b) auto-correlation analysis of the phases; (c) illustration of the simplification of TX tone amplitude.

To investigate the phase information of the TX spectrum, we recorded cellphone emulator generated TX signals with an oscilloscope and a 2.5 ms period of TX sequence data with 2 Gsample/s (satisfying the requirements described in equation (8)). Both amplitude and phase were found after fast Fourier transformation of the recorded waveform (Figure 6 (b)). The phase terms of the discrete TX tones were plotted in a histogram (Figure 7 (a)), and the phases of the TX tones appeared to satisfy a random uniform distribution. Moreover, we calculated the autocorrelation [23] of the phase sequence of the TX tones with:

$$R_{xx}[m] = \sum_{n=1}^N \varphi[n] \cdot \overline{\varphi[n-m]} \quad (19)$$

where  $N$  is the total number of tones (here  $N=20,001$ ),  $\varphi[n]$  is the phase sequence of the tones, and  $\overline{\varphi[n-m]}$  is the circular shifted sequence of  $\varphi[n]$  by  $m$  points. The autocorrelation results were close to zero (Figure 7 (b)). Therefore, the phases could be reasonably assumed to be random with no periodic patterns. Regarding the amplitudes of the tones, although the actual measured TX spectrum showed fluctuations among the tones, and the sideband noise power therefore also fluctuated, summation over the RX channel frequency range smoothed out the fluctuations. Thus, the TX spectrum can be simplified as in equation (11), with approximations demonstrated in Figure 7 (c).

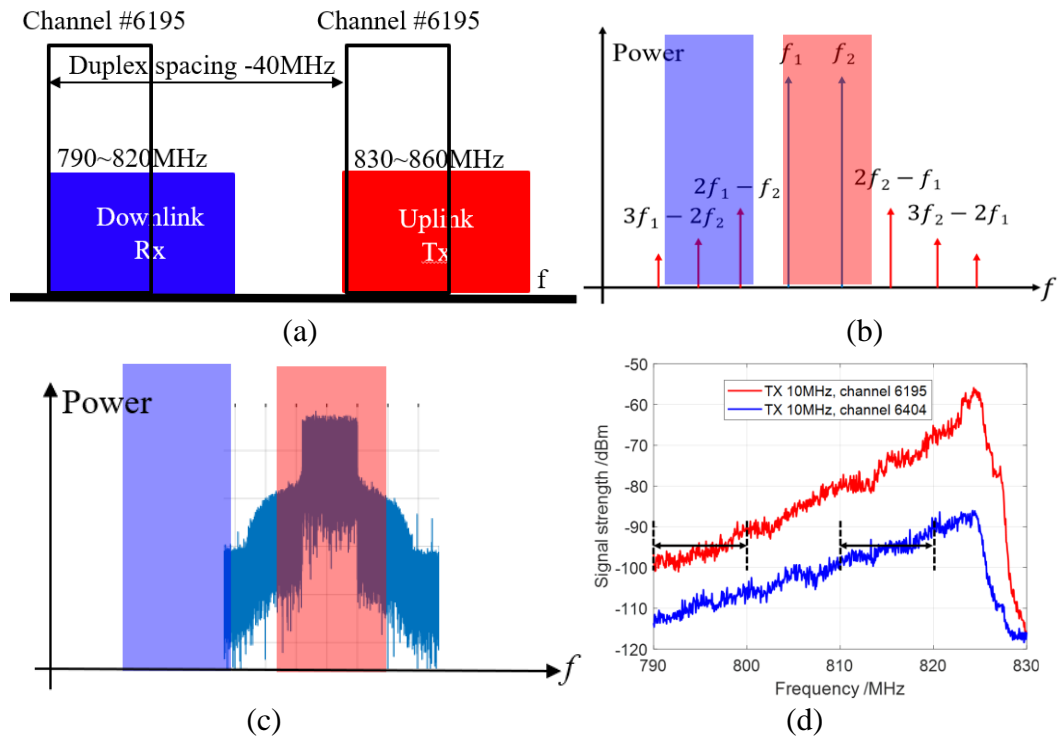


Figure 8. Investigation of the pre-distorted TX spectrum: (a) explanations of FDD channels and duplex spacing; (b) illustration of pre-distortion for two-tone signals; (c) illustration of pre-distortion for wideband TX signals; (d) measured RX spectrum for different channel settings.

Notably, because of the extra SMA and BNC adaptor connections, the spectrum leakage was probably exaggerated in this measurement (PIM caused by the adaptor connections). The effects of the TX spectrum pre-distortion therefore needed to be investigated for the broadband case. For the FDD LTE band 20 example shown in Figure 8 (a), the corresponding duplexer functioned as a bandpass filter in suppressing the spectrum outside the TX/RX range. For the two-tone case, the test system with the duplexer connection [14] filtered out the IM products caused by pre-distortion (Figure 8 (b)). However, this duplexer-based system could not completely remove the pre-distorted sideband (Figure 8 (c), because the TX band was wider than the TX channel bandwidth). However, by selecting different channels within the TX band, the perseveration of the sideband differed. When TX transmitted at the start channel (#6195), the duplexer truncated the lower-side sideband spectrum and eliminated the effects of pre-distortion on the RX channel power. In contrast, using the last channel (#6404) for TX transmission preserved the lower-side noise spectrum, thus affecting the RX channel. Fortunately, the results shown in Figure 8 (d) indicated that the pre-distortion of the TX spectrum had little influence on the RX channel power (also calculated with equation (10); difference of only  $<2$  dB). Therefore, the TX model expressed in equation (11) without considering the spurious sideband can be used to estimate the RX noise power without substantially sacrificing accuracy.

### 3.2. METALLIC CONTACT MEASUREMENT SYSTEM

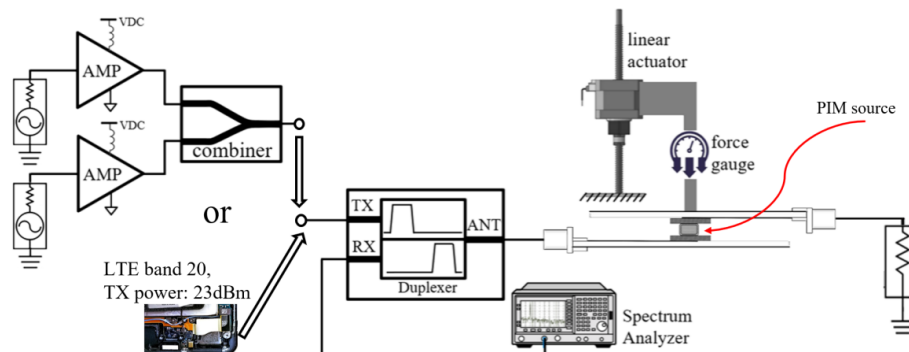


Figure 9. Measurement setup for validation of a metallic contact.

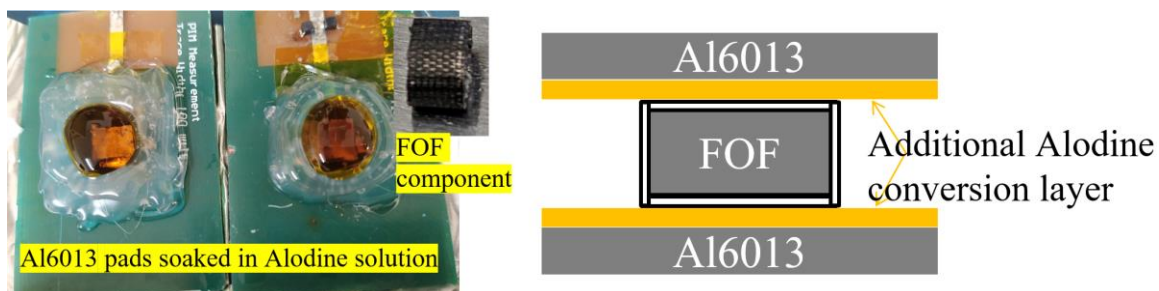


Figure 10. Test fixture comprising a flexible metallic component (Al pads on two micro-strip boards and conductive fabric over foam).

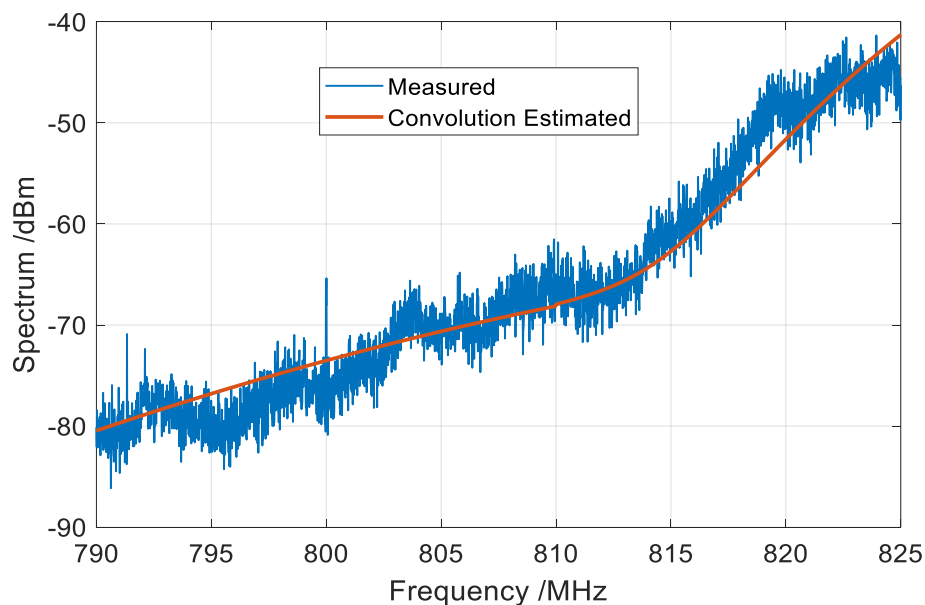


Figure 11. Correlation results of a conductive foam (0.24 N loading force case).

To validate the proposed model for correlating the two-tone and broadband (LTE band 20 herein) cases, the metallic contact component should satisfy two conditions: 1) the PIM level must be sufficiently high that both IM3 and IM5 in the two-tone test can be measured (above the noise floor), and 2) the contact must not be highly sensitive to external mechanical disturbance (because the “TX” port injection must be switched between two-tone and wideband, disturbance is inevitable during the measurement, as shown in Figure 9). However, these two conditions are usually contradictory, because the loosely connected conductive foam components often have high PIM but poor replicability and stability, whereas tightly connected conductive foam shows higher replicability and stability, but a low PIM level. Therefore, we intentionally created a “poor” foam contact by immersing the aluminum alloy pads in Alodine solution for several days (typically the immersion process for corrosion resistive purpose should take only minutes or even seconds), thus forming thick conversion layers with poor contact qualities (Figure 10). IM3 and IM5 were measured with two-tone injection. Then, under the same force loading condition, we carefully switched the TX injection to broadband from the cellphone emulator and measured the wideband RX spectra. Finally, we switched back to two-tone injection and determined whether IM3 and IM5 remained the same. This measurement was repeated for several different force loading conditions. Notably, a back-and-forth repeatability check is necessary. If the IM3 and IM5 results under the same force loading differ before and after the wideband TX injection, the measured results should be discarded, because the contact condition has already changed. The direct measured wideband spectrum was compared with the closed-form equation

calculated result shown in Figure 11. The calculation was found to capture the main trends in the spectrum change over frequencies.

We examined several additional cases under different force loading conditions for correlation validation (results summarized in Table I). The occupied TX frequency range was 830–850 MHz; with 40 MHz and 30 MHz duplex spacings, the RX ranges accounting for the received noise power were 790–810 MHz and 800–820 MHz, respectively.

### **3.3. TUNABLE NONLINEAR SOURCE SYSTEM**

In the experimental correlation validation with the conductive foam, acquisition of large amounts of data was hindered by the frequent TX source alternation and the poor stability (despite treatment with Alodine, the contact remained sensitive to disturbance, and the contact conditions were subject to change). Another limitation of the method is that the nonlinear system must be invariant (thus requiring the nonlinear behavior to be unchanged). This model may fail when the nonlinearity has substantial power dependency (e.g., does not follow a linear regrowth rate [20],[21]) or time variant behavior (for which determining when to capture the nonlinear characteristics is difficult). Therefore, to experimentally validate the calculations for different but more continuous nonlinearity levels, we created a tunable nonlinear source fixture. As shown in Figure 12 (a), the nonlinear source was on the signaling path of a microstrip trace. A multi-turn coil connected with a diode functioned as the nonlinear source. The near-field coupling between the microstrip trace and the nearby coil was controlled by the distance (position

Table 1 Correlation Results for Alodine-coated Conductive Foam

Force loading (N)	0.24	0.3	0.4	0.6
Two-tone results (IM3/IM5) [dBm]	-41.2/ -66.9	-51.6/ -80.6	-62.9/ -92.5	-66.4/ -89.3
Measured/estimated RX (duplex spacing 40 MHz, [dBm])	-62/ -64	-68.7/ -71	-69.5/ -72	-71.85/ -75.5
Measured/estimated RX (duplex spacing 30 MHz, [dBm])	-46.56/ -47	-51.31/ -52	-56.64/ -58.5	-61.18/ -59.5

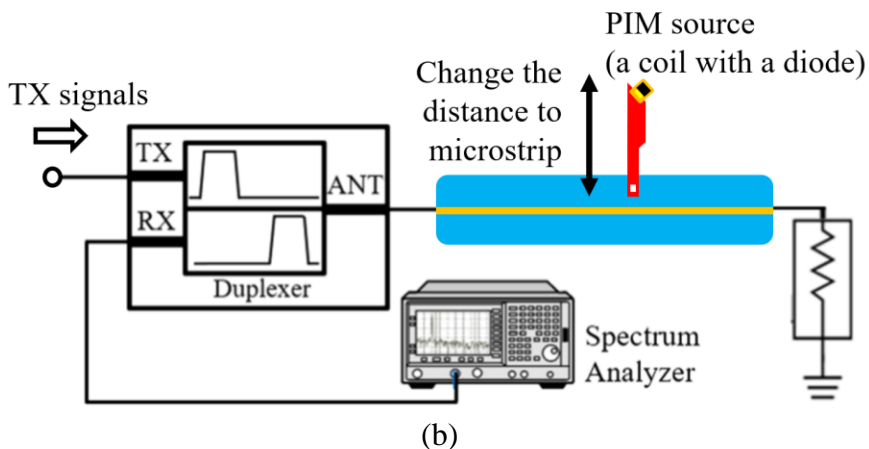
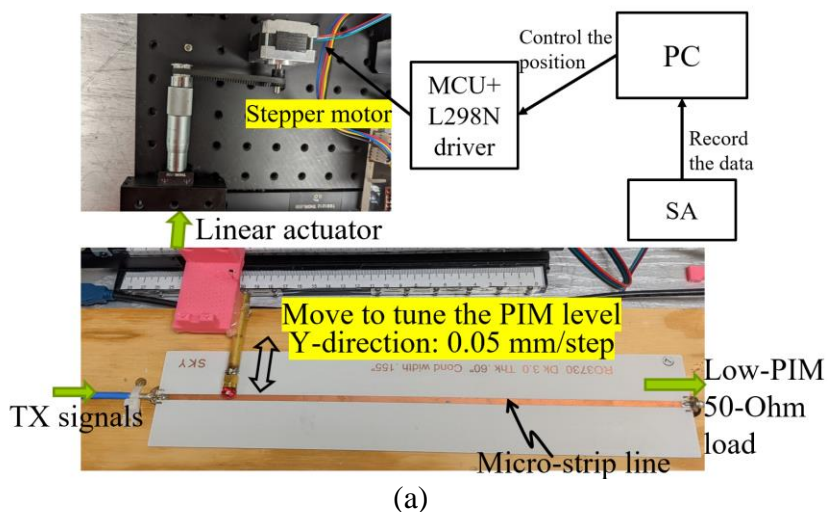
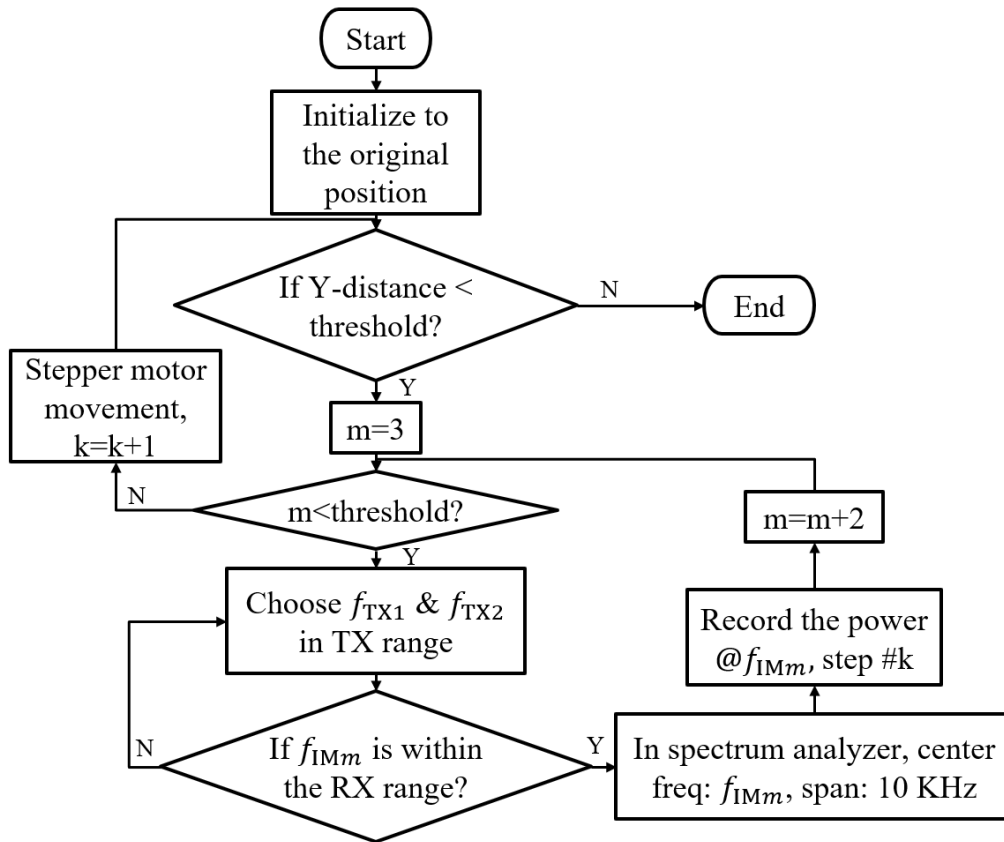


Figure 12. Measurement setup: (a) tunable nonlinear source fixture; (b) test system connection diagram.

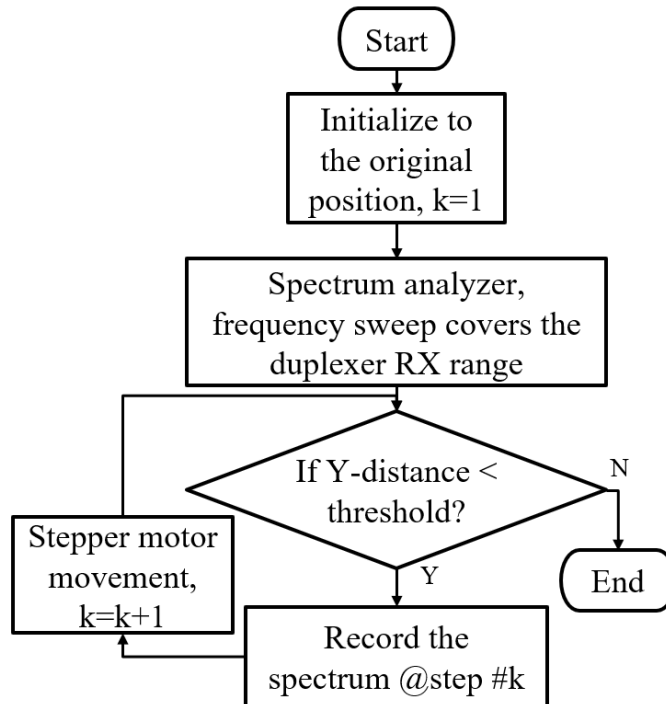
controlled by a linear actuator with a belt connected to a stepper motor). The TX signals first coupled from the trace to coil and showed nonlinear distortion at the diode. The distorted spectrum was coupled back from the coil to trace. The TX signals were either two-tone or from a wideband LTE emulator. The RX spectrum measured in the spectrum analyzer was recorded for every position. This tunable nonlinear fixture had the advantages of much better stability and repeatability than the metallic contacts discussed previously (as long as the position could be precisely replicated). The automation of the test flow is demonstrated in Figure 13 (a)(b). When two-tone was selected as the input, by changing the two-tone, the corresponding IM frequencies products occurred in the RX band and were captured by the spectrum analyzer over different positions (Figure 14 (a)). The sideband spectrum estimation was performed with equation (18) with the two-tone measured IM data in Figure 14 (a). Theoretically, any IM components with higher power than the noise floor can be measured, but the measured results might have larger errors for higher orders [18]. Higher orders might be caused by the high mixing orders when multiple PIM sources in the RF path or noticeable reflections are present. Therefore, measuring IM of higher orders is impractical.

After the two-tone test, we initialized the coil position and repeated the same movement, but changed the input as wideband signals. All recorded spectrum curves over different positions are shown in Figure 14 (b). The spectrum analyzer measured in Section 3.2, thus enabling repeatable measurements without frequent changing of the wideband in-channel RX power was calculated as follows [24]:

$$P_{\text{RX,channel}} \text{ (dBm)} = 10 \log_{10} \left( \frac{\sum_{k=1}^N P[k] \cdot (f[N] - f[1])}{\text{RBW} \cdot (N-1)} \right) \quad (20)$$



(a)



(b)

Figure 13. Automation of the test flow: (a) two-tone; (b) wideband.

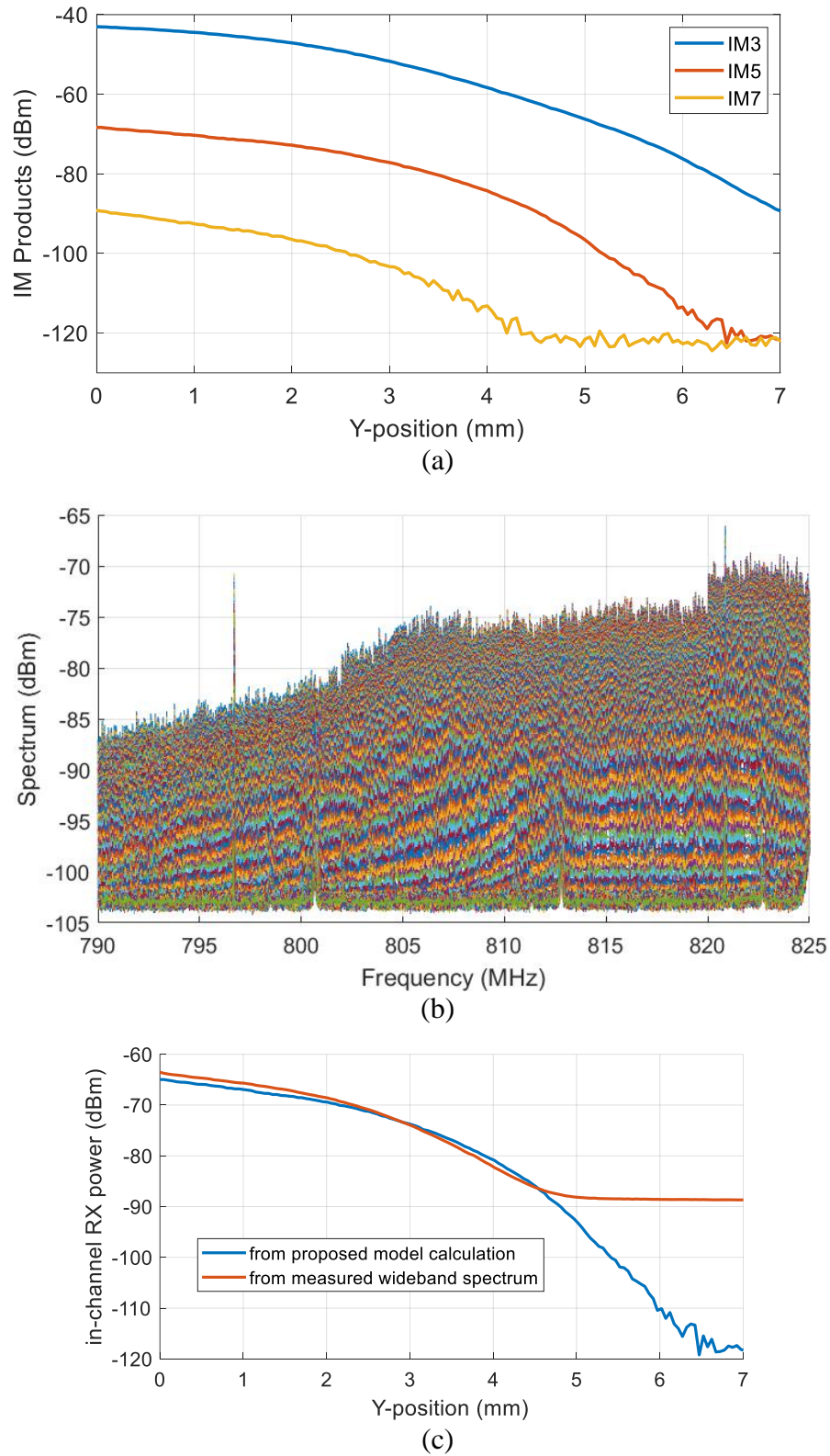


Figure 14. Measurement results and comparison: (a) two-tone measured IM products; (b) wideband spectrum of all positions; (c) RX channel noise power level comparison.

where  $f(1)$  and  $f(N)$  are the start frequency and stop frequency of the RX channel, respectively.  $N$  is the total number of points. RBW is the instrument resolution bandwidth setting (RBW must be considered here for the power calculation, because the span was 20 MHz, and the RBW exceeded 1 KHz).

Thus, the tunable nonlinear source fixture enabled the curve-to-curve comparison shown in Figure 14 I. The sideband noise spectrum power level correlation showed a 2 dB discrepancy except for the range reaching the spectrum measurement noise floor (>4.5 mm position). The sideband spectrum therefore was estimated well from the extracted characteristics from two-tone measurements.

#### 4. CONCLUSION

Herein, a mathematical link was established to correlate two-tone measurement results to the wideband spectrum. A nonlinear model was extracted from the two-tone measurement results. To calculate the nonlinear distortion of the wideband case with an affordable computational burden, we used trimmed frequency domain convolution to substitute the time-domain calculations. On the basis of several features of the actual TX spectrum, simplifications were applied to express the TX model explicitly. Thus, closed-form equations were derived for the RX spectrum estimations with the simplified TX model. The proposed sideband spectrum calculations were validated experimentally. Thus, we established a link enabling conversion of two-tone measurements for wideband spectrum estimation/prediction.

This work has several limitations: 1) negligible PIM source discontinuity in the RF path, 2) one dominant lumped PIM source, 3) negligible higher-mixing components, and 4) nonlinearity invariance (PIM behavior remaining unchanged). Nonetheless, a fundamental workflow and feasible numerical/analytical solutions are provided. More in-depth analysis or applications may be based on the outcomes/conclusions in this study.

## REFERENCES

- [1] C. Hwang and J. Fan, "Modeling and Mitigation of Radio Frequency Interference for Wireless Devices," *IEEE Electromagnetic Compatibility Magazine*, vol. 12, no. 1, pp. 87-92, 1<sup>st</sup> Quarter 2023, doi: 10.1109/MEMC.2023.10136454.
- [2] R. Holm, "Errata, 'The Electric Tunnel Effect across Thin Insulator Films in Contacts,'" *Journal of Applied Physics*, vol. 22, no. 9, p. 1217, 1951, doi: 10.1063/1.1700142.
- [3] C. D. Bond, C. S. Guenzer, and C. A. Carosella, "Intermodulation generation by electron tunneling through aluminum-oxide films," *Proceedings of the IEEE*, vol. 67, no. 12, pp. 1643-1652, Dec. 1979, doi: 10.1109/PROC.1979.11544.
- [4] C. Vicente and H. L. Hartnagel, "Passive-intermodulation analysis between rough rectangular waveguide flanges," *IEEE Transactions on Microwave Theory and Techniques*, vol. 53, no. 8, pp. 2515-2525, Aug. 2005, doi: 10.1109/TMTT.2005.852771.
- [5] J. G. Simmons, "Generalized Formula for the Electric Tunnel Effect between Similar Electrodes Separated by a Thin Insulating Film," *Journal of Applied Physics*, vol. 34, no. 6, pp. 1793-1803, June 1963, doi: 10.1063/1.1702682.
- [6] L. Kogut and K. Komvopoulos, "Analytical current-voltage relationships for electron tunneling across rough interfaces," *Journal of Applied Physics*, vol. 97, 073701-073701, 2005, doi: 10.1063/1.1866472.

- [7] J. R. Wilkerson, K. G. Gard, A. G. Schuchinsky, and M. B. Steer, "Electro-Thermal Theory of Intermodulation Distortion in Lossy Microwave Components," *IEEE Transactions on Microwave Theory and Techniques*, vol. 56, no. 12, pp. 2717-2725, Dec. 2008, doi: 10.1109/TMTT.2008.2007084.
- [8] J. R. Wilkerson, P. G. Lam, K. G. Gard, and M. B. Steer, "Distributed Passive Intermodulation Distortion on Transmission Lines," *IEEE Transactions on Microwave Theory and Techniques*, vol. 59, no. 5, pp. 1190-1205, May 2011, doi: 10.1109/TMTT.2011.2106138.
- [9] A. P. Shitvov, D. S. Kozlov, and A. G. Schuchinsky, "Nonlinear Characterization for Microstrip Circuits With Low Passive Intermodulation," *IEEE Transactions on Microwave Theory and Techniques*, vol. 66, no. 2, pp. 865-874, Feb. 2018, doi: 10.1109/TMTT.2017.2758726.
- [10] Q. Jin, J. Gao, G. T. Flowers, Y. Wu, G. Xie, and L. Bi, "Modeling of Passive Intermodulation in Connectors With Coating Material and Iron Content in Base Brass," *IEEE Transactions on Microwave Theory and Techniques*, vol. 67, no. 4, pp. 1346-1356, April 2019, doi: 10.1109/TMTT.2019.2893193.
- [11] Q. Jin and Q. Feng, "Frequency and Power Dependence of Passive Intermodulation in Connectors With Contact-Material Nonlinear Modeling," *IEEE Microwave and Wireless Components Letters*, vol. 31, no. 2, pp. 207-210, Feb. 2021, doi: 10.1109/LMWC.2020.3038861.
- [12] V. Golikov, S. Hienonen, and P. Vainikainen, "Passive intermodulation distortion measurements in mobile communication antennas," *IEEE 54<sup>th</sup> Vehicular Technology Conference. VTC Fall 2001. Proceedings (Cat. No.01CH37211)*, Atlantic City, NJ, USA, 2001, pp. 2623-2625 vol.4, doi: 10.1109/VTC.2001.957226.
- [13] S. Yang, W. Wu, S. Xu, Y. -J. Zhang, D. Stutts, and D. J. Pommerenke, "A Passive Intermodulation Source Identification Measurement System Using a Vibration Modulation Method," *IEEE Transactions on Electromagnetic Compatibility*, vol. 59, no. 6, pp. 1677-1684, Dec. 2017, doi: 10.1109/TEMC.2017.2705114.
- [14] S. Xia et al., "Practical Fixture Design for Passive Intermodulation Tests for Flexible Metallic Contacts," *2022 IEEE International Symposium on Electromagnetic Compatibility & Signal/Power Integrity (EMCSI)*, Spokane, WA, USA, 2022, pp. 17-22, doi: 10.1109/EMCSI39492.2022.9889578.

- [15] S. Xia et al., “Passive Intermodulation Under Different Spring Contact Conditions,” 2022 IEEE International Symposium on Electromagnetic Compatibility & Signal/Power Integrity (EMCSI), Spokane, WA, USA, 2022, pp. 12-16, doi: 10.1109/EMCSI39492.2022.9889661.
- [16] “TS 136 104 – V8.3.0 – LTE,” IEEE Standard for LTE, 3<sup>rd</sup> Generation Partnership Project (3GPP), 2018.
- [17] N. L. Johnson, S. Kotz, and N. Balakrishnan, Continuous Univariate Distributions, Volume 2, 2<sup>nd</sup> Edition, Wiley, 1995, ISBN 0-471-58494-0 (Section 26.9).
- [18] J. A. Gubner, Probability and Random Processes for Electrical and Computer Engineers, Cambridge University Press, 2006, ISBN 978-0-521-86470-1.
- [19] Agilent Technologies, “Agilent Spectrum and Signal Analyzer Measurements and Noise,” Retrieved July 25, 2013, from <http://literature.agilent.com/litweb/pdf/5966-4008E.pdf>.

#### IV. A SEGMENTATION APPROACH FOR PREDICTING PLANE WAVE COUPLING TO PCB STRUCTURES

##### ABSTRACT

Evaluating the far-field radio frequency (RF) susceptibility of electronic devices often depends on extensive testing or full wave simulations. These methods are effective when complete system information is available but require too much time and too many resources to evaluate a large number of variations in system configurations, where trace routings, IC package styles, trace terminations, arrival angle and polarization of incoming wave, etc., are varied from one configuration to another. The goal of the following paper is to develop simulation techniques for studying the statistical characteristics of coupling to typical printed circuit board (PCB) structures. Simulation time can be reduced by breaking the structure into small segments, determining the coupling and transmission characteristics of each segment analytically or in a full-wave model, and then determining the coupling to the overall structure by assembling the individual segments in a circuit simulation. Re-using pre-modeled segments of commonly occurring structures (e.g. IC package, trace, etc.) allows making estimates with minimal computational effort even for a complicated PCB design. Simulation time is estimated to improve by a factor of 40 or more over traditional full-wave modeling using this approach. This methodology enables the analysis of statistical electromagnetic coupling to random PCB geometries.

**Keywords:** electromagnetic coupling, PCB, plane wave illumination, reciprocity, segmentation, statistical analysis, susceptibility.

## 1. INTRODUCTION

Complicated electronic devices usually contain PCBs for main controllers or various modules. External electromagnetic waves can interrupt the normal functions of the devices if there is sufficient energy coupled to the PCB. When considering the electromagnetic coupling to the PCBs, the incoming wave angle of arrival, PCB size, trace length, trace orientation angle etc. are uncertain. To better understand the immunity of PCBs to electromagnetic energy which couples to traces, it is worthwhile to look at the statistical results for the susceptibility study rather than looking into several specific cases. With statistical data to help understand the dominant electromagnetic coupling structure type(s) on the PCBs, the improvement of RF immunity can be achieved more easily. Electromagnetic coupling to PCBs has been studied for decades. The simplest scenario is a plane wave coupling to a microstrip trace. Detailed analytical derivations are given in [1], [2] for coupling to a single microstrip line from an external wave. There are some studies to modify and apply the analytical solutions to more variations [3], [4]. These studies, however, are still limited to simplified structures and are difficult to apply to many realistic applications, especially as modern electronic devices become more and more complicated. As a result, the analysis of coupling to electronic devices relies heavily on full-wave simulations. Although computational electromagnetic modeling tools can handle very complicated geometries, the calculation time will be substantial when modeling multiple boards. A full-wave simulation for a single angle of incidence could take hours, making analysis of multiple geometries and incident angles virtually

impossible. A faster method is essential for statistical studies of electromagnetic coupling to PCBs.

The electromagnetic coupling to a structure from an external plane wave can be estimated for multiple angles of incidence in just one simulation using the reciprocity theorem [5], which greatly reduces the total analysis time. Transmission line structures like PCB traces above a return plane can be broken into several straight segments and then simulated in a circuit simulator [6]. A statistical analysis can be used to quantify how coupling changes with variations in geometry [7]. It is not possible, however, to use transmission line equations to find the coupling that results from discontinuities or transitions in the transmission lines, and which are responsible for a significant portion of the non-TEM fields. Accounting for coupling to the packages of integrated circuits (ICs) also does not fit the standard transmission line approach. The study in [8] showed how electromagnetic coupling to circuit structures can be represented using extended S-parameters. As discussed in [9], while the trace is part of the electronic device, one ultimately wants to find the voltage induced by the electromagnetic wave at the IC pins. The authors of [10] explain how to use extended S-parameters to predict radiated emissions by segmenting the whole structure into several parts. These concepts are combined in our study in the sense that complicated PCB structures are broken into pieces, or segments, the electromagnetic properties of each segment are characterized in full-wave simulation to form a library of PCB parts, and then coupling to complicated PCB IC/trace structures can be estimated by assembling the extended S-parameters for these segments together in SPICE or a similar tool. Since commonly occurring structures on the PCBs, such as straight trace segments, trace bends, IC packages, etc., can be

reused in multiple simulations, coupling can be found for many complex structures made from these segments very quickly, requiring much less time than a full-wave simulation of the entire structure.

The following paper extends paper [11] which proposes a segmentation and cascading method based on far-field reciprocity to study RF coupling to PCBs. The method utilizes the generalized S-parameter model to represent the electromagnetic properties of a structure under external electromagnetic wave illumination. Thus, the electromagnetic coupling problem is converted to a circuit problem. The previous paper [11] already introduced the segmentation approach and demonstrated the electromagnetic coupling prediction accuracy for both individual incident angles and the average of the angles of arrivals sampled on a sphere. As the extension part, this paper will discuss in more detail the implementation of the segmentation and cascading approach. Proper handlings are needed to correctly “align” and cascade the segments. The detailed pre-modeling phase procedures for different structures will also be covered. Some accuracy is sacrificed to achieve faster electromagnetic coupling analysis because of implicit assumptions associated with the approach. However, a distinguished advantage of the segmentation method is that the pre-characterized segments can be assembled like building blocks to represent a complicated PCB geometry with minimal computational efforts. With this accelerated segmentation method for electromagnetic coupling analysis, a large number of geometries can be analyzed when considering a variety of PCBs with many random variables.

## 2. SEGMENTATION APPROACH

To solve the problem of rapidly determining coupling to a variety of PCB configurations, a segmentation method is used by connecting a handful of pre-characterized typical structures. Each structure is characterized in advance and stored as a “component” segment. The segment blocks can be reused and connected to retrieve the electromagnetic characteristics of a complex geometry. This segmentation approach utilizes far-field reciprocity to use the extended S-parameters to represent coupling to individual PCB components or segments. Transformations of the S-parameters are needed, however, to align the segments in the desired locations.

### 2.1. CASCADABLE SEGMENTS FOR FAST COUPLING ANALYSIS

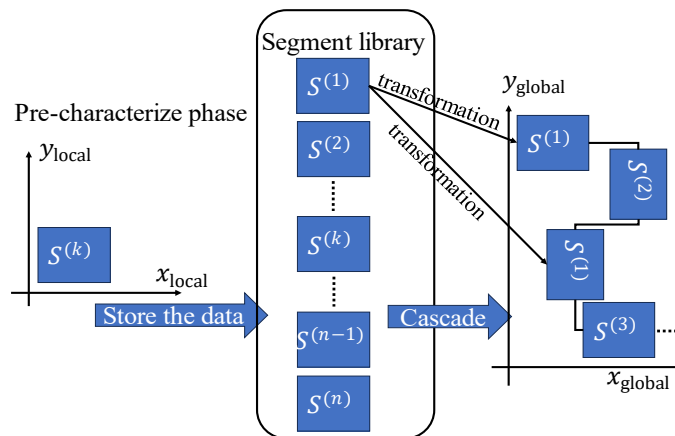


Figure 1. Segmentation concept illustration.

To accelerate the computational speed for studying the electromagnetic susceptibility of a variety of devices under test (DUTs), some typical/commonly

occurring structures can be characterized in advance, so it only requires a minimum effort to assemble the parts when simulating each geometry. As shown in Figure 1, the electromagnetic properties of a segment are found at the pre-characterization phase and then stored in the segment library. For the susceptibility study of the DUT, the pre-characterized segments are picked and placed in the global coordinate system following a correct order to retrieve the electromagnetic coupling characteristics of the entire DUT. As the illustrated example shows, one segment can be re-used without going through the characterization stage again. This is the key point of saving computational efforts and accelerating the electromagnetic coupling analysis. Since the stored data of a segment are obtained when the segment is placed in a local coordinate system, to correctly place and “align” the segments in the global system, some transformations are needed.

## 2.2. FAR-FIELD RECIPROCITY

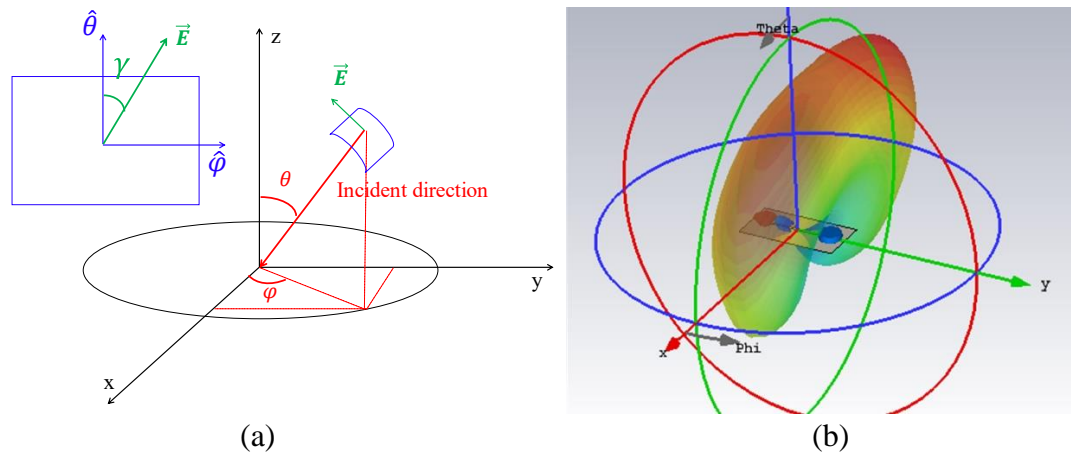


Figure 2. PCB under electromagnetic wave illumination: (a). Incident angle of arrival and polarizations for the incoming plane wave (b). Radiation pattern of a PCB.

The electromagnetic coupling characteristics of the DUT that is subject to incoming plane waves with angles of arrival  $\theta, \phi$  and the polarization angle  $\gamma$  (see the

angle definition in Figure 2 (a)) can be obtained directly in the full wave simulation. Fully characterizing the DUT susceptibility for different angles of arrival and polarization, however, requires a prohibitively large number of direct illumination (full-wave) simulations to be performed. Far-field reciprocity can be utilized to substantially reduce the amount of simulation time. Using this technique, the coupling characteristics of a device/structure from many polarizations and angles of arrival can be found with only one far-field simulation providing the radiation pattern of the device (see Figure 2 (b)). The coupled voltage across the victim port is given by [11], [12]:

$$V(\theta, \varphi, \gamma) = \frac{\lambda R}{\eta} \sqrt{\frac{Z_0}{2P_{in}}} \left( \cos\gamma \cdot E_{inc} \cdot E_{\theta rad}(\theta, \varphi) + \sin\gamma \cdot E_{inc} \cdot E_{\varphi rad}(\theta, \varphi) \right). \quad (1)$$

where  $E_{inc}$  is the incident E-field of the external plane wave with the polarization angle of  $\gamma$ ,  $P_{in}$  is the excitation power at the input port (used to calculate the radiation pattern),  $R$  is the radius of the spherical observation surface,  $\mathbf{E}_{rad} = (E_{\theta rad}, E_{\varphi rad})$  is the radiated E-field on the observation sphere when the victim port is excited, and  $\eta$  is the impedance of free space. Both incident and radiated fields are decomposed into orthogonal  $\theta$  and  $\varphi$  components.  $Z_0$  is the load impedance at the port,  $\lambda$  is the wavelength of the incoming wave.

### 2.3. GENERALIZED S-PARAMETERS BASED ON FAR-FIELD RECIPROCIDY

Consider a two-port structure illuminated by a plane wave as shown in Figure 3. The S-parameters between the ports defined at the two ends are obvious and typical. In addition to these ports, however, a third port can be defined to represent the external electromagnetic wave coupling to the structure [8]. An expanded 3-port S-parameter

representation characterizes both the original two-port structure as well as its coupling to/from an external plane wave. The coupling characteristics can be expressed as:

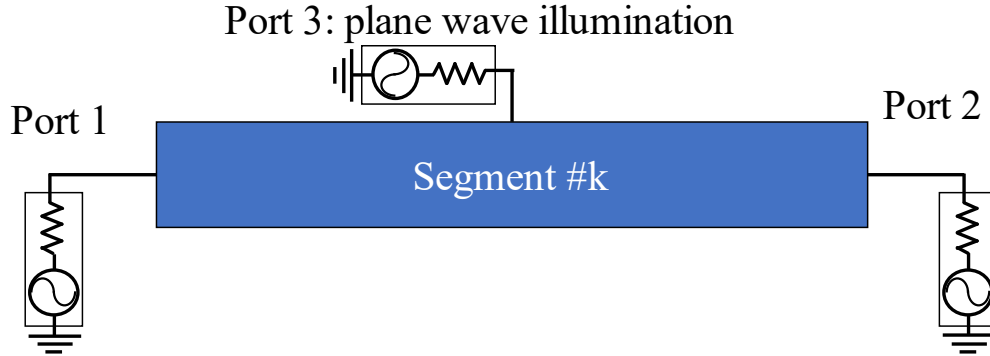


Figure 3. Generalized S-parameter model to represent a segment under plane wave illumination.

$$S_{13}(\theta, \varphi, \gamma) = \frac{V_1^-}{E_{\text{inc}}} = \frac{\lambda R}{\eta} \sqrt{\frac{Z_0}{2P_{\text{in}}}} (E_{\theta\text{rad},1}(\theta, \varphi) \cdot \cos\gamma + E_{\varphi\text{rad},1}(\theta, \varphi) \cdot \sin\gamma). \quad (2)$$

where  $V_1^-$  is the amplitude of the outgoing wave at port 1 normalized to the impedance  $Z_0$  (in this case the reflected wave  $V_1^+ = 0$  and  $V_1^- = V_1$ ),  $\theta, \varphi, \gamma, P_{\text{in}}, R, Z_0, \eta, \lambda$  have the same definitions as in (1),  $E_{\theta\text{rad},1}(\theta, \varphi)$  and  $E_{\varphi\text{rad},1}(\theta, \varphi)$  are the radiated E-field (orthogonal components) at an angle  $(\theta, \varphi)$  at a distance  $R$  when the source is placed at port 1. The parameter  $S_{23}$  can be found with a similar expression except that the radiated E-fields are calculated with the stimulus at port 2. The full 3-port S-parameter matrix structure is explained in [8], [11].

The extended S-parameters can be determined from an analytic representation of the radiation from a structure (in particular this is possible for a microstrip line, monopole and loop antennas, etc.), or by performing a full wave simulation. Once the 3 port S-parameters are known, the analysis can be performed in a circuit simulator. The two ends

of the trace can be connected to any other components (e.g. terminations or other 3-port S-parameter blocks) to analyze a variety of PCB configurations.

## 2.4. ROTATION, TRANSLATION, AND CASCADING OF SEGMENTS

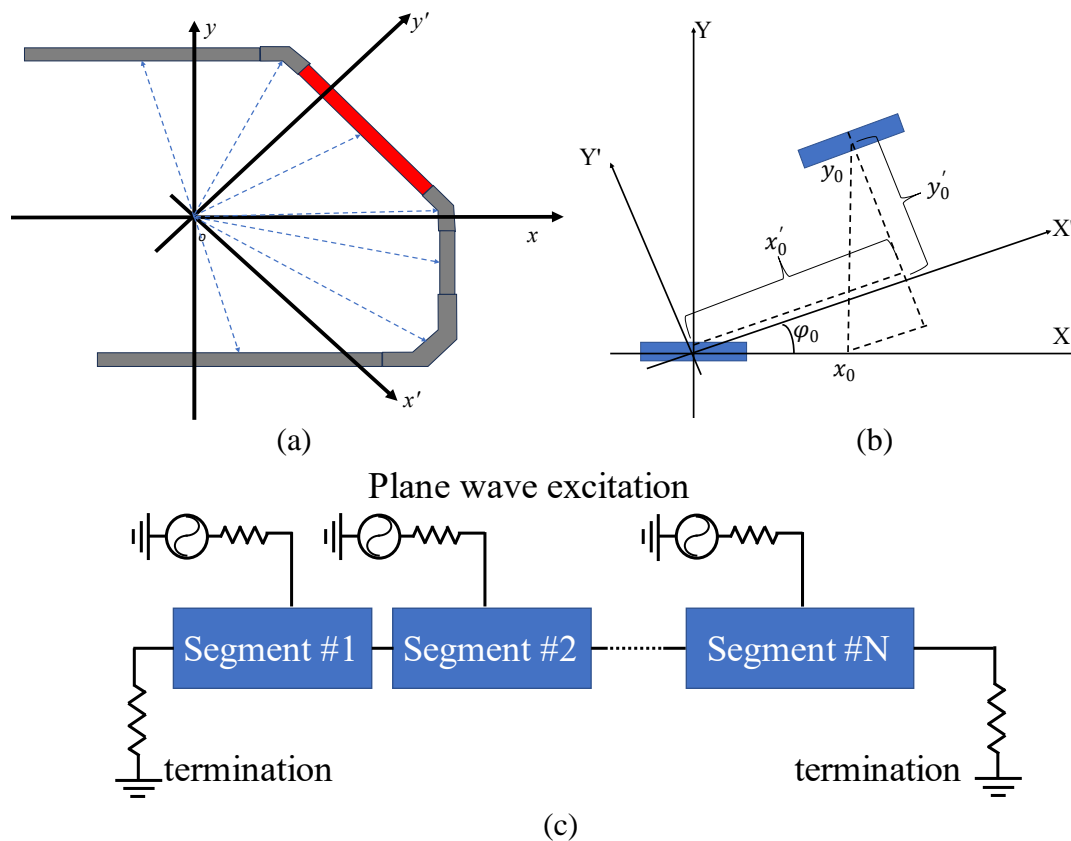


Figure 4. (a) a trace routing example composed by 7 segments; (b) translation and rotation to a segment (top view); (c) equivalent circuit representation.

The segmentation approach can substantially speed up simulation reducing it to circuit consisting of the pre-determined generalized S-parameter blocks of each segment of a complex PCB layout connected in the correct order. For example, the trace shown in Figure 4 (a) can be decomposed into 4 straight traces and 3 trace bends. All 7 segments can be modeled as 3-port S-parameter blocks as discussed in Section 2. Each segment is

characterized at the origin of the coordinate system as shown in Figure 1. To assemble the trace geometry from the segments, each segment has to be rotated and translated into their position within the trace geometry. The translation and rotation operations are shown in Figure 4 (b). Once translated and rotated, the analysis of the electromagnetic coupling is as simple as cascading the S-parameter blocks and conducting a circuit simulation as shown in Figure 4 (c).

Rotation and translation require modification of the segment S-parameters. Since the PCB plane is not rotated, rotation of the segment only changes the azimuthal angle  $\varphi$ . This operation is given mathematically as:

$$S_{13,\text{rot}}(\theta, \varphi, \gamma) = S_{13}(\theta, \varphi - \varphi_0, \gamma), \quad S_{13}(\theta, \varphi + 2\pi n, \gamma) = S_{13}(\theta, \varphi, \gamma),$$

$$n = \pm 1, \pm 2, \dots, \infty \quad (3)$$

where  $S_{13,\text{rot}}$  is the transformed S-parameters after the rotation in the azimuthal direction by the angle  $\varphi_0$ . The equation for the component  $S_{23}$  is identical.

Translation of the S-parameters is more complicated. We assume that the translation happens only in the  $xy$  plane because of the planar structures of the PCB. As shown in Figure 5, the translation from point  $A$  to point  $B$  results in a phase shift of the incoming plane wave which can be calculated from the projection of the translation vector onto the PCB in the illumination direction. The projection distance  $L$  can be calculated as a scalar product of two vectors:

$$L(\theta, \varphi, x_0, y_0) = \overline{U(\theta, \varphi)} \cdot \overline{V(x_0, y_0)} \quad (4)$$

where

$$\overline{U(\theta, \varphi)} = (\sin \theta \cos \varphi, \sin \theta \sin \varphi, \cos \theta) \quad (5)$$

is the unit vector in the direction of illumination,  $\theta$  and  $\varphi$  are the elevation and azimuth

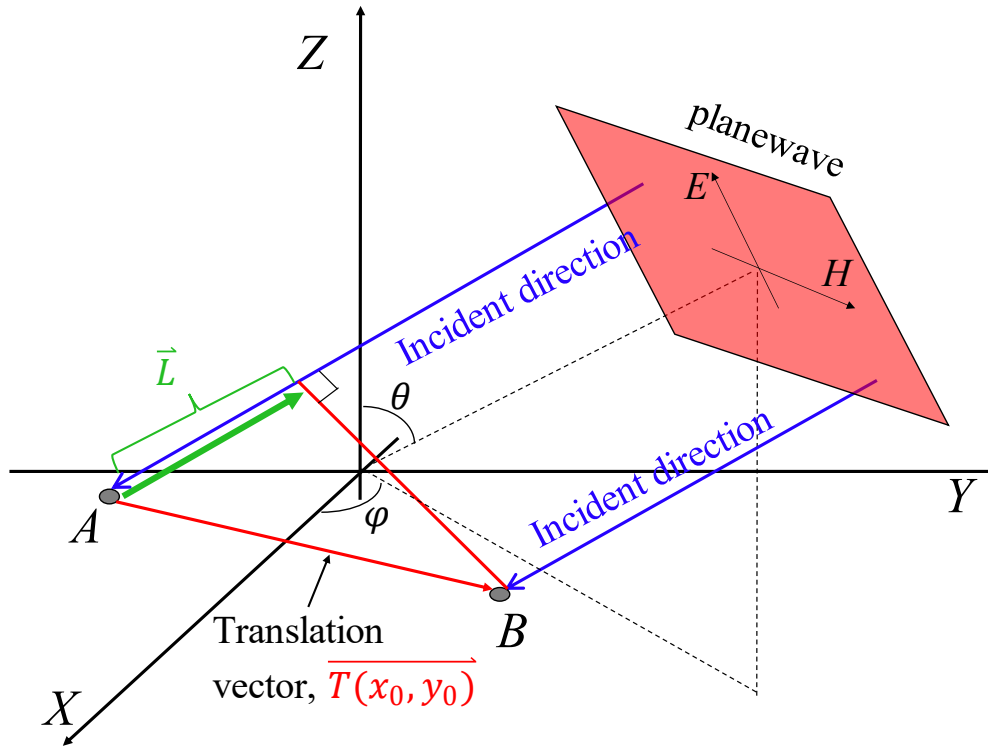


Figure 5. Extra time delay due to the translation (on the 2D plane) of the segment.

angles, respectively, and

$$\overrightarrow{T(x_0, y_0)} = (x_0, y_0, 0) \quad (6)$$

is the translation vector to the coordinates  $x_0, y_0$ . The corresponding phase shift is

$$\Delta\varphi(\theta, \varphi, x_0, y_0) = \frac{2\pi f}{c} L(\theta, \varphi, x_0, y_0), \quad (7)$$

where  $f$  is the frequency, and  $c$  is the speed of light. The modified coupling term therefore is

$$S_{13\_tran}(\theta, \varphi, x_0, y_0, f) = S_{13}(\theta, \varphi, f) \cdot e^{j\Delta\varphi}. \quad (8)$$

Combining (4) and (9), the complete transformation is given by:

$$S_{13\_rot\&tran}(\theta, \varphi, x_0, y_0, f) = S_{13}(\theta, \varphi - \varphi_0, f) \cdot e^{j\Delta\varphi(\theta, \varphi - \varphi_0, x_0, y_0)} \quad (9)$$

Using the modified 3-port S-parameters after translation and rotation of each segment, the original electromagnetic coupling problem can be reduced to solving an equivalent circuit as shown in Figure 4 I.

### 3. PRE-CHARACTERIZATION OF SEGMENTS

Although the mathematical definition of the extended S-parameters given in the previous section is straightforward, practical implementation of the segment characterization leads to certain challenges, which will be discussed below.

#### 3.1. MODELING OF SEGMENTS USING FULL-WAVE SIMULATIONS

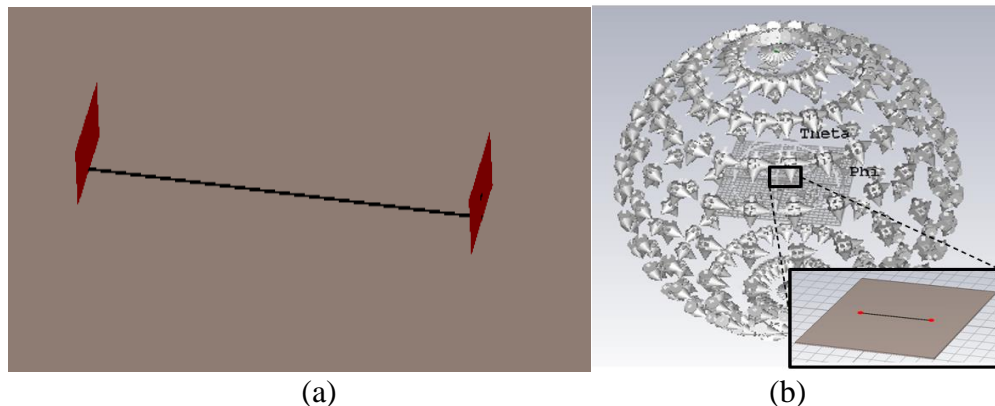


Figure 6. Modeling of a microstrip trace segment to obtain generalized S-parameters: (a) stimulation of both ends of the segment; (b) far-field electric-field probes over a sphere.

The generalized S-parameters for a segment can be found from the two-port S-parameters and radiation patterns produced by driving each port, as discussed in Section 2. For demonstration purpose, the microstrip structure in Figure 6 (a) is used as an example. The excitation ports were set at the two ends of the trace, and far-field

electric-field probes (for both the  $\theta$  and  $\varphi$  components of the radiated field) were placed on a sphere around the PCB at 15-degree increments (total 650 probes, shown in Figure 6 (b)). Excitation of each port produces  $\theta$  and  $\varphi$  far-field components at each probe location (i.e. 4 responses total for each location). Equation (2) is then used to calculate the generalized S-parameter matrix for each probe location (corresponding to an incoming plane wave). A similar workflow can be applied to other segments, such as IC packages, via transition, etc. [11]. It is worth mentioning that waveguide ports were chosen over lumped ports because waveguide ports have minimal reflections. However, lumped ports have to be used in some scenarios due to geometry limitation. These reflections caused by the excessive inductance of the lumped ports in the full-wave characterizations can cause errors and may accumulate over many segments. Therefore, accuracy loss can be reduced by minimizing the number of segments using lumped-port stimulated full-wave simulations when possible.

### 3.2. ANALYTICAL MODELING OF THE STRAIGHT TRACES

As an alternative to using a full-wave simulation, straight microstrip lines can be characterized using closed-form equations. As the straight trace above a ground plane is a typical structure and its electromagnetic coupling characteristics are well studied [1], [13], the coupled voltages across the two ends on a finite-length straight trace (along the x-direction) due to the external incoming plane wave can be expressed using Baum-Liu-Tesche (BLT) equations [13]:

$$\begin{bmatrix} V_1 \\ V_2 \end{bmatrix} = \begin{bmatrix} 1 + \rho_1 & 0 \\ 0 & 1 + \rho_2 \end{bmatrix} \begin{bmatrix} -\rho_1 & e^{j\beta l} \\ e^{j\beta l} & -\rho_2 \end{bmatrix}^{-1} \begin{bmatrix} S_1 \\ S_2 \end{bmatrix} \quad (10)$$

then by expansion, the expression can be changed to:

$$\begin{bmatrix} S_1 \\ S_2 \end{bmatrix} = \begin{bmatrix} \frac{1}{2} \int_0^l e^{j\beta x} [V'_{s1}(x) + Z_c I'_{s1}(x)] dx \\ -\frac{1}{2} \int_0^l e^{j\beta(l-x)} [V'_{s1}(x) - Z_c I'_{s1}(x)] dx \end{bmatrix} \quad (11)$$

$$\begin{bmatrix} V'_{s1} \\ I'_{s1} \end{bmatrix} = \begin{bmatrix} -j\omega\mu_0 \int_0^d H^{\text{inc}}_y(x, z) dz \\ -j\omega C_{\text{pul}} \int_0^d E^{\text{inc}}_z(x, z) dz \end{bmatrix} \quad (12)$$

where  $V_1$  and  $V_2$  are the coupled voltages across the two ends,  $\rho_1$  and  $\rho_2$  are the reflection coefficients at two ends,  $C_{\text{pul}}$  is the per unit length capacitance,  $H_y^{\text{inc}}$  is the incident magnetic field in the y-direction, and  $E_z^{\text{inc}}$  is the incident electric field in the z-direction. When the coupling is calculated analytically rather than using the full-wave simulations, the transmission coefficients to the plane wave port can be directly found by:

$$S_{13} = V_1^- / E_{\text{inc}}|_{V_1^+=0, V_2^+=0}, \quad S_{23} = V_2^- / E_{\text{inc}}|_{V_1^+=0, V_2^+=0} \quad (13)$$

The advantages of using BLT equations to model straight microstrip lines are: a) pre-characterization time is faster than full-wave simulation; and b) the S-parameters of a transmission line of arbitrary length can be calculated “on the fly,” and thus eliminate the need to discretize the variable length of the segments. Although full-wave simulations are still needed in the pre-characterization phase of realistic PCB geometries (for non-straight trace segments and IC packages), the BLT equations can be used to further reduce the computational time as well as the potential number of segments needed, since any trace length can be supported (as opposed to representing a straight trace with many short segments).

### 3.3. MODELING OF TRACE BENDS

The modeling of small segments such as trace bend is more challenging. The transmission lines are often considered not to be the dominant radiating structures [14], but the discontinuities such as trace bends can be more significant coupling structures as the non-TEM waves are inevitably excited at discontinuities. A simplified lumped LC model of a trace bend was described in [13], however, this equivalent model ignores both the electromagnetic coupling to the bend and the distributed effects at higher frequencies.

As has been discussed in Section 3, the waveguide ports are preferred for excitations for the segment modeling. Defining lumped ports at the ends of the segments is undesirable because of the additional radiation due to the vertical port currents and excessive port inductance. However, defining two waveguide ports at the ends of the short bend segment might be geometrically impossible because of the port intersection.

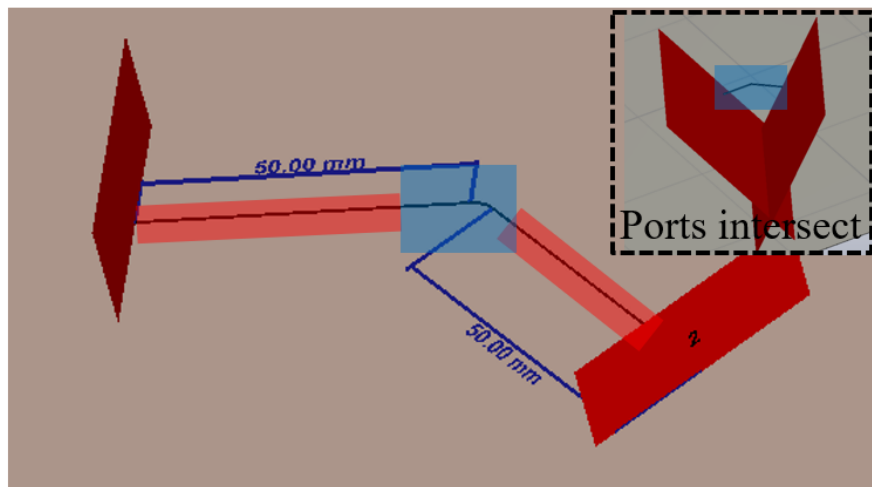


Figure 7. Two straight traces are added to a small trace bend to allow simulation with waveguide ports.

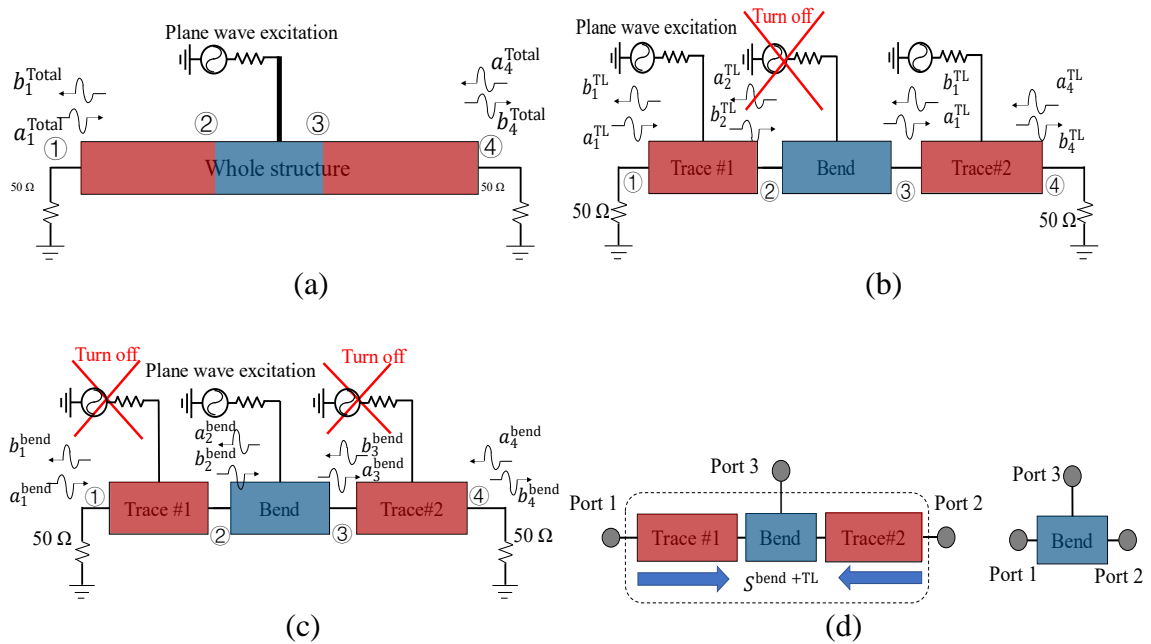


Figure 8. De-embedding the characteristics of the bend: (a) the plane wave excitation applied to all segments; (b) the excitation of the bend is turned off; (c) only the bend is stimulated by the plane wave; (d) de-embedding of the bend segment.

A solution for this problem is to add straight transmission lines at the ends of a bend segment as shown in Figure 7 to enable the definition of the waveguide ports and later de-embed the straight segments. The S-parameter of the entire structure  $S^{\text{Total}}$  shown in Figure 8 can be obtained following the procedure described in Section 3. Conventional de-embedding procedures [15] cannot be directly applied to this case, however, because the plane wave is coupled directly to each of the segments (Figure 8 (a)). The middle segment can instead be de-embedded using the superposition principle. Since the segmented structure is linear, the incident and reflected waves at nodes 1-4 of the circuit (a) are the superposition of the corresponding quantities in circuits (b) and (c). The characteristics of the straight transmission line segments (including the coupling to the plane wave) are known from either full-wave simulations or from an analytical

equation, as discussed previously. The two-port S-parameters of the bend can then be extracted using 2x-thru de-embedding [15]. The 4 elements ( $S_{11}^{\text{bend}}$ ,  $S_{21}^{\text{bend}}$ ,  $S_{12}^{\text{bend}}$ ,  $S_{22}^{\text{bend}}$ ) of  $S^{\text{bend}}$  can thus be obtained.

The forward and reverse propagating voltages at the node  $k$  are equal to  $a_k^{\text{Total}}$ ,  $b_k^{\text{Total}}$  for a plane wave excitation applied to all segments (circuit a), equal to  $a_k^{\text{TL}}$ ,  $b_k^{\text{TL}}$  when the plane wave excitation is applied to the transmission line segments (circuit b), and equal to  $a_k^{\text{bend}}$ ,  $b_k^{\text{bend}}$  when the plane wave excitation is applied to the bend segment (circuit c). Since there are no sources at node 1 and 4 and the loads are non-reflective,

$$a_1^{\text{TL}} = a_4^{\text{TL}} = a_1^{\text{Total}} = a_4^{\text{Total}} = 0. \quad (14)$$

Assuming a certain amplitude of the incident wave at the plane wave port  $V_{\text{inc}}^+$  in circuit (a), the outgoing waves at nodes 1 and 4 can be found as

$$b_1^{\text{Total}} = V_{\text{inc}}^+ S_{13}^{\text{Total}}; \quad b_4^{\text{Total}} = V_{\text{inc}}^+ S_{23}^{\text{Total}}. \quad (15)$$

Using superposition, the outgoing waves in circuit I can be expressed as

$$b_1^{\text{bend}} = b_1^{\text{Total}} - b_1^{\text{TL}}, \quad b_4^{\text{bend}} = b_4^{\text{Total}} - b_4^{\text{TL}}. \quad (16)$$

This operation allows the S-parameters to be found for the structure in circuit (d) which has the plane wave port at the bend segment only and two two-port fixtures at ports 1 and 2:

$$S_{13}^{\text{bend+TL}} = S_{31}^{\text{bend+TL}} = \frac{b_1^{\text{bend}}}{V_{\text{inc}}^+} = \frac{b_1^{\text{Total}} - b_1^{\text{TL}}}{V_{\text{inc}}^+} \quad (17)$$

$$S_{23}^{\text{bend+TL}} = S_{32}^{\text{bend+TL}} = \frac{b_4^{\text{bend}}}{V_{\text{inc}}^+} = \frac{b_4^{\text{Total}} - b_4^{\text{TL}}}{V_{\text{inc}}^+} \quad (18)$$

The rest of the elements in  $S^{\text{bend+TL}}$  are identical to those in  $S^{\text{Total}}$ . Now circuit (d) can be treated with a fixture de-embedding procedure [15] to obtain the full  $S^{\text{bend}}$  matrix.

#### **4. ASSESSMENT ACCURACY OF THE SEGMENTATION METHOD**

The segmentation approach implicitly assumes that the size of the return plane and the location of the segments with respect to the edges of the return plane is not important, and similarly ignores mutual couplings between segments. The algorithm also assumes that the field probes (in Figure 6) are placed infinitely far from the segment, while in reality they are located at a finite distance. Errors due to these assumptions are discussed below.

##### **4.1. TRANSLATION INDUCED ERROR**

The translation operation assumes that probes are placed infinitely far from the device under test, but in reality the position of the probes relative to the segments changes due to the segment translation. The impact of the change in distance should generally be small, however, due to the relatively small size of a typical PCB (usually less than tens of cm) compared to the distance to the probes (3 m in this study). The size of the typical error caused by ignoring the change in distance was studied.

To evaluate the translation error, the radiated E-fields generated by an infinitesimal dipole antenna were compared when the dipole was placed at the origin and when it was translated by (10, 10, 0) cm with the “probes” placed at a 3 m distance as

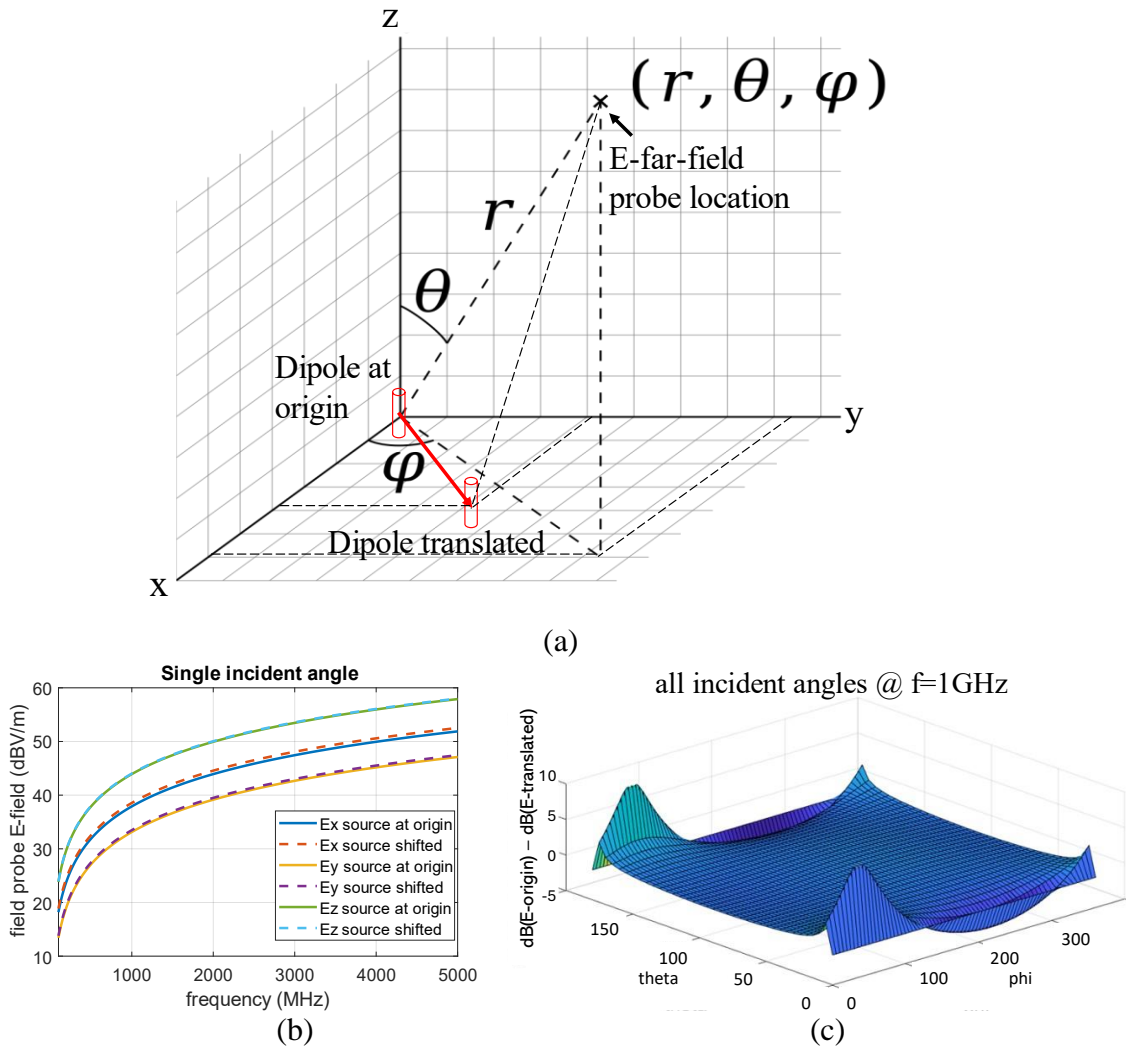


Figure 9. Investigation of the translation error: (a) infinitesimal dipole antenna at the origin and after translation; (b) magnitudes of the radiated E-fields; (c) difference in radiation patterns on a decibel scale.

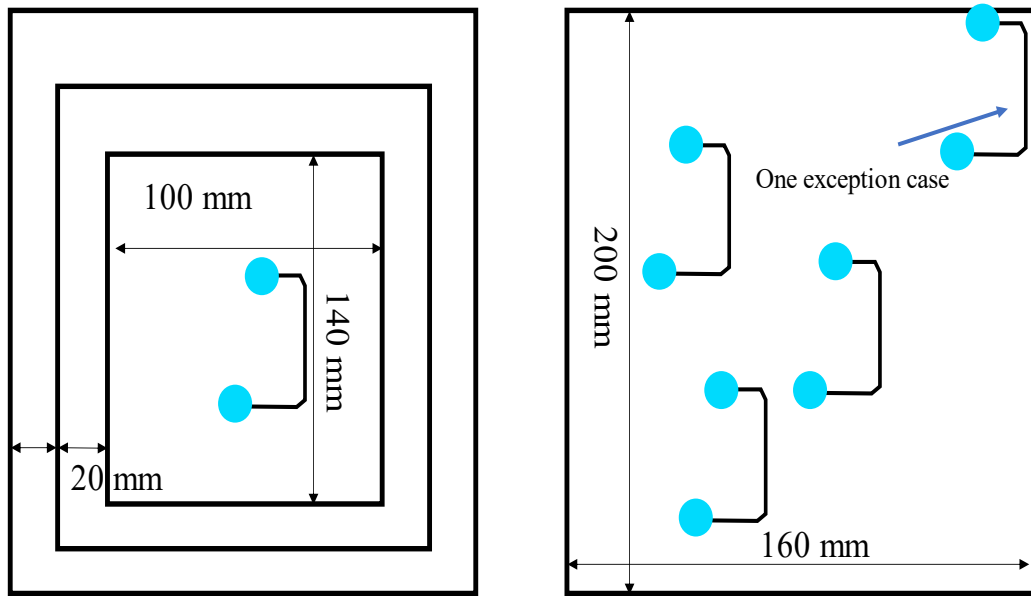
shown in Figure 9 (a). The infinitesimal dipole antenna was selected to avoid any effects from the PCB ground plane (which will be discussed in Section 4) and because radiated fields can be calculated from closed-form equations. As shown in Figure 9 (b) for an incident angle  $\theta = 60^\circ$ ,  $\phi = 30^\circ$  (some other incident angles were also looked at, produce similar level of errors), the radiated E-field changes by less than 0.6 dB due to translation. As shown in Figure 9 (c) at 1 GHz, the change in the measured field is less than 0.6 dB

for most incident angles of arrivals, except when the angles of illumination are  $\theta = 0$  or  $\theta = 180^\circ$  (where the radiation is negligible from the dipole antenna, and small errors could cause a large - but unimportant - change in magnitude). The overall error was considered acceptable for this study. If needed, the error could be reduced by moving the probes farther away.

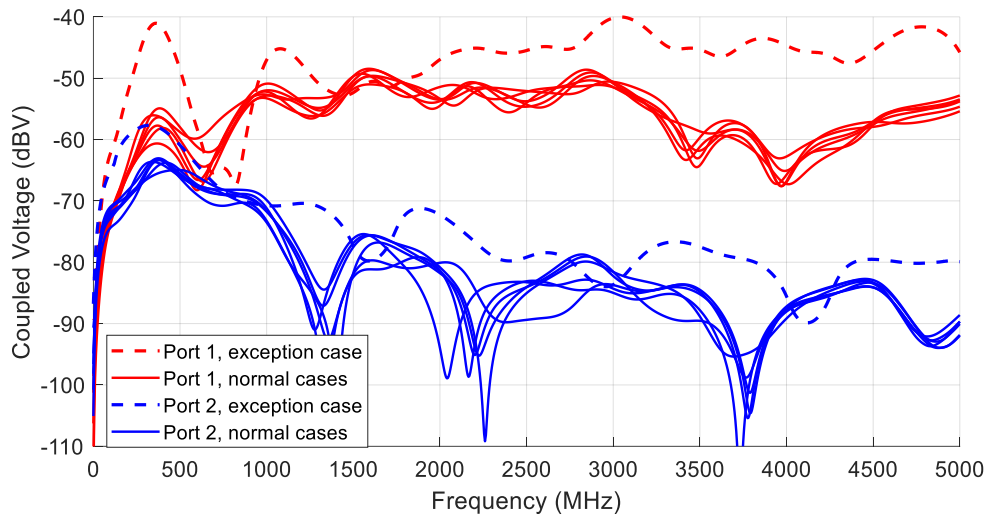
#### 4.2. IMPACT OF FINITE GROUND PLANE

One of the more important assumptions in the segmentation technique is that the ground plane is large enough that the electromagnetic coupling to each segment remains the same when the segments are shifted to a new location. As shown earlier, when the traces are placed too close to the edge of the return plane, the electromagnetic coupling increases dramatically, but varies little once the traces are within about a couple of centimeters away from the edge when considering the frequency range below several GHz [16]. While we assume here that the probability of a trace to be close to the edge is sufficiently small that it can be ignored, it is worthwhile to understand the potential error caused by the finite size of the ground plane.

Figure 10 (a) shows four example cases where the same trace is placed on ground planes of different sizes and at different distances to the plane edge. Except for the case marked as an intentional outlier, all the others are never particularly close to the edge. Simulations of the coupled voltages across the two terminals (port 1 loaded by a  $100 \Omega$  resistor and port 2 loaded by a  $20 \text{ pF}$  capacitor) of different board sizes/trace orientations are shown in Figure 10 (b) (the results are for an incident angle and polarization of  $\theta = 60^\circ, \varphi = 30^\circ, \gamma = 30^\circ$  some other incident angles and polarizations were also checked,



(a)



(b)

Figure 10. Impact of the size of the ground plane and relative position of the trace: (a) trace configurations with different ground plane sizes and different trace placement positions; (b) variation in coupled voltage (solid lines: traces with  $>2$  cm margin to the edges; dashed lines: trace close to the edge).

have similar behaviors). The solid lines are the coupled voltages of the traces placed with at least several centimeter margin to the edges and the dashed lines are for the outlier case very close to the edge. The voltages coupled to each trace configuration with more than a

couple centimeter margin to the edges are largely the same but may vary by several decibels mainly due to the shift of the resonances. While when the trace is placed close to the edges, the coupling level is noticeably increased. These results demonstrate that relatively small errors can be expected due to a finite size of the ground plane, however the method can underestimate coupling to the incoming plane waves when a trace is routed close to the PCB edges.

### **4.3. LIMITATIONS AND THE POTENTIAL ERRORS**

Except for the assumptions of sufficiently large ground plane and not allowing traces to be close to the edges, several other important assumptions may also affect the electromagnetic coupling prediction accuracy:

- Common-mode coupling is not considered: the common-mode coupling is more likely to have an impact when wires/cable bundles are attached [17], [18], [19]. The common-mode couplings on PCBs without attached cables are typically (but not always) negligible. However, the segmentation concept can still be used to predict common mode coupling but is more technically challenging [20].
- Crosstalk/mutual coupling between the segmented structures are ignored: as the electromagnetic characteristics of each segment are pre-modeled without the presence of other structures, when the segments are cascaded and analyzed by the equivalent circuit model, any mutual coupling behavior [21] is ignored, which may introduce additional errors.

- Solid ground plane assumption: for some PCBs, there may exist slots on the ground plane. Traces running across the slotted ground will be significantly coupled to the external wave disturbances [22]. However, EMC engineers are well aware of these effects and most well-designed products should have avoided using such geometries.
- Accumulated numerical error due to a large number of cascaded segments: some amount of numerical error inevitably exists for each segment at the pre-characterization phase. These errors can accumulate therefore it is better to minimize the number of segments used. Using BLT to characterize the traces had the advantage that any straight traces can be represented with a single segment, whereas many smaller segments might have to be cascaded when using full-wave simulations if the correct length is not already available in the segment library.
- Pre-characterization is mandatory to enable cascading the segments: when a structure of interest is not available in the segment library, it is required to utilize full-wave simulation or use analytical formulas (when available) to obtain the equivalent generalized S-parameter representation. After the characterization is finished, the component is ready for picking up from the data library and placement.

## 5. STATISTICAL ANALYSIS OF COUPLING USING THE SEGMENTATION METHOD

Relevant statistical characteristics of electromagnetic coupling to DUTs include the average, maximum value and standard deviation of the coupled voltages, and more generally the probability density of the voltage amplitudes as a function of the incident and polarization angles. Compared to other researchers' study of the statistical EM coupling [23], the proposed segmentation method allows to use more random variables and more complicated geometries. Although some errors due to the segmentation are inevitable, their impact is expected to be small when considering the statistical analysis of coupling from many angles of arrival and many random trace/PCB configurations [11]. The sacrifice in accuracy is made to the benefit of the speed of calculation. Once the segments have been characterized in a full-wave simulation, no further full-wave simulations are required. Characterized segments can be placed in a library and connected to represent a wide variety of complicated PCB structures (e.g., an IC connected to a meandering trace, which is connected to another IC). Estimating coupling only requires solving a simple circuit problem.

To illustrate this the segmentation method was used to analyze the average coupled voltages of 500 random geometries as shown in Figure 11 (a), which consisted of two IC packages connected through an L-shaped microstrip trace. The interconnect trace was composed of two straight segments plus one 90-degree bend. The length of each straight trace segment was a random variable with uniform distribution from 5 mm to 100 mm. The terminations of the ICs were set to 100  $\Omega$  and 20 pF, respectively. The detailed

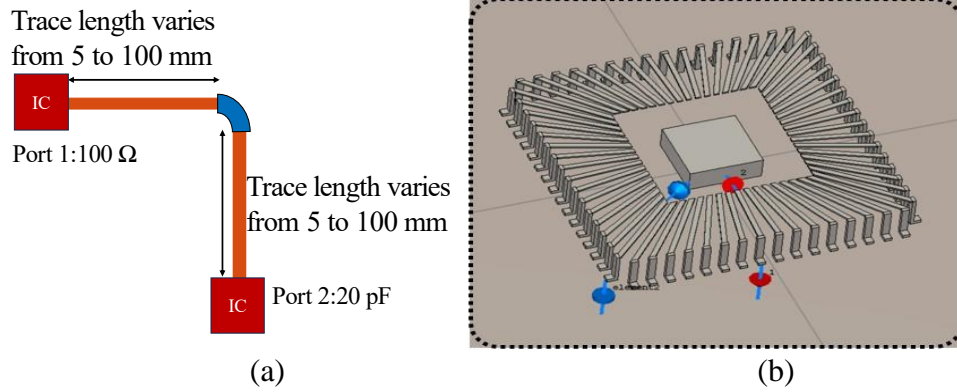


Figure 11. Random IC-trace-IC geometry: (a) Segments and the connections; (b) detailed IC structure model.

IC package structure is shown in Figure 11 (b). The port settings and equivalent circuit representations are explained in details in [11].

The segmentation method was used to estimate coupling to 500 randomly generated structures. For each geometry the absolute value of the coupled voltages at the terminations were averaged over all incidence angles and polarizations as

$$V_{\text{avg } 1,2}(f) = \frac{1}{N_\gamma N_\varphi N_\theta} \sum_{\gamma=0 \sim \frac{\pi}{2}} \sum_{\varphi=0 \sim 2\pi} \sum_{\theta=0 \sim \pi} |V_{1,2}(\theta, \varphi, \gamma, f)| \sin \theta, \quad (19)$$

where  $N_\theta = 13$ ,  $N_\varphi = 25$ , and  $N_\gamma = 10$  are the numbers of the angles analyzed (every 15 degrees for the elevation/azimuth angles and every 10 degrees for the polarization angle). The estimated coupled voltages at each port for each geometry are shown in Figure 12 (a). The coupled voltages averaged over the 500 geometries are shown in Figure 12 (b). An example of the probability density (in a form of a histogram) for the absolute value of the induced voltage at port 1 at 1 GHz is shown in Figure 12 (c).

The computational efficiency of the proposed segmentation method is illustrated by the following analysis. Suppose that a total of  $N_g$  geometries for  $N_a$  illumination or

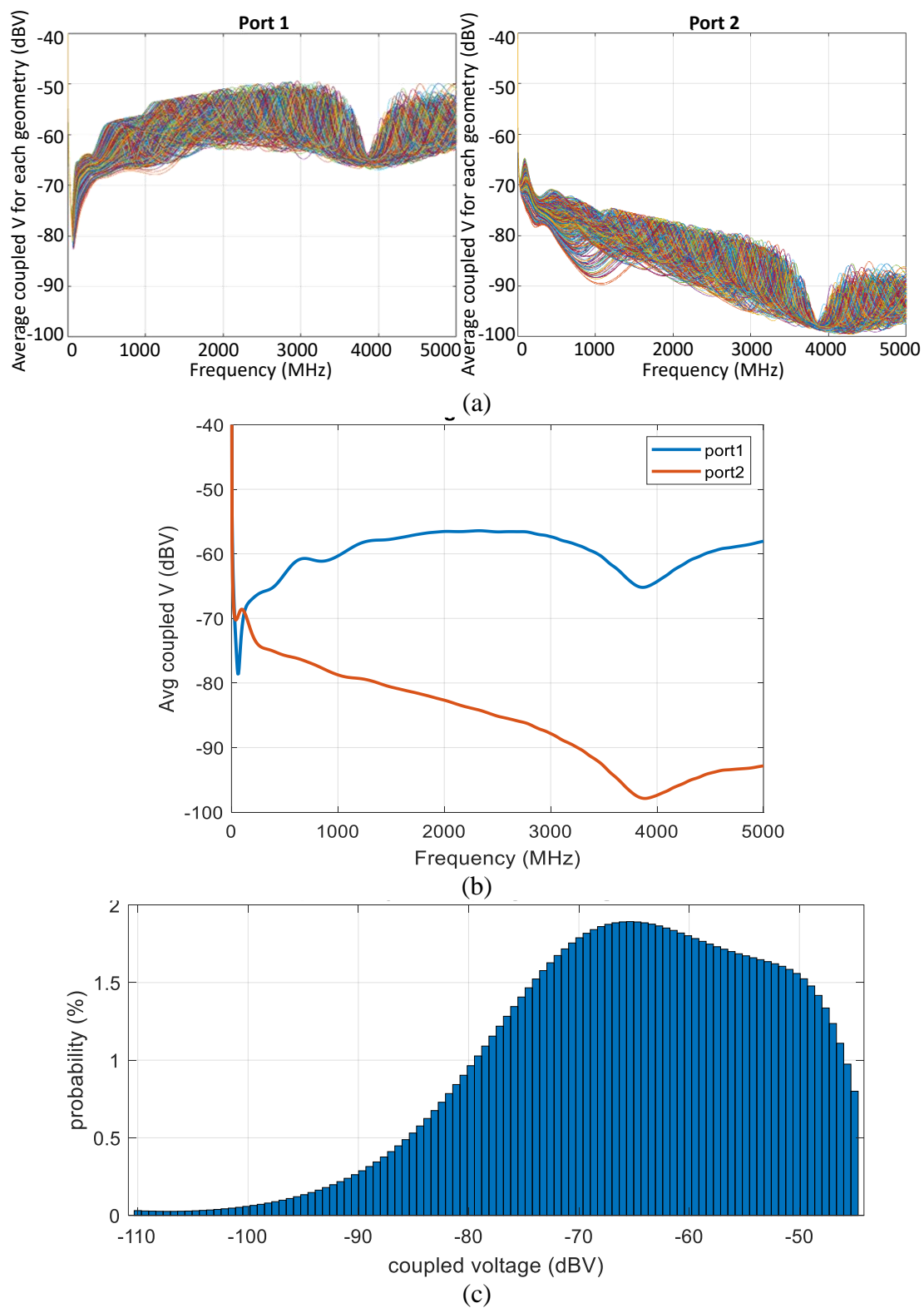


Figure 12. Statistical analysis of random IC-trace-IC geometries: (a) coupling to each geometry averaged over angles of incidence; (b) averaged over all geometries; (c) histogram of the coupled voltage at port 1 at 1 GHz.

polarization angles need to be simulated. The calculations could be performed in any of the following ways:

1. Estimate coupling using full-wave simulations for every angle of arrival for each geometry (brute-force).
2. Use reciprocity to determine coupling from all angles of arrival from a single simulation of each geometry using (1) (brute force with reciprocity).
3. Use the segmentation approach to estimate coupling for each geometry, where the characteristics of individual segments must be pre-computed via full-wave simulations (assuming they are not already available in a library).

Each approach involves a different number of full-wave, reciprocal and circuit simulations. Let us denote the time of the full-wave simulations as  $t_{fw}$  and assume that an equal simulation time is needed for the simulation of the complete geometry and to characterize each segment (in reality the size and the geometrical complexity of the segments is much lower than the full geometry and would take less time to simulate, but we are using this worst case estimate here for simplicity). Let us also denote the time to perform the reciprocity calculation per angle as  $t_r$ , and the time needed to perform the simulation of the circuit containing the connected segments as  $t_{cir}$  (a circuit is created and simulated for each angle of arrival). The time needed to obtain the results using the brute-force approach without reciprocity is then

$$T_{bf} = N_g N_a t_{fw}, \quad (20)$$

the time needed using the brute-force approach with reciprocity is calculated as the following equation:

$$T_{bf,rec} = N_g (t_{fw} + N_a t_r) \quad (21)$$

and the time needed for the segmentation approach with  $N_{\text{seg}}$  segments is

$$T_{\text{seg}} = N_{\text{seg}}(t_{\text{fw}} + N_a t_r) + N_a t_{\text{cir}}. \quad (22)$$

On a Windows 10 computer with an Intel i5 CPU with 16 GB of memory, the time required to implement the reciprocity calculation ( $t_r$ ) was found to be 2.7 ms per angle and the circuit simulation time ( $t_{\text{cir}}$ ) for the segmentation approach was found to be 5.5 ms (both calculations were implemented in MATLAB and the time was measured determined using “cputime” variable). The full-wave simulation time  $t_{\text{fw}}$  was assumed to be 30 minutes. Table 1 shows the estimated time required for each technique for 500 geometries and 3250 angles, assuming that the PCB geometries could be represented with 5 segments.

Table 1 Computational Time Comparison

	Brute-force	Brute-force with reciprocity	Segmentation
Estimation	92.75 years	10.47 days	2.52 hours
Actual	N/A	N/A	6.7 hours

Table I demonstrates that the segmentation approach requires significantly less time to simulate coupling to a large number of geometries compared to methods using full-wave simulations of complete geometries. The actual simulation time, listed in the second row of the table, was significantly longer than the estimated time due to the need to read and save a large number of data files, but still significantly shorter than the time

required by alternative methods. The calculation time could be significantly reduced through optimization of the code, or by storing data in cache memory or on an SSD. Even with the limitations of the non-optimized code, however, the segmentation approach was nearly 40x faster than using full-wave simulations (brute-force with reciprocity).

## 6. DISCUSSION AND CONCLUSIONS

The proposed segmentation method enables a fast electromagnetic coupling analysis to complicated PCB structures by cutting the structure into small pieces, or segments. Each segment is pre-characterized to determine its electrical characteristics (the S-parameters), as well as its ability to generate far-field emissions or to couple energy from an incident plane-wave. The pre-characterized segments can then be assembled to simulate coupling to or radiation from complicated structures without the need to perform additional full-wave simulations. The fact that the characterization of individual segments can be placed in a library and reused (e.g. that a characterization of a 45° trace bend may be characterized once but used many times in many circuits) presents a significant advantage since calculations with pre-characterized segments can be done very quickly with little computational effort, and with no computationally burdensome full-wave simulations. The trade-off of this method is some loss of accuracy compared to the full-wave simulation of the complete geometry.

Results were presented here for frequency-domain analysis of structures containing microstrip traces and IC packages. The approach could be relatively easily extended to other PCB components like via transitions, two-terminal SMT components, and the like. Non-radiating structures like co-planar traces and striplines could be represented with

conventional two-port S-parameters, since the third “radiation” port is not needed. Use of the technique with more complicated radiating structures, like a trace over a gap in the return plane, should be studied. The approach can also be extended to estimate time-domain waveforms coupled to individual pins, by utilizing the estimated frequency-domain response along with the time-domain characteristics of the incident waveform. Such a transformation would allow statistical analysis of time-domain characteristics of the coupled voltage like its peak level.

One unique potential advantage of the approach is that, since the electromagnetic coupling to each segment is calculated separately and the combined segments obey superposition, the technique allows one to estimate the contributions of each individual segment to the coupled voltage. The most dominant coupling structures can thus be identified to better understand the coupling mechanisms.

## REFERENCES

- [1] M. Leone and H. L. Singer, “On the coupling of an external electromagnetic field to a printed circuit board trace,” *IEEE Transactions on Electromagnetic Compatibility*, vol. 41, no. 4, pp. 418-424, Nov. 1999, doi: 10.1109/15.809842.
- [2] P. Bernardi and R. Cicchetti, “Response of a planar microstrip line excited by an external electromagnetic field,” *IEEE Transactions on Electromagnetic Compatibility*, vol. 32, no. 2, pp. 98-105, May 1990, doi: 10.1109/15.52405.
- [3] M. Leone and V. Navratil, “On the external inductive coupling of differential signalling on printed circuit boards,” *IEEE Transactions on Electromagnetic Compatibility*, vol. 46, no. 1, pp. 54-61, Feb. 2004, doi: 10.1109/TEMPC.2004.823611.

- [4] S. Park, Y. Kami and Y. Nahm, "Coupling analysis of complex-layout traces using a circuit-concept approach," *IEEE Transactions on Electromagnetic Compatibility*, vol. 56, no. 1, pp. 208-220, Feb. 2014, doi: 10.1109/TEMPC.2013.2273078.
- [5] F. Vanhee, D. Pissort, J. Catrysse, G. A. E. Vandenbosch and G. G. E. Gielen, "Efficient reciprocity-based algorithm to predict worst case induced disturbances on multiconductor transmission lines due to incoming plane waves," *IEEE Transactions on Electromagnetic Compatibility*, vol. 55, no. 1, pp. 208-216, Feb. 2013, doi: 10.1109/TEMPC.2012.2208754.
- [6] H. Zhao, X. Gao, B. Wang, E. Li and E. K. Chua, "Efficient analysis of radiated immunity of printed circuit boards using SPICE," *2012 IEEE International Symposium on Electromagnetic Compatibility*, 2012, pp. 289-293, doi: 10.1109/ISEMC.2012.6351768.
- [7] J. Hunter, S. Xia, A. Harmon, A. Hassan, V. Khilkevich and D. Beetner, "Modeling and statistical characterization of electromagnetic coupling to electronic devices," *2021 United States National Committee of URSI National Radio Science Meeting (USNC-URSI NRSM)*, 2021, pp. 14-15, doi: 10.23919/USNC-URSINRSM51531.2021.9336496.
- [8] D. Drogoudis, J. Van Hese, B. Boesman and D. Pissort, "Combined circuit/full-wave simulations for electromagnetic immunity studies based on an extended S-parameter formulation," *2014 IEEE 18<sup>th</sup> Workshop on Signal and Power Integrity (SPI)*, 2014, pp. 1-4, doi: 10.1109/SaPIW.2014.6844551.
- [9] F. V. Zonouz, N. Masoumi and M. Mehri, "Effect of IC package on radiated susceptibility of board level interconnection," *2015 International Conference on Synthesis, Modeling, Analysis and Simulation Methods and Applications to Circuit Design (SMACD)*, 2015, pp. 1-4, doi: 10.1109/SMACD.2015.7301676.
- [10] V. S. Reddy, P. Kralicek and J. Hansen, "A novel segmentation approach for modeling of radiated emission and immunity test setups," *IEEE Transactions on Electromagnetic Compatibility*, vol. 59, no. 6, pp. 1781-1790, Dec. 2017, doi: 10.1109/TEMPC.2017.2699480.
- [11] S. Xia et al., "A fast cascading method for predicting the coupling from external plane waves to PCBs," *2022 IEEE International Symposium on Electromagnetic Compatibility & Signal/Power Integrity (EMCSI)*, Spokane, WA, USA, 2022, pp. 152-157, doi: 10.1109/EMCSI39492.2022.9889338.

- [12] Stutzman, W. L., & Thiele, G. A. (2013). *Antenna Theory and design*. Wiley.
- [13] S. J. Guo, L. S. Wu, M. Tang and J. F. Mao, "Analysis of illuminated bent microstrip line based on Baum-Liu-Tesche (BLT) equation," 2015 IEEE Electrical Design of Advanced Packaging and Systems Symposium (EDAPS), Seoul, Korea (South), 2015, pp. 159-162, doi: 10.1109/EDAPS.2015.7383691.
- [14] P. Maheshwari, V. Khilkevich, D. Pommerenke, H. Kajbaf and J. Min, "Application of emission source microscopy technique to EMI source localization above 5 GHz," 2014 IEEE International Symposium on Electromagnetic Compatibility (EMC), Raleigh, NC, USA, 2014, pp. 7-11, doi: 10.1109/ISEMC.2014.6898933.
- [15] B. Chen, J. He, Y. Guo, S. Pan, X. Ye and J. Fan, "Multi-ports ([2n] 2×-thru de-embedding: theory, validation, and mode conversion characterization," IEEE Transactions on Electromagnetic Compatibility, vol. 61, no. 4, pp. 1261-1270, Aug. 2019, doi: 10.1109/TEMC.2019.2908782.
- [16] T. Hubing, "PCB EMC design guidelines: a brief annotated list," 2003 IEEE Symposium on Electromagnetic Compatibility. Symposium Record (Cat. No.03CH37446), Boston, MA, USA, 2003, pp. 34-36 vol.1, doi: 10.1109/ISEMC.2003.1236559.
- [17] C. Su and T. H. Hubing, "Imbalance difference model for common-mode radiation from printed circuit boards," IEEE Transactions on Electromagnetic Compatibility, vol. 53, no. 1, pp. 150-156, Feb. 2011, doi: 10.1109/TEMC.2010.2049853.
- [18] S. Deng, T. Hubing and D. Beetner, "Estimating maximum radiated emissions from printed circuit boards with an attached cable," IEEE Transactions on Electromagnetic Compatibility, vol. 50, no. 1, pp. 215-218, Feb. 2008, doi: 10.1109/TEMC.2007.915288.
- [19] Hwan-Woo Shim and T. H. Hubing, "Model for estimating radiated emissions from a printed circuit board with attached cables due to voltage-driven sources," IEEE Transactions on Electromagnetic Compatibility, vol. 47, no. 4, pp. 899-907, Nov. 2005, doi: 10.1109/TEMC.2005.859060.
- [20] J. Hunter et al., "A segmentation strategy for structures with common mode coupling," 2022 IEEE International Symposium on Electromagnetic Compatibility & Signal/Power Integrity (EMCSI), Spokane, WA, USA, 2022, pp. 415-420, doi: 10.1109/EMCSI39492.2022.9889666.

- [21] M. Tang, J. Lu, J. Mao and L. Jiang, "A systematic electromagnetic-circuit method for EMI analysis of coupled interconnects on dispersive dielectrics," *IEEE Transactions on Microwave Theory and Techniques*, vol. 61, no. 1, pp. 1-13, Jan. 2013, doi: 10.1109/TMTT.2012.2220562.
- [22] A. B. Kouki, R. Mittra and Chi Hou Chan, "Analysis of a thin slot discontinuity in the reference plane of a microstrip structure," *IEEE Transactions on Microwave Theory and Techniques*, vol. 41, no. 8, pp. 1356-1362, Aug. 1993, doi: 10.1109/22.241675.
- [23] M. Mehri, N. Masoumi and S. Heidari, "Electromagnetic susceptibility analysis of PCBs using predictive method," *2015 International Conference on Synthesis, Modeling, Analysis and Simulation Methods and Applications to Circuit Design (SMACD)*, Istanbul, Turkey, 2015, pp. 1-4, doi: 10.1109/SMACD.2015.7301686.

## SECTION

### 3. CONCLUSIONS AND SUMMARY

RF interference control has been discussed in various of aspects including the noise source modeling, nonlinear behavior quantification, and EM coupling analysis. The challenges of solving/identifying the RF interference problems are the lack of physics-based understandings of the EM coupling mechanism and the missing linkage to the spectrum generation due to the nonlinear distortions. Paper I covers the complete work flow using the dipole-moment-based coupling framework as tool to identify the dominant noise source. The reciprocity-based theorem can help with a better physics-based understanding and is also powerful for what-if scenario studies. This EM based reciprocity can also be extended to speed up the computational time for far-field coupling scenarios. The detailed procedures of taking advantage of the far-field reciprocity and segmentation method for fast EM coupling analysis has been covered in Paper IV.

In the second and the third papers, the main focus is on PIM only. Paper II covers the innovative PIM-free solution with anodization process. The PIM behavior and the capacitive contact impedance are evaluated in the proper methods. Paper III covers setting up the mathematical linkage from the typical two-tone results to the wideband spectrum, which is more straight-forward and intuitive to desense problems. Furthermore, the constructed nonlinear model can be used for setting up the target of measurement dynamic ranges with a clear figure-of-merit.

## REFERENCE

- [1] E. X. Liu, W. J. Zhao, B. Wang, S. Gao and X. C. Wei, "Near-field scanning and its EMC applications," *2017 IEEE International Symposium on Electromagnetic Compatibility & Signal/Power Integrity (EMCSI)*, 2017, pp. 327-332, doi: 10.1109/ISEMC.2017.8077889.
- [2] Y. F. Shu and X. C. Wei, "PCB electromagnetic interference modelling based on reciprocity theorem," *2017 IEEE Electrical Design of Advanced Packaging and Systems Symposium (EDAPS)*, 2017, pp. 1-3, doi: 10.1109/EDAPS.2017.8276939.
- [3] W. Zhang et al., "Improvement on the Accuracy of Near-Field Scanning Using Tangential Electric Field Probe," *2021 IEEE International Joint EMC/SI/PI and EMC Europe Symposium*, 2021, pp. 370-375, doi: 10.1109/EMC/SI/PI/EMCEurope52599.2021.9559226.
- [4] J. Pan, X. Gao and J. Fan, "Identifying Interference From Multiple Noise Sources Using Only Magnetic Near Fields," *IEEE Transactions on Electromagnetic Compatibility*, vol. 63, no. 2, pp. 580-588, April 2021, doi: 10.1109/TEMC.2020.3020049.
- [5] J. Zhang, K. W. Kam, J. Min, V. V. Khilkevich, D. Pommerenke, and J. Fan, "An Effective Method of Probe Calibration in Phase-Resolved Near-Field Scanning for EMI Application," *IEEE Transactions on Instrumentation and Measurement*, vol. 62, no. 3, pp. 648-658, 2013.
- [6] H. Wang, V. Khilkevich, Y. Zhang and J. Fan, "Estimating Radio-Frequency Interference to an Antenna Due to Near-Field Coupling Using Decomposition Method Based on Reciprocity," *IEEE Transactions on Electromagnetic Compatibility*, vol. 55, no. 6, pp. 1125-1131, Dec. 2013, doi: 10.1109/TEMC.2013.2248090.
- [7] J. Pan et al., "Radio-Frequency Interference Estimation Using Equivalent Dipole-Moment Models and Decomposition Method Based on Reciprocity," *IEEE Transactions on Electromagnetic Compatibility*, vol. 58, no. 1, pp. 75-84, Feb. 2016, doi: 10.1109/TEMC.2015.2496210.
- [8] Y. Sun, B. Tseng, H. Lin and C. Hwang, "RFI Noise Source Quantification Based on Reciprocity," *2018 IEEE Symposium on Electromagnetic Compatibility, Signal Integrity and Power Integrity (EMC, SI & PI)*, 2018, pp. 548-553, doi: 10.1109/EMCSI.2018.8495187.
- [9] L. Zhang et al., "Radio-Frequency Interference Estimation for Multiple Random Noise Sources," *IEEE Transactions on Electromagnetic Compatibility*, doi: 10.1109/TEMC.2021.3117845.

- [10] Balanis, C. A. (1997). *Antenna theory: Analysis and design*. Wiley.
- [11] A. Taaghool and T. K. Sarkar, "Near-field to near/far-field transformation for arbitrary near-field geometry, utilizing an equivalent magnetic current," *IEEE Trans. Electromagn. Compat.*, vol. 38, no. 3, pp. 536–542, Aug. 1996. [5] J. Pan, X. Gao, and J. Fan, "Far-field prediction by only magnetic near
- [12] Q. Huang, T. Enomoto, S. Seto, K. Araki, J. Fan, C. Hwang "Accurate and Fast RFI Prediction Based on Dipole Moment Sources and Reciprocity" *Proc. of DesignCon*, 2018.
- [13] Q. Huang, Y. Liu, L. Li, Y. Wang, C. Wu and J. Fan, "Radio frequency interference estimation using transfer function based dipole moment model," *2018 IEEE International Symposium on Electromagnetic Compatibility and 2018 IEEE Asia-Pacific Symposium on Electromagnetic Compatibility (EMC/APEMC)*, Singapore, 2018, pp. 115-120.
- [14] G. Cho, J. Jin, H. Park, H. H. Park and C. Hwang, "Assessment of Integrated Circuits Emissions With an Equivalent Dipole-Moment Method," *IEEE Transactions on Electromagnetic Compatibility*, vol. 59, no. 2, pp. 633-638, April 2017, doi: 10.1109/TEMC.2016.2633332.
- [15] Q. Huang and J. Fan, "Machine Learning Based Source Reconstruction for RF Desense," *IEEE Transactions on Electromagnetic Compatibility*, vol. 60, no. 6, pp. 1640-1647, Dec. 2018, doi: 10.1109/TEMC.2018.2797132.
- [16] S. Lee et al., "Analytical intra-system EMI model using dipole moments and reciprocity," *2018 IEEE International Symposium on Electromagnetic Compatibility and 2018 IEEE Asia-Pacific Symposium on Electromagnetic Compatibility (EMC/APEMC)*, 2018, pp. 1169-1173, doi: 10.1109/ISEMC.2018.8393972.
- [17] C. Hwang, J. -D. Lim, G. Y. Cho, H. -B. Park and H. H. Park, "A Novel Shielding Effectiveness Matrix of Small Shield Cans Based on Equivalent Dipole Moments for Radio-Frequency Interference Analysis," *IEEE Transactions on Electromagnetic Compatibility*, vol. 58, no. 3, pp. 766-775, June 2016, doi: 10.1109/TEMC.2016.2536139.
- [18] W. Liu, Z. Yan, J. Wang, Z. Min and Z. Ma, "An Improved Equivalent Dipole Moment Source Model Based on Regularization Optimization Method for Near Field-Far Field Conversion," *IEEE Access*, vol. 8, pp. 42504-42518, 2020, doi: 10.1109/ACCESS.2020.2976907.
- [19] Q. Huang et al., "A Novel RFI Mitigation Method Using Source Rotation," *IEEE Transactions on Electromagnetic Compatibility*, vol. 63, no. 1, pp. 11-18, Feb. 2021, doi: 10.1109/TEMC.2020.2995828.

- [20] Y. Sun, H. Lin, B. -C. Tseng, D. Pommerenke and C. Hwang, "Mechanism and Validation of USB 3.0 Connector Caused Radio Frequency Interference," *IEEE Transactions on Electromagnetic Compatibility*, vol. 62, no. 4, pp. 1169-1178, Aug. 2020, doi: 10.1109/TEMPC.2019.2925935.
- [21] C. Hwang and Q. Huang, "IC placement optimization for RF interference based on dipole moment sources and reciprocity," *2017 Asia-Pacific International Symposium on Electromagnetic Compatibility (APEMC)*, 2017, pp. 331-333, doi: 10.1109/APEMC.2017.7975497.
- [22] C. Hwang et al., "Noise coupling path analysis for RF interference caused by LCD noise modulation," *2016 IEEE International Symposium on Electromagnetic Compatibility (EMC)*, 2016, pp. 348-352, doi: 10.1109/ISEMC.2016.7571671.
- [23] S. Xia, et al., "RFI Estimation for Multiple Noise Sources Due to Modulation at a Digital Mic Using Dipole Moment Based Reciprocity," *2020 IEEE International Symposium on Electromagnetic Compatibility & Signal/Power Integrity (EMCSI)*, 2020, pp. 1-5, doi: 10.1109/EMCSI38923.2020.9743517.
- [24] C. Hwang, D. Pommerenke, J. Fan, T. Enomoto, J. Maeshima and K. Araki, "Modeling and Estimation of LCD Noise Modulation for Radio Frequency Interference," *IEEE Transactions on Electromagnetic Compatibility*, vol. 59, no. 6, pp. 1685-1692, Dec. 2017, doi: 10.1109/TEMPC.2017.2705178.
- [25] C. Hwang, D. Pommerenke, J. Fan, T. Enomoto, J. Maeshima and K. Araki, "Wideband Noise Measurement Technique in Duplex Systems for RF Interference," *IEEE Transactions on Electromagnetic Compatibility*, vol. 60, no. 4, pp. 1038-1044, Aug. 2018, doi: 10.1109/TEMPC.2017.2782673.
- [26] L. Zhang et al., "Accurate RFI prediction of 3D non-planar connector with half magnetic dipole pattern," *2019 Joint International Symposium on Electromagnetic Compatibility, Sapporo and Asia-Pacific International Symposium on Electromagnetic Compatibility (EMC Sapporo/APEMC)*, 2019, pp. 770-773, doi: 10.23919/EMCSapporo/APEMC44270.2019.8976328.
- [27] Balanis, C.A. (1997) *Antenna theory: Analysis and design*. New York: Wiley.
- [28] Simmons, J. G. et al., "Generalized Formula for the Electric Tunnel Effect between Similar Electrodes Separated by a Thin Insulating Film," *Journal of Applied Physics*, 34(6), 1793-1803. doi: 10.1063/1.1702682
- [29] H. Yang, H. Wen, Y. Qi and J. Fan, "An Equivalent Circuit Model to Analyze Passive Intermodulation of Loose Contact Coaxial Connectors," *IEEE Transactions on Electromagnetic Compatibility*, vol. 60, no. 5, pp. 1180-1189, Oct. 2018, doi: 10.1109/TEMPC.2018.2794992.

- [30] J. Li et al., "Self-contact Introduced Passive Intermodulation Characterizations for Captured Springs," *2021 IEEE International Joint EMC/SI/PI and EMC Europe Symposium, Raleigh, NC, USA, 2021*, pp. 929-934, doi: 10.1109/EMC/SI/PI/EMCEurope52599.2021.9559265.
- [31] S. Xia et al., "Passive Intermodulation Under Different Spring Contact Conditions," *2022 IEEE International Symposium on Electromagnetic Compatibility & Signal/Power Integrity (EMCSI), Spokane, WA, USA, 2022*, pp. 12-16, doi: 10.1109/EMCSI39492.2022.9889661.
- [32] J. R. Wilkerson, P. G. Lam, K. G. Gard and M. B. Steer, "Distributed Passive Intermodulation Distortion on Transmission Lines," *IEEE Transactions on Microwave Theory and Techniques*, vol. 59, no. 5, pp. 1190-1205, May 2011, doi: 10.1109/TMTT.2011.2106138.
- [33] Holm, R. (1951). Errata, "The Electric Tunnel Effect across Thin Insulator Films in Contacts," *Journal of Applied Physics*, 22(9), 1217-1217. doi:10.1063/1.1700142
- [34] J. J. Henrie, A. J. Christianson and W. J. Chappell, "Linear–Nonlinear Interaction and Passive Intermodulation Distortion," in *IEEE Transactions on Microwave Theory and Techniques*, vol. 58, no. 5, pp. 1230-1237, May 2010, doi: 10.1109/TMTT.2010.2045527.
- [35] S. Xia et al., "Practical Fixture Design for Passive Intermodulation Tests for Flexible Metallic Contacts," *2022 IEEE International Symposium on Electromagnetic Compatibility & Signal/Power Integrity (EMCSI), Spokane, WA, USA, 2022*, pp. 17-22, doi: 10.1109/EMCSI39492.2022.9889578.
- [36] B. Chen, J. He, Y. Guo, S. Pan, X. Ye and J. Fan, "Multi-ports ( $2n$ )  $2\times$ -thru de-embedding: theory, validation, and mode conversion characterization," *IEEE Transactions on Electromagnetic Compatibility*, vol. 61, no. 4, pp. 1261-1270, Aug. 2019, doi: 10.1109/TEMC.2019.2908782.
- [37] J. Jeon, H. Lee, B. Pu, J. -H. Kim, N. Zhang and W. Nah, "Prediction of Impedance Characteristics of MLCC Using Multiconductor Transmission Line Theory," *IEEE Transactions on Electromagnetic Compatibility*, vol. 58, no. 6, pp. 1760-1771, Dec. 2016, doi: 10.1109/TEMC.2016.2588519.
- [38] L. E. Wojewoda, M. J. Hill, K. Radhakrishnan and N. Goyal, "Use Condition Characterization of MLCCs," *IEEE Transactions on Advanced Packaging*, vol. 32, no. 1, pp. 109-115, Feb. 2009, doi: 10.1109/TADVP.2008.2004811.
- [39] C. Hwang and J. Fan, "Modeling and Mitigation of Radio Frequency Interference for Wireless Devices," *IEEE Electromagnetic Compatibility Magazine*, vol. 12, no. 1, pp. 87-92, 1st Quarter 2023, doi: 10.1109/MEMC.2023.10136454.

- [40] R. Holm, "Errata, 'The Electric Tunnel Effect across Thin Insulator Films in Contacts,'" *Journal of Applied Physics*, vol. 22, no. 9, p. 1217, 1951, doi: 10.1063/1.1700142.
- [41] C. D. Bond, C. S. Guenzer, and C. A. Carosella, "Intermodulation generation by electron tunneling through aluminum-oxide films," *Proceedings of the IEEE*, vol. 67, no. 12, pp. 1643-1652, Dec. 1979, doi: 10.1109/PROC.1979.11544.
- [42] C. Vicente and H. L. Hartnagel, "Passive-intermodulation analysis between rough rectangular waveguide flanges," *IEEE Transactions on Microwave Theory and Techniques*, vol. 53, no. 8, pp. 2515-2525, Aug. 2005, doi: 10.1109/TMTT.2005.852771.
- [43] J. G. Simmons, "Generalized Formula for the Electric Tunnel Effect between Similar Electrodes Separated by a Thin Insulating Film," *Journal of Applied Physics*, vol. 34, no. 6, pp. 1793-1803, June 1963, doi: 10.1063/1.1702682.
- [44] L. Kogut and K. Komvopoulos, "Analytical current-voltage relationships for electron tunneling across rough interfaces," *Journal of Applied Physics*, vol. 97, 073701-073701, 2005, doi: 10.1063/1.1866472.
- [45] J. R. Wilkerson, K. G. Gard, A. G. Schuchinsky, and M. B. Steer, "Electro-Thermal Theory of Intermodulation Distortion in Lossy Microwave Components," *IEEE Transactions on Microwave Theory and Techniques*, vol. 56, no. 12, pp. 2717-2725, Dec. 2008, doi: 10.1109/TMTT.2008.2007084.
- [46] J. R. Wilkerson, P. G. Lam, K. G. Gard, and M. B. Steer, "Distributed Passive Intermodulation Distortion on Transmission Lines," *IEEE Transactions on Microwave Theory and Techniques*, vol. 59, no. 5, pp. 1190-1205, May 2011, doi: 10.1109/TMTT.2011.2106138.
- [47] A. P. Shitvov, D. S. Kozlov, and A. G. Schuchinsky, "Nonlinear Characterization for Microstrip Circuits With Low Passive Intermodulation," *IEEE Transactions on Microwave Theory and Techniques*, vol. 66, no. 2, pp. 865-874, Feb. 2018, doi: 10.1109/TMTT.2017.2758726.
- [48] Q. Jin, J. Gao, G. T. Flowers, Y. Wu, G. Xie, and L. Bi, "Modeling of Passive Intermodulation in Connectors With Coating Material and Iron Content in Base Brass," *IEEE Transactions on Microwave Theory and Techniques*, vol. 67, no. 4, pp. 1346-1356, April 2019, doi: 10.1109/TMTT.2019.2893193.
- [49] Q. Jin and Q. Feng, "Frequency and Power Dependence of Passive Intermodulation in Connectors With Contact-Material Nonlinear Modeling," *IEEE Microwave and Wireless Components Letters*, vol. 31, no. 2, pp. 207-210, Feb. 2021, doi: 10.1109/LMWC.2020.3038861.

- [50] V. Golikov, S. Hienonen, and P. Vainikainen, "Passive intermodulation distortion measurements in mobile communication antennas," *IEEE 54th Vehicular Technology Conference. VTC Fall 2001. Proceedings (Cat. No.01CH37211)*, Atlantic City, NJ, USA, 2001, pp. 2623-2625 vol.4, doi: 10.1109/VTC.2001.957226.
- [51] S. Yang, W. Wu, S. Xu, Y. -J. Zhang, D. Stutts, and D. J. Pommerenke, "A Passive Intermodulation Source Identification Measurement System Using a Vibration Modulation Method," *IEEE Transactions on Electromagnetic Compatibility*, vol. 59, no. 6, pp. 1677-1684, Dec. 2017, doi: 10.1109/TEMC.2017.2705114.
- [52] S. Xia et al., "Practical Fixture Design for Passive Intermodulation Tests for Flexible Metallic Contacts," *2022 IEEE International Symposium on Electromagnetic Compatibility & Signal/Power Integrity (EMCSI)*, Spokane, WA, USA, 2022, pp. 17-22, doi: 10.1109/EMCSI39492.2022.9889578.
- [53] S. Xia et al., "Passive Intermodulation Under Different Spring Contact Conditions," *2022 IEEE International Symposium on Electromagnetic Compatibility & Signal/Power Integrity (EMCSI)*, Spokane, WA, USA, 2022, pp. 12-16, doi: 10.1109/EMCSI39492.2022.9889661.
- [54] "TS 136 104 - V8.3.0 - LTE," *IEEE Standard for LTE, 3rd Generation Partnership Project (3GPP)*, 2018.
- [55] N. L. Johnson, S. Kotz, and N. Balakrishnan, *Continuous Univariate Distributions, Volume 2, 2nd Edition*, Wiley, 1995, ISBN 0-471-58494-0 (Section 26.9).
- [56] J. A. Gubner, *Probability and Random Processes for Electrical and Computer Engineers*, Cambridge University Press, 2006, ISBN 978-0-521-86470-1.
- [57] Agilent Technologies, "Agilent Spectrum and Signal Analyzer Measurements and Noise," Retrieved July 25, 2013, from <http://literature.agilent.com/litweb/pdf/5966-4008E.pdf>.
- [58] M. Leone and H. L. Singer, "On the coupling of an external electromagnetic field to a printed circuit board trace," *IEEE Transactions on Electromagnetic Compatibility*, vol. 41, no. 4, pp. 418-424, Nov. 1999, doi: 10.1109/15.809842.
- [59] P. Bernardi and R. Cicchetti, "Response of a planar microstrip line excited by an external electromagnetic field," *IEEE Transactions on Electromagnetic Compatibility*, vol. 32, no. 2, pp. 98-105, May 1990, doi: 10.1109/15.52405.
- [60] M. Leone and V. Navratil, "On the external inductive coupling of differential signalling on printed circuit boards," *IEEE Transactions on Electromagnetic Compatibility*, vol. 46, no. 1, pp. 54-61, Feb. 2004, doi: 10.1109/TEMC.2004.823611.

- [61] S. Park, Y. Kami and Y. Nahm, "Coupling analysis of complex-layout traces using a circuit-concept approach," *IEEE Transactions on Electromagnetic Compatibility*, vol. 56, no. 1, pp. 208-220, Feb. 2014, doi: 10.1109/TEMPC.2013.2273078.
- [62] F. Vanhee, D. Pissoort, J. Catrysse, G. A. E. Vandenbosch and G. G. E. Gielen, "Efficient reciprocity-based algorithm to predict worst case induced disturbances on multiconductor transmission lines due to incoming plane waves," *IEEE Transactions on Electromagnetic Compatibility*, vol. 55, no. 1, pp. 208-216, Feb. 2013, doi: 10.1109/TEMPC.2012.2208754.
- [63] H. Zhao, X. Gao, B. Wang, E. Li and E. K. Chua, "Efficient analysis of radiated immunity of printed circuit boards using SPICE," 2012 IEEE International Symposium on Electromagnetic Compatibility, 2012, pp. 289-293, doi: 10.1109/ISEMC.2012.6351768.
- [64] J. Hunter, S. Xia, A. Harmon, A. Hassan, V. Khilkevich and D. Beetner, "Modeling and statistical characterization of electromagnetic coupling to electronic devices," 2021 United States National Committee of URSI National Radio Science Meeting (USNC-URSI NRSM), 2021, pp. 14-15, doi: 10.23919/USNC-URSINRSM51531.2021.9336496.
- [65] D. Drogoudis, J. Van Hese, B. Boesman and D. Pissoort, "Combined circuit/full-wave simulations for electromagnetic immunity studies based on an extended S-parameter formulation," 2014 IEEE 18th Workshop on Signal and Power Integrity (SPI), 2014, pp. 1-4, doi: 10.1109/SaPIW.2014.6844551.
- [66] F. V. Zonouz, N. Masoumi and M. Mehri, "Effect of IC package on radiated susceptibility of board level interconnection," 2015 International Conference on Synthesis, Modeling, Analysis and Simulation Methods and Applications to Circuit Design (SMACD), 2015, pp. 1-4, doi: 10.1109/SMACD.2015.7301676.
- [67] V. S. Reddy, P. Kralicek and J. Hansen, "A novel segmentation approach for modeling of radiated emission and immunity test setups," *IEEE Transactions on Electromagnetic Compatibility*, vol. 59, no. 6, pp. 1781-1790, Dec. 2017, doi: 10.1109/TEMPC.2017.2699480.
- [68] S. Xia et al., "A fast cascading method for predicting the coupling from external plane waves to PCBs," 2022 IEEE International Symposium on Electromagnetic Compatibility & Signal/Power Integrity (EMCSI), Spokane, WA, USA, 2022, pp. 152-157, doi: 10.1109/EMCSI39492.2022.9889338.
- [69] Stutzman, W. L., & Thiele, G. A. (2013). *Antenna Theory and design*. Wiley.

- [70] S. -J. Guo, L. -S. Wu, M. Tang and J. -F. Mao, "Analysis of illuminated bent microstrip line based on Baum-Liu-Tesche (BLT) equation," 2015 IEEE Electrical Design of Advanced Packaging and Systems Symposium (EDAPS), Seoul, Korea (South), 2015, pp. 159-162, doi: 10.1109/EDAPS.2015.7383691.
- [71] P. Maheshwari, V. Khilkevich, D. Pommerenke, H. Kajbaf and J. Min, "Application of emission source microscopy technique to EMI source localization above 5 GHz," 2014 IEEE International Symposium on Electromagnetic Compatibility (EMC), Raleigh, NC, USA, 2014, pp. 7-11, doi: 10.1109/ISEMC.2014.6898933.
- [72] B. Chen, J. He, Y. Guo, S. Pan, X. Ye and J. Fan, "Multi-ports ( $2n$ )  $2\times$ -thru de-embedding: theory, validation, and mode conversion characterization," IEEE Transactions on Electromagnetic Compatibility, vol. 61, no. 4, pp. 1261-1270, Aug. 2019, doi: 10.1109/TEMC.2019.2908782.
- [73] T. Hubing, "PCB EMC design guidelines: a brief annotated list," 2003 IEEE Symposium on Electromagnetic Compatibility. Symposium Record (Cat. No.03CH37446), Boston, MA, USA, 2003, pp. 34-36 vol.1, doi: 10.1109/ISEMC.2003.1236559.
- [74] C. Su and T. H. Hubing, "Imbalance difference model for common-mode radiation from printed circuit boards," IEEE Transactions on Electromagnetic Compatibility, vol. 53, no. 1, pp. 150-156, Feb. 2011, doi: 10.1109/TEMC.2010.2049853.
- [75] S. Deng, T. Hubing and D. Beetner, "Estimating maximum radiated emissions from printed circuit boards with an attached cable," IEEE Transactions on Electromagnetic Compatibility, vol. 50, no. 1, pp. 215-218, Feb. 2008, doi: 10.1109/TEMC.2007.915288.
- [76] Hwan-Woo Shim and T. H. Hubing, "Model for estimating radiated emissions from a printed circuit board with attached cables due to voltage-driven sources," IEEE Transactions on Electromagnetic Compatibility, vol. 47, no. 4, pp. 899-907, Nov. 2005, doi: 10.1109/TEMC.2005.859060.
- [77] J. Hunter et al., "A segmentation strategy for structures with common mode coupling," 2022 IEEE International Symposium on Electromagnetic Compatibility & Signal/Power Integrity (EMCSI), Spokane, WA, USA, 2022, pp. 415-420, doi: 10.1109/EMCSI39492.2022.9889666.
- [78] M. Tang, J. Lu, J. Mao and L. Jiang, "A systematic electromagnetic-circuit method for EMI analysis of coupled interconnects on dispersive dielectrics," IEEE Transactions on Microwave Theory and Techniques, vol. 61, no. 1, pp. 1-13, Jan. 2013, doi: 10.1109/TMTT.2012.2220562.

- [79] A. B. Kouki, R. Mittra and Chi Hou Chan, "Analysis of a thin slot discontinuity in the reference plane of a microstrip structure," *IEEE Transactions on Microwave Theory and Techniques*, vol. 41, no. 8, pp. 1356-1362, Aug. 1993, doi: 10.1109/22.241675.
- [80] M. Mehri, N. Masoumi and S. Heidari, "Electromagnetic susceptibility analysis of PCBs using predictive method," 2015 International Conference on Synthesis, Modeling, Analysis and Simulation Methods and Applications to Circuit Design (SMACD), Istanbul, Turkey, 2015, pp. 1-4, doi: 10.1109/SMACD.2015.7301686.

## VITA

Shengxuan Xia (Student Member, IEEE) was born in Wuhan, Hubei, China. He received the B.S. degree in electrical and computer engineering from the Huazhong University of Science and Technology, Wuhan, China, in 2018. In May 2024, he received a Doctoral of Philosophy degree in Electrical Engineering with the Electromagnetic Compatibility Laboratory, Electrical and Computer Engineering Department, Missouri University of Science and Technology, Rolla, MO, USA. His research interests included radio-frequency interference, desense, radiated emission susceptibility modeling, and hardware security. Shengxuan Xia was a recipient of the Outstanding graduate Student Member Award in IEEE St. Louis Section 2022, and EMC Society President's Memorial Award 2023.